

ASPECTS OF ELF/VLF CHORUS GENERATION MECHANISM:
SOURCE LOCATION AND MOTION

A DISSERTATION
SUBMITTED TO THE DEPARTMENT OF ELECTRICAL
ENGINEERING
AND THE COMMITTEE ON GRADUATE STUDIES
OF STANFORD UNIVERSITY
IN PARTIAL FULFILLMENT OF THE REQUIREMENTS
FOR THE DEGREE OF
DOCTOR OF PHILOSOPHY

Manuel Platino
October 2006

© Copyright by Manuel Platino 2007
All Rights Reserved

I certify that I have read this dissertation and that, in my opinion, it is fully adequate in scope and quality as a dissertation for the degree of Doctor of Philosophy.

(Umran S. Inan) Principal Co-Advisor

I certify that I have read this dissertation and that, in my opinion, it is fully adequate in scope and quality as a dissertation for the degree of Doctor of Philosophy.

(Timothy F. Bell) Principal Co-Advisor

I certify that I have read this dissertation and that, in my opinion, it is fully adequate in scope and quality as a dissertation for the degree of Doctor of Philosophy.

(Martin Walt)

Approved for the University Committee on Graduate Studies.

Dedication

*Here's one for mother.*¹

¹Frank Vincent Zappa

Abstract

Observations by the Wide Band Data (WBD) plasma wave instrument, on the four Cluster spacecraft, of upper and lower band chorus emissions at geomagnetic latitudes $-10^\circ < \lambda_m < 10^\circ$ and L shells ranging from $L = 4$ to $L = 5$ have been used to estimate the location of the compact sources of chorus emissions. The interpretation of frequency differences exhibited by the same chorus emissions observed on different spacecraft in terms of a differential Doppler shift has led to a simple model involving rapidly moving sources traveling at speeds comparable to the parallel resonant velocity of counter-streaming gyroresonant electrons. Even though this property of the sources of chorus waves was discussed as a possibility in early models of chorus generation, such source motion was not observed previously and a physical interpretation of the source motion was not previously presented. In this thesis a physical interpretation of the rapid motion of sources of chorus waves is given, building upon previous models of chorus emissions and energetic electron phase bunching and delineating the relationship between rapid temporal growth and saturation of chorus and the rapid movement of the source of these waves. For selected cases in 2003, the source characteristics (location, velocity, and frequency dependence of these parameters) and the linear wave growth rate are estimated using broadband measurements of the plasma wave electric field observed by the WBD instrument and energetic electron fluxes observed by the Plasma Electron And Current Experiment (PEACE) instrument onboard Cluster. For these cases, the particle distribution functions estimated from data are used to calculate the linear amplitude growth due to cyclotron resonance. Results indicate that chorus sources move for ~ 6000 km along the Earth's magnetic field lines at a velocity of $\sim 0.05 c$. The emitted chorus waves at the source

are assumed to have a wide range of wave normal angles, but the rays reaching the spacecraft are generally only those with small wave normal angles. In general, the direction of motion of the source, either away or toward the Cluster spacecraft, appears to be determined by the wave amplitude growth rate.

Acknowledgments

With absolute certainty I knew this section was going to be the most difficult to write, knowing that it is so difficult to transmit the immense proportions of my gratitude toward the people who have contributed to my formation as a scientist and as a person. To assume that all the work and effort put into becoming a Ph.D. was done only by me would be absurd. Of course none of this would have been possible without the guidance of my mentors, Umran Inan and Timothy Bell. During all these years I have done my best to absorb not only the knowledge, but also the wisdom of these two excellent professionals and persons, learning not only about electromagnetism and plasma physics, but also many other aspects that have contributed to my formation as a professional and as a person.

Most of my work as a member of the Cluster team was possible thanks to the support of doctors Donald Gurnett, Jolene Pickett, Patrick Canu and Pierrette Décréau whose valuable help has been crucial to the work in this dissertation.

Being part of the VLF group was also a huge motivation, and it provided me the possibility to learn from brilliant scientists, such as Martin Walt, who has taken the time to read this dissertation, and also both Donald Carpenter and Robert Helliwell, whose advice, support and comments have helped me most. I would also like to thank professors Howard Zebker and Vahe Petrosian for agreeing to be part of my defense committee. But not only from renowned faculty comes wisdom: I must also mention the invaluable help I got from my fellow students and members of the group, most of all Troy Wood, Jacob Bortnik, Maria Spasojević and Timothy Chevalier, all of whom contributed enormously to my formation. I would also like to thank Shaolan Min and Helen Niu as well, for being the heart and soul of the VLF group.

Not a single word of this dissertation would have been written in the first place if not for the role played by my grandfathers Antonio Platino and Ricardo Cabrera, who introduced me to science and encouraged me to study the field from a very young age. Of course I must mention my parents, Carlos Platino and Ana Lía Cabrera, who were the main influence in my formation as a person, and I could never find words to properly represent my gratitude toward them; and my brothers Mariano Platino and Mauricio Platino whose support was invaluable. My friends and colleagues, Ignacio Zuleta, Karl Stahl, Ernesto Staroswiecki, Pablo Vázquez, Catherine Sullivan, David Gutiérrez, Gabriel Velarde, Ramón Prieto, Jeffrey Sadowsky, Víctor Calo, Natacha Poggio and my lifetime buddy Ovidio Antón are people who gave huge support to me during the whole stimulating and sometimes difficult experience of studying and living in a foreign country. Cristina Bordon and Ricardo Díaz deserve a special mention, for being like stepparents to me in the United States.

Finally and most of all, I would like to thank María Disalvo, the person who has the patience and caring of going with me through the most important and difficult stages of becoming a Ph.D. with such love and support that I find it hard to imagine how I could have managed without her.

...y gracias a los que me acompañaron desde la distancia en este viaje.

Manuel Platino

Stanford, CA

October 5, 2006

This research was supported by the National Aeronautics and Space Administration, under parent grant NAG5-9974 at the University of Iowa and with Subcontract No.4000061641 to Stanford University. We greatly appreciate the help of D.L. Gurnett, J.S. Pickett, C. Abramo of DSN and M. Hapgood of RAL in scheduling the real-time wideband data acquisition from the WBD receiver, and also the help of J. H. Dowell, I. W. Christopher, J. M. Seeberger and R. L. Brechwald of the University of Iowa in reducing the data to usable form. We thank Drs. P.M.E. Décréau and P. Canu who have provided the WHISPER data; and Dr. A.N. Fazakerley who provided the PEACE data.

Contents

Dedication	v
Abstract	vi
Acknowledgments	viii
1 Introduction	1
1.1 Electromagnetic Chorus Waves	3
1.1.1 Chorus Observations in Space	5
1.1.2 Proposed Mechanisms of Generation of Chorus	18
1.2 The Cluster Mission	19
1.3 A Review of Whistler Mode Propagation	22
1.4 An Overview of Cyclotron Resonance	27
1.5 Overview and Contributions	29
2 Estimation of Chorus Source Location	31
2.1 Doppler Shift due to Source Motion	31
2.2 Previous Work on Moving Sources of Chorus	37
2.3 Source Location and Velocity Determination	44
3 Observations and Results for July 24, 2003	53
3.1 Observations on July 24, 2003	53
3.1.1 Geomagnetic Conditions	54
3.1.2 WBD Observations	56

3.2	Source Location and Velocity for July 24, 2003	63
3.2.1	Source Location Results for Case 1	67
3.2.2	Source Location Results for Case 2	71
3.2.3	Raytracing Results	71
3.2.4	Source Velocity Results	75
4	Physical Interpretation of Moving Sources	77
4.1	Interpretation of Chorus Source Motion	78
4.2	Phase Bunching	81
4.3	Wave amplification by Cyclotron Resonance	84
4.4	The Process of Source Motion	90
4.5	Summary of the Model	93
5	Observations on August 23, 2003. Comparison	95
5.1	Observations on August 23, 2003	95
5.1.1	Geomagnetic Conditions	96
5.1.2	WBD Observations	96
5.2	Source Location Derived from PEACE Data	101
6	Summary	110
6.1	Summary	110
6.2	Discussion	113
6.3	Suggestions for Future Work	117
6.3.1	Improvements on the Source Location Method	117
6.3.2	Improvements in the measurement of the frequency-time differ- ences between spacecraft	117
6.3.3	Improvements in the Physical Interpretation Model	118
	Bibliography	119

List of Tables

3.1	Values \mathbf{x}_g used to solve the system of equations described by (2.8), (2.9), (2.12), (2.17) and (2.18), for Case 1	65
3.2	Values \mathbf{x}_g used to solve the system of equations described by (2.8), (2.9), (2.12), (2.17) and (2.18), for Case 2	66
6.1	Estimated values of average growth rate γ and bunching time τ_B for each estimated frequency ω_ξ , obtained for the calculations performed in Case 1.	115
6.2	Estimated values of average growth rate γ and bunching time τ_B for each estimated frequency ω_ξ , obtained for the calculations performed in Case 2.	116
6.3	Estimated values of average growth rate γ and bunching time τ_B for each estimated frequency ω_ξ , obtained for the calculations performed in Case 3.	116
6.4	Estimated values of average growth rate γ and bunching time τ_B for each estimated frequency ω_ξ , obtained for the calculations performed in Case 4.	116

List of Figures

1.1	The Magnetosphere, adapted from <i>Hill and Dessler</i> (1991)	4
1.2	Polar PWI observations of plasma waves	7
1.3	Cluster WBD observations of chorus on 11/27/2000	9
1.4	Cluster WBD observations of chorus on 07/25/2001	10
1.5	Cluster WBD observations of chorus on 04/18/2002	11
1.6	Cluster WBD observations of chorus on 01/26/2003	12
1.7	Cluster WBD observations of chorus on 09/06/2004	14
1.8	Cluster WBD observations of chorus on 03/23/2005	15
1.9	Cluster spacecraft orbit configuration	21
1.10	Whistler-mode wave packet and refractive index surfaces	23
1.11	The cyclotron resonance	28
2.1	Doppler frequency shift in two different mediums	33
2.2	Doppler frequency shift due to source motion, at $f = 6\text{kHz}$, $f_{ce} = 12\text{kHz}$ and $f_{pe} = 40\text{kHz}$	36
2.3	Chorus source location in 2D, adapted from <i>Inan et al.</i> (2004)	39
2.4	Estimation of chorus source location, adapted from <i>Inan et al.</i> (2004)	41
2.5	Proposed model of different localized sources of ELF/VLF chorus . .	43
2.6	Schematic of the chorus emission model of a source moving along \mathbf{B}_0	49
3.1	Geomagnetic conditions and Whisper observations on July 24, 2003 .	55
3.2	WBD overview spectrogram of observations on July 24, 2003	57
3.3	Observations on July 24, 2003, 01:14:38 UT: Case 1	59
3.4	Observations on July 24, 2003, 01:35:25 UT: Case 2	61

3.5	Source location results for Case 1	68
3.6	Results verification on Case 1	70
3.7	Source location results for Case 2	72
3.8	Raytracing results for July 24, 2003	75
3.9	Results of the calculations of source velocity	76
4.1	General picture of the physical interpretation of chorus	80
4.2	Phase bunching process	83
4.3	Radiating current distribution in space and time	85
4.4	PEACE observations of energetic particle flux	88
4.5	Wave amplification by cyclotron resonance	89
4.6	General description of the model	92
5.1	Geomagnetic conditions and Whisper observations on August 23, 2003	97
5.2	WBD overview spectrogram of observations on August 23, 2003	98
5.3	Observations on August 24, 2003, 23:00:25 UT: Case 3	100
5.4	Observations on August 24, 2003, 23:02:30 UT: Case 4	102
5.5	Comparison of source location results for Case 1	105
5.6	Comparison of source location results for Case 2	106
5.7	Comparison of source location results for Case 3	108
5.8	Comparison of source location results for Case 4	109

Chapter 1

Introduction

‘Pigmaei gigantum humeris impositi plusquam ipsi gigantes vident.’¹

‘Bernard of Chartres used to say that we are like dwarfs on the shoulders of giants, so that we can see more than they, and things at a greater distance, not by virtue of any sharpness of sight on our part, or any physical distinction, but because we are carried high and raised up by their giant size.’²

This dissertation concerns observations, from multiple spacecraft, of an intense and discrete type of electromagnetic emission known as Extremely Low Frequency and Very Low Frequency (ELF/VLF) ‘chorus’, and the identification of the properties and rapid motion of the compact sources from which these chorus waves emanate. An interpretation is also provided in terms of other known properties of chorus.

One of the first references to chorus mentioned in the published literature is in the Appendix of [Storey, 1953] where an unidentified electromagnetic noise was noticed and mentioned as ‘dawn chorus’. Chorus waves are usually observed in the ELF/VLF band, which overlaps with the audible frequency range. Before the use of spectrograms it was common practice to ‘listen’ to plasma waves observed in the ELF/VLF range by connecting the time series recordings of the electromagnetic signal (usually recorded

¹‘Dwarves, placed upon the shoulder of giants, see further than the giants themselves’.- Bernardus Carnotensis (*Bernard of Chartres*)

²John of Salisbury, *Metalogicon*, believed to be written around 1159

on a magnetic tape) to a speaker and using the human brain's natural ability to perform Fourier transforms as a means to identify the different types of plasma waves. *Storey* [1953] used the name 'dawn chorus' to denote the fact that 'the sound of the dawn chorus may be likened to that of a rookery heard from a distance'. These first observations were obtained from ground-based measurements in Cambridge, United Kingdom.

Extensive studies were performed during the 1960s to understand the nature of chorus waves and the physical mechanisms of their generation. As mentioned later in this Chapter, the importance of chorus waves in the overall context of space physics increased following the dawn of the space age, especially with the discovery of the Earth's radiation belts [*Van Allen*, 1959], after which the study of near-Earth space and the role of plasma waves therein came to the fore as a subject of great interest.

This dissertation is divided into three parts. In Chapter 1, chorus emissions are introduced, and an overview is given of previous work to understand the properties of chorus, their propagation and mechanisms of its generation. The Cluster mission and data are then described, along with a review of whistler mode propagation. The contributions of the present work are also itemized at the end of this Chapter. In Chapters 2 to 5 the estimation of the chorus source location and motion from multi-spacecraft data is described. In those Chapters a quantitative interpretation of source motion as a necessary consequence of observed properties of chorus, such as rapid temporal growth, saturation, and frequency-time shapes is presented. The observations performed by the Cluster spacecraft that are used to test the proposed interpretation of moving sources of chorus are also described in these Chapters. Finally, in Chapter 6, we summarize the results and succinctly state the conclusions.

The relation between chorus waves and trapped particles in the inner magnetosphere has become increasingly important over the years. Nowadays it is evident that one of the most important types of waves that can energize trapped particles in the outer radiation belts is whistler mode chorus interacting with electrons via Doppler shifted cyclotron resonance [*Meredith et al.*, 2003]. These chorus waves are believed to play a key role in the acceleration of trapped energetic electrons in the radiation belts [*Isenberg et al.*, 1982; *Horne et al.*, 2005; *Spasojević and Inan*, 2005] to MeV

energies at which they can cause serious problems for electronics onboard spacecraft moving through the belts [Baker, 2000]. Horne *et al.* [2005] concluded that wave acceleration by whistler mode chorus is a viable mechanism for electron flux increases during magnetically disturbed times in the heart of the outer radiation belt near $L=4.5$. During the same cyclotron resonant interactions, which lead to acceleration, other trapped particles whose pitch angles are near the loss cone are removed by pitch angle scattering, which redirects their momentum, resulting in their precipitation into the atmosphere [Holzer *et al.*, 1974; Horne and Thorne, 2003].

1.1 Electromagnetic Chorus Waves

Chorus waves are electromagnetic emissions observed in the inner magnetosphere, a region in space where the plasma dynamics is dominated by the Earth's magnetic field, denoted herein as \mathbf{B}_0 . Chorus is observed more specifically in the inner part of this region, at distances of 15000 – 30000 km from the Earth's surface. Figure 1.1 shows a schematic diagram of the magnetosphere, a cold, magnetized, inhomogeneous collisionless plasma, exhibiting a wide range of plasma densities that can vary depending on the region of the magnetosphere studied. Cold plasma densities found throughout the magnetosphere are of the order of $1 - 200 \text{ cm}^{-3}$, and they can vary significantly over distances of $\sim 1000 \text{ km}$.

The plasmasphere is a doughnut-shaped region inside the Earth's magnetosphere. It is basically an extension of the ionosphere, or the topmost part of the Earth's atmosphere, and is shown in Figure 1.1 as a shaded area around the Earth. This region of space is characterized by having much higher densities of cold ($\sim 1 \text{ eV}$) electrons than the rest of the magnetosphere. The outer limit of the plasmasphere is called the plasmapause, a region in space where the gradient of the electron density is much larger than that found in the rest of the plasmasphere.

Chorus waves are usually observed in the region outside the plasmapause in the ELF/VLF band, herein defined as the frequency range between 300 Hz and 30 kHz. They are distinguished as discrete elements, each of which lasts for a time on the order of a tenth of a second up to several seconds. For each of these elements, the frequency

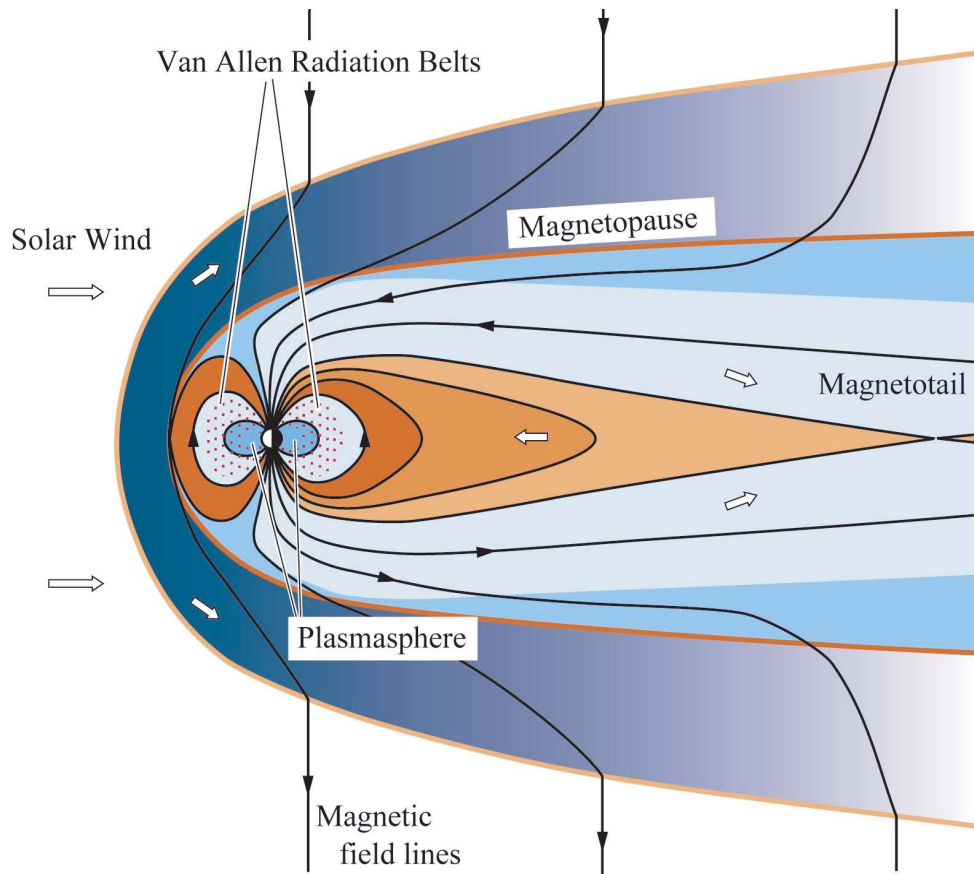


Figure 1.1: Schematic diagram of the magnetosphere and its most important regions [Hill and Dessler, 1991]. The solid black lines indicate the magnetic field lines of the Earth and the Solar Wind. The white arrows indicate the direction of motion of the particles that constitute the Solar Wind, arriving from the Sun, located leftward of the image.

usually changes with an approximately linear rate of several kHz/sec to hundreds of Hz/sec. Chorus usually consists of elements of increasing frequency, but elements of decreasing frequency and with more complicated structure are also often observed. Chorus waves are generally observed in two frequency bands, separated by a narrow band of decreased intensity near one half of the local electron cyclotron frequency [Burtis and Helliwell, 1976]. Chorus waves studied in the present work were observed at frequencies both above and below this gap of decreased intensity, and are typically referred to as ‘upper band chorus’ and ‘lower band chorus’ respectively. For a good summary of previous work on chorus see *Sazhin and Hayakawa* [1992], *Lauben et al.* [2002] and references therein.

There have been extensive observations of chorus waves, both in space and on the ground since the first report by *Storey* [1953]. One of the earliest reports on chorus emissions observed in-situ [Gurnett and O’Brien, 1964] concerned observations at frequencies from a few hundred Hz to several kHz. Since then, discrete ELF/VLF chorus emissions have been found to constitute one of the most intense forms of electromagnetic plasma waves observed in the vicinity of the Earth [e.g., *Smith et al.*, 1996; *Gurnett and Inan*, 1988; *Lauben et al.*, 1998], and other magnetized planets [e.g., *Scarfi et al.*, 1979; *Warwick et al.*, 1979; *Gurnett et al.*, 1979b], in the ELF/VLF range of frequencies. In the following, we provide a review only of chorus observations in space, as is relevant to the topic of this dissertation, involving observations on the Cluster spacecraft.

1.1.1 Chorus Observations in Space

Satellite observations at high latitudes and altitudes not exceeding 3000 km [Dunckel and Helliwell, 1969; Holzer et al., 1974; Ondoh et al., 1982] reported chorus waves to be propagating poleward with their group velocity vectors parallel to the Earth’s magnetic field, with the upper and lower frequency limits decreasing with increasing L -value. These observations implied that chorus observed at high latitudes propagate away from the equator. This idea was also extensively reported based on measurements on the OGO spacecraft [Burtis and Helliwell, 1969 and 1976; Burtis, 1974;

Russell et al., 1969]. These studies based on observations onboard OGO, showed chorus to be generated close to the geomagnetic equator, at Magnetic Local Times (MLT) on the dawn and noon side, at distances of $1-2$ Earth radii from the plasmapause, with the most common emissions being rising tones. In the studies mentioned above, it was concluded that the generation region of chorus lies within 25° in latitude of the geomagnetic equator. An average predominantly poleward direction of propagation has also been observed at high altitudes [*LeDocq et al.*, 1998; *Parrot et al.*, 2003]. Recent studies of the spatial extent of chorus sources using observations onboard the Cluster spacecraft, yielded values of $\sim 7-100$ km across \mathbf{B}_0 and $\sim 60-260$ km along \mathbf{B}_0 [*Santolík and Gurnett*, 2003; *Santolík et al.*, 2003]. These results indicate the presence of a compact source, i.e., a region in space that has dimensions comparable to the wavelength $\sim \lambda$ of the emitted waves.

As used in the previous paragraph, the Magnetic Local Time (MLT) refers to the position of the observation point relative to the Sun. The MLT at each location depends on the difference between the geomagnetic longitude at that point and the geomagnetic longitude at the point of midnight (i.e., directly opposite to the direction of the Sun along the Sun-Earth line). In other words, MLT is 12:00 (noon) if the location faces the Sun, while MLT is 24:00 (midnight) if it faces directly away from the Sun, and other values of MLT follow for other relative positions with respect to the Sun-Earth line. Magnetic longitude and latitude are defined in the same way as geographic latitude and longitude, but converging to and emerging from the magnetic poles instead of the geographic poles [*Helliwell*, 1965, Appendix].

The frequency-time spectrogram in Figure 1.2 shows plasma wave observations on the Polar spacecraft as it moved around the Earth in a highly elliptical orbit, the meridional projection of which is sketched in the upper left panel. The spectrogram shows the power spectral density of the wave electric field as a function of time and frequency. The auxiliary scales below the time axis show the location of the spacecraft in geomagnetic coordinates (Radial distance Re , geomagnetic latitude λ_m , L -value, and MLT). The coordinate Re is a radial distance unit measured from the center of the Earth. In other words $1 Re = 6371$ km and is equal to the radius of a sphere of the same volume as the Earth's. The white line represents the local electron gyration

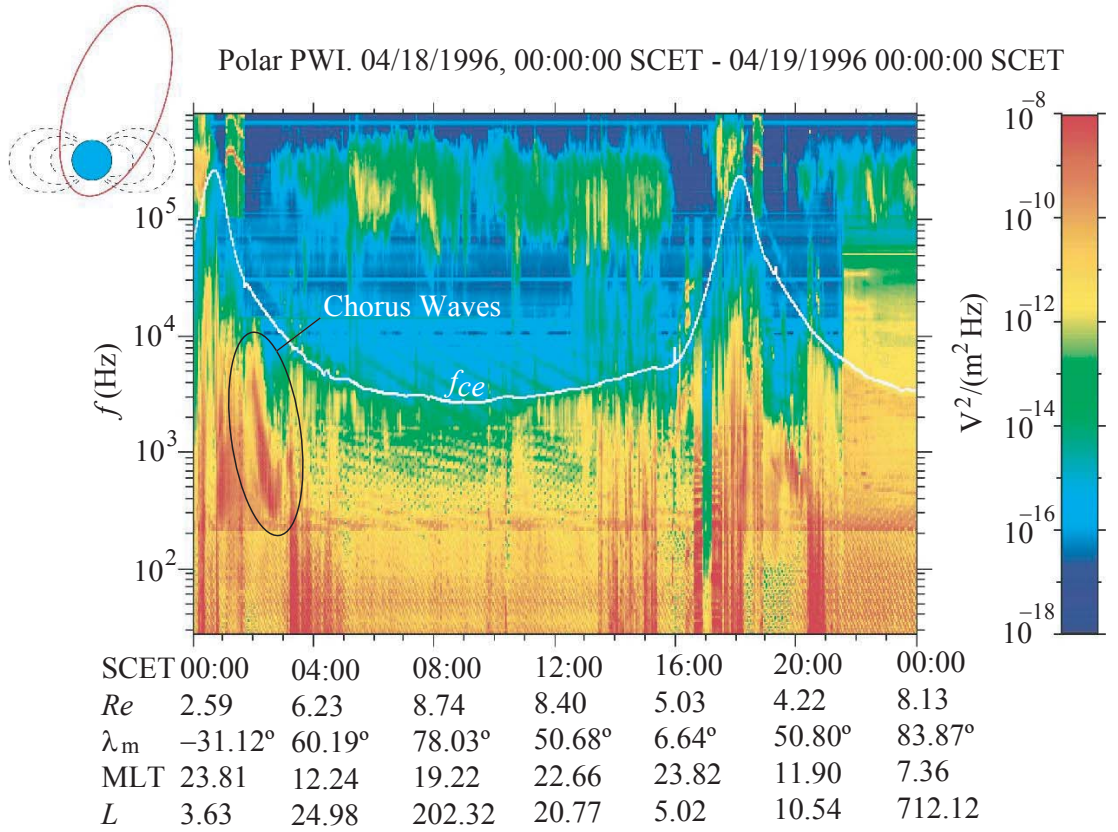


Figure 1.2: Power spectral density of the wave electric field, as observed by the Polar PWI instrument during 04/18/1996. The vertical axis represents the frequency in Hz, while the horizontal axis represents time in the SCET (Spacecraft Event Time) scale. The auxiliary horizontal axes show the geomagnetic coordinates of the spacecraft along its orbit. The color scale represents the power spectral density of the electric field ($V^2/(\text{m}^2\text{Hz})$). The white line represents the value of the local electron cyclotron frequency f_{ce} . Circled in the spectrogram are the observations of chorus waves between 01:30 and 03:00 SCET.

frequency or gyrofrequency ($f_{ce} = \omega_{ce}/2\pi$). Chorus waves are observed in the circled region in the Figure and also later near 20:00 UT with a relatively weaker intensity when the satellite passes through the same MLT region.

More detailed (high time resolution) examples of chorus observed by the Wide Band Data (WBD) plasma wave instrument [Gurnett *et al.*, 1997] on the Cluster spacecraft are shown in Figures 1.3 to 1.8. These observations exemplify the variety of frequency, bandwidth, and spectral shapes of magnetospheric chorus emissions, as well as their varying intensities observed by the Cluster spacecraft. Figures 1.3 to 1.8 illustrate six different Cluster passes on 11/27/2000 (Figure 1.3), 07/25/2001 (Figure 1.4), 04/18/2002 (Figure 1.5), 01/26/2003 (Figure 1.6), 09/06/2004 (Figure 1.7) and 03/23/2005 (Figure 1.8), each day exhibiting different degrees of chorus activity.

All of the spectrograms show wideband observations of the electric field on two to four spacecraft during a pass of about 2 hours. The top labels on each spectrogram show the geomagnetic coordinates of the spacecraft at the observation time. The sudden changes in the amplitude of the background noise observed in Figures 1.7 and 1.8 are due to pre-programmed switching between antennas (from the electric to the magnetic search coil antennas) that connect to the wideband receiver (see below) on-board the Cluster spacecraft. Single chorus elements can be easily distinguished and exhibit approximately linear frequency-time shapes in some cases, as well as other kinds of shapes. The wide range of intensities observed in the six cases shown in Figures 1.3 to 1.8 exemplifies the high variability of chorus activity. Intensities of chorus waves shown in Figures 1.3 to 1.8 range from relatively low (i.e., ~ 0.056 mV/m in Figure 1.3) to very high (~ 10 mV/m in Figure 1.5). Other different types of plasma waves are also observed in Figures 1.3 and 1.4, in addition to the so-called upper and lower band chorus, as well as Extremely Low Frequency (ELF) hiss, as indicated, which is commonly seen at lower frequencies inside the plasmapause [Gurnett and O'Brien, 1964; Burtis, 1974]. Plasmaspheric ELF hiss is usually not accompanied by discrete chorus activity, since chorus is typically only observed outside the plasmapause. In Figure 1.5, the sometimes quasi-periodic nature of chorus emissions [Burtis and Helliwell, 1976] is also evident. Figure 1.6 shows how the frequency shapes can vary from the typically observed ‘risers’ (a narrowband signal whose center frequency

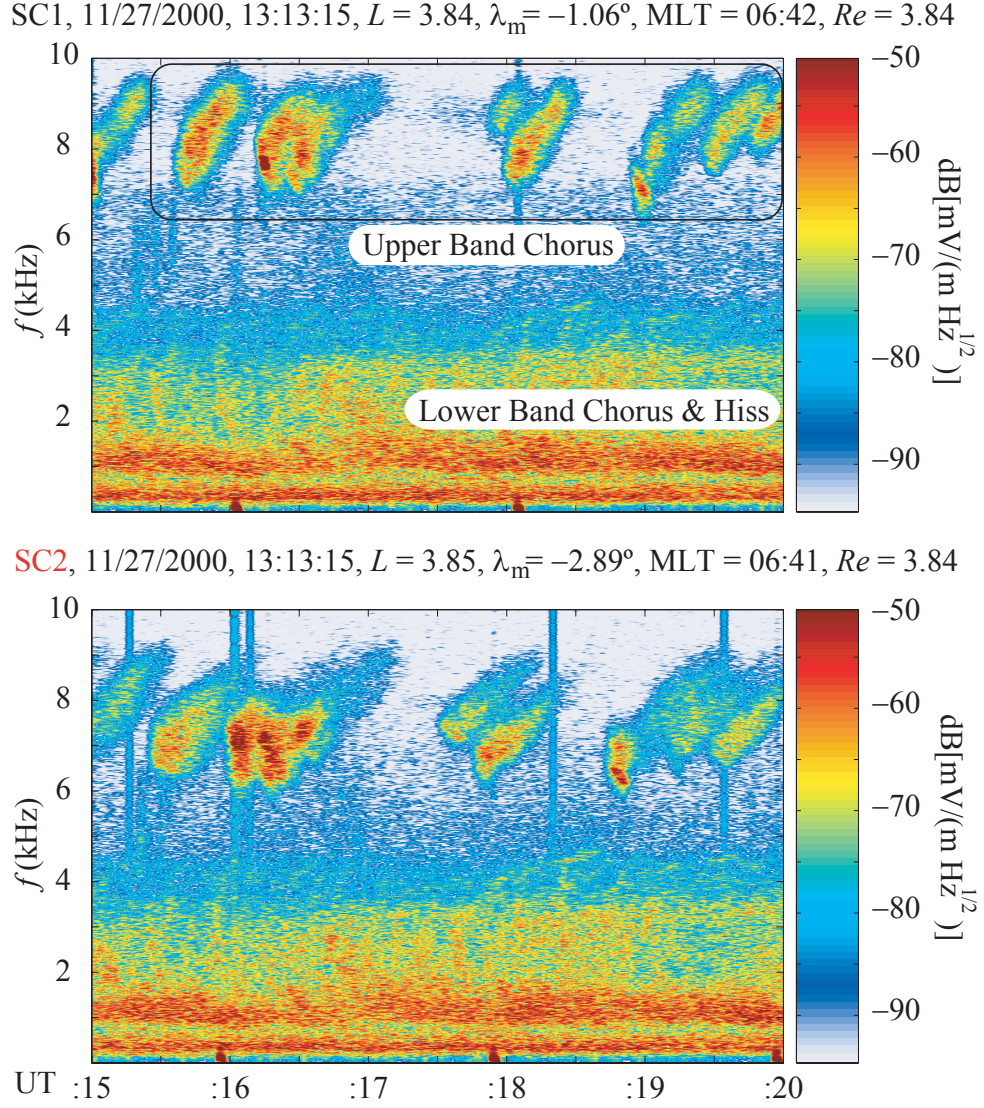


Figure 1.3: WBD spectrograms of plasma waves observed by the Cluster spacecraft during passes on 11/27/2000. The vertical axis represents frequency (kHz) and the horizontal axis represents Universal Time UT. Also indicated are the geomagnetic coordinates of the spacecraft for each case. The color scale represents the amplitude of the electric field with respect to $1 \text{ mV}/(\text{m}\sqrt{\text{Hz}})$.

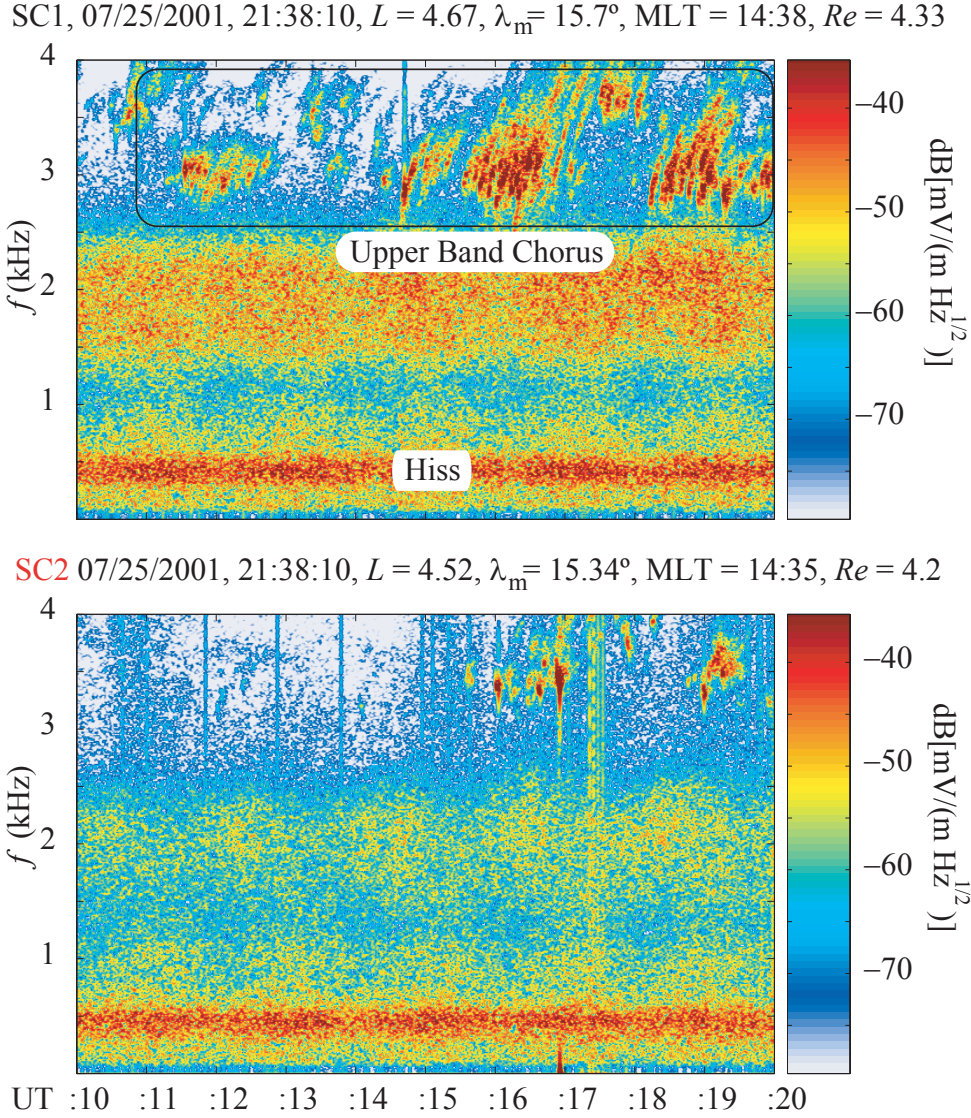


Figure 1.4: WBD spectrograms of plasma waves observed by the Cluster spacecraft during passes on 07/25/2001. The vertical axis represents frequency (kHz) and the horizontal axis represents Universal Time UT. Also indicated are the geomagnetic coordinates of the spacecraft for each case. The color scale represents the amplitude of the electric field with respect to $1 \text{ mV}/(\text{m}\sqrt{\text{Hz}})$.

SC3 04/18/2002, 08:52:02, $L = 4.36$, $\lambda_m = 0.776^\circ$, MLT = 21:00, $Re = 4.36$

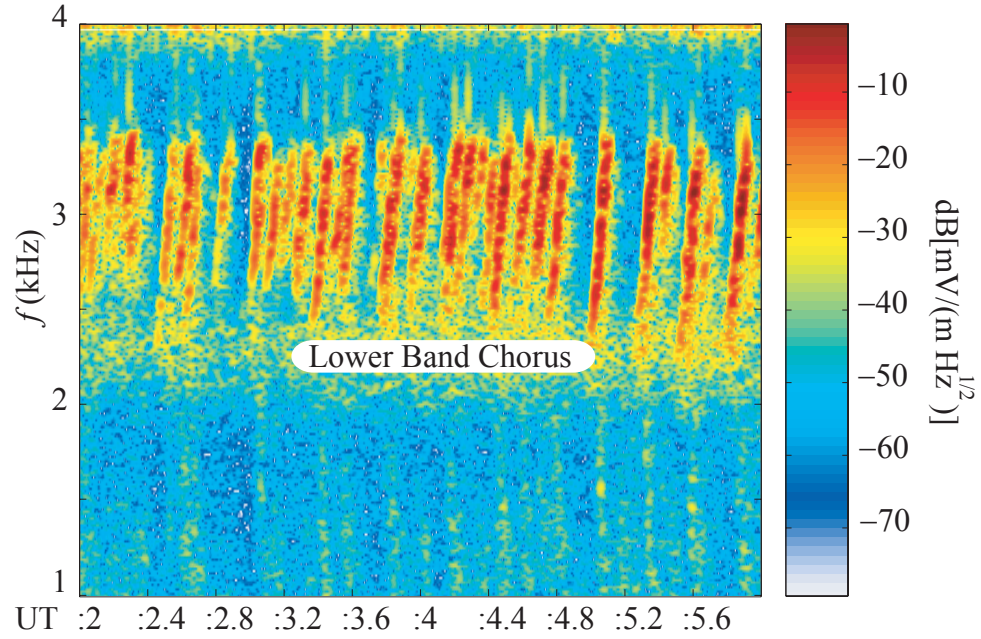


Figure 1.5: WBD spectrograms of plasma waves observed by the Cluster spacecraft during passes on 04/18/2002. The vertical axis represents frequency (kHz) and the horizontal axis represents Universal Time UT. Also indicated are the geomagnetic coordinates of the spacecraft for each case. The color scale represents the amplitude of the electric field with respect to $1 \text{ mV}/(\text{m}\sqrt{\text{Hz}})$.

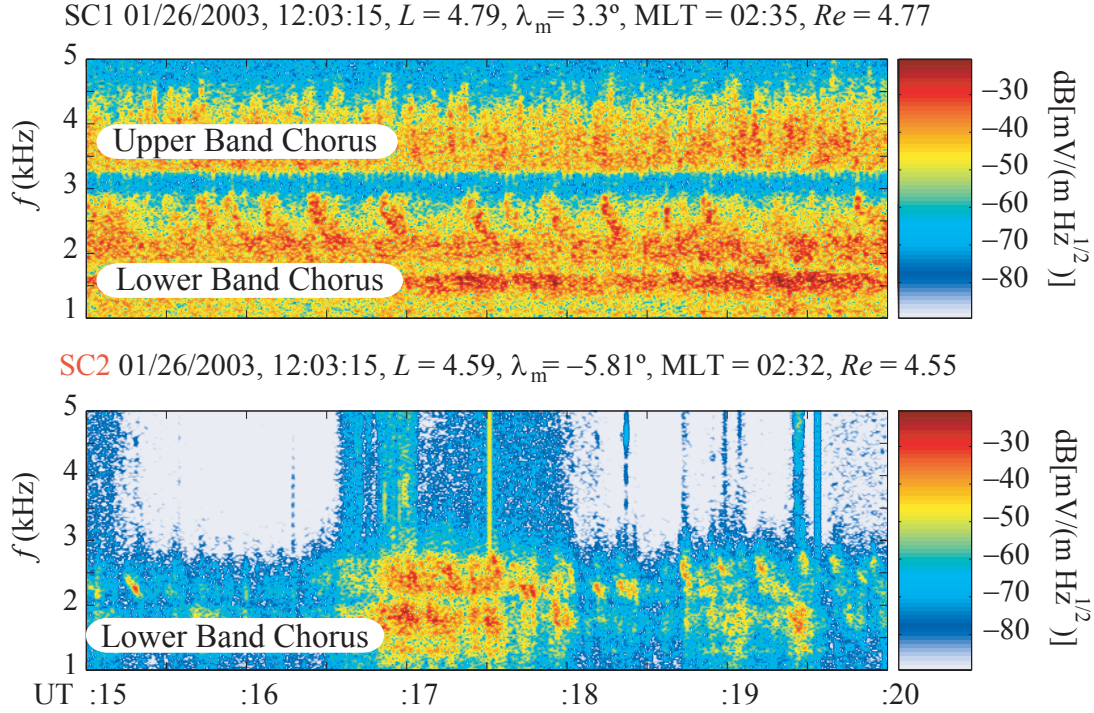


Figure 1.6: WBD spectrograms of plasma waves observed by the Cluster spacecraft during passes on 01/26/2003. The vertical axis represents frequency (kHz) and the horizontal axis represents Universal Time UT. Also indicated are the geomagnetic coordinates of the spacecraft for each case. The color scale represents the amplitude of the electric field with respect to $1 \text{ mV}/(\text{m}\sqrt{\text{Hz}})$.

increases over time) to ‘fallers’ (a narrow band signal whose center frequency decreases with time) and other more complicated frequency-time characteristics. As mentioned before, the upper and lower frequency limits of observed chorus activity typically increase with decreasing value L , and a frequency gap near half the electron gyrofrequency is often observed within which waves are absent [Burtis and Helliwell, 1976].

In all, the detailed spectrograms of Figures 1.3 to 1.8 exemplify the facts that chorus waves consist of discrete bursts of highly coherent electromagnetic emissions, whose wideband intensity can be as high as $\sim 30 \text{ mV}/\text{m}$ (for the cases shown in Figures 1.3 to 1.8), and which are usually observed between 200 Hz and 10 kHz. Exhaustive studies of chorus wave intensities, such as those presented in Meredith *et al.* [2001],

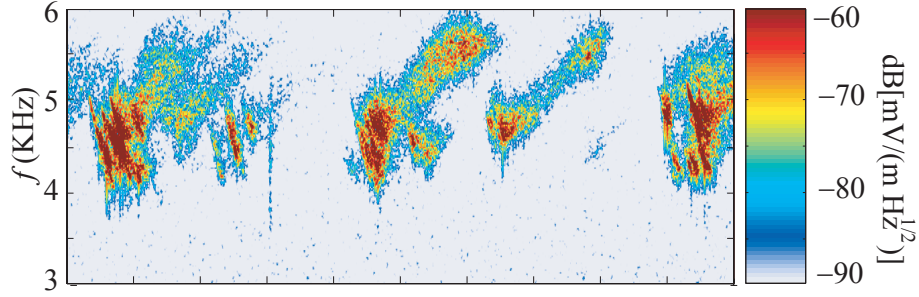
show that chorus emissions observed near the geomagnetic equator are strongest in the lower band during geomagnetically active periods with average amplitudes typically >0.5 mV/m in the dawn side region of the magnetosphere, $3 < L < 7$.

These intense natural emissions known as chorus are believed to be produced by energetic electrons that populate the radiation belts of the Earth. As mentioned before, the name ‘chorus’ originates from the fact that when wideband chorus time series data is connected to an audio amplifier, the audio signal sounds like a chorus of birds. In recognition of their spectral-time shapes and short durations, chorus emissions are usually also referred to as ‘discrete electromagnetic emissions’. The mechanism of generation of chorus waves is generally believed to be cyclotron resonance interactions with energetic electrons [Helliwell, 1967; Sazhin and Hayakawa, 1992]. Observationally, the region in which chorus is usually generated was found to be near the geomagnetic equator, in the region just outside the plasmasphere [Burtis and Helliwell, 1976], although details of the generation mechanism, especially the physical processes that lead to the rapid growth rates, high coherence, saturation, and frequency-time shapes (i.e., risers, fallers and the occasional hook type shapes) are not yet known.

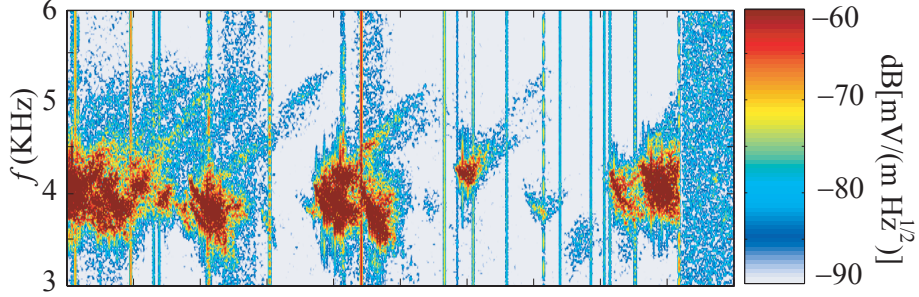
All of the chorus data used for this dissertation were acquired with the Wide Band Data plasma wave instrument (WBD) onboard the Cluster spacecraft [Gurnett *et al.*, 1997], which provides continuous broadband high time resolution measurements of the electric field in the VLF band. An important advantage of continuous broadband data over more compressed or reduced data formats is the fact that it provides the ability to distinguish discrete emissions, such as chorus, from other plasma waves.

In the present work, our attention is focused on discrete structured activity. However, it should be borne in mind that chorus is often accompanied by background unstructured hiss, which is at times quite strong and occasionally appears without any accompanying chorus. In previous studies [e.g., Burtis, 1974], this unstructured noise was called ‘banded hiss’ because of its tendency to accompany band-limited chorus. Its region of maximum occurrence was found to be generally similar to that of banded chorus (and in the region of occurrence of chorus described earlier). Banded hiss was observed somewhat less frequently than chorus in the dawn and noon sectors,

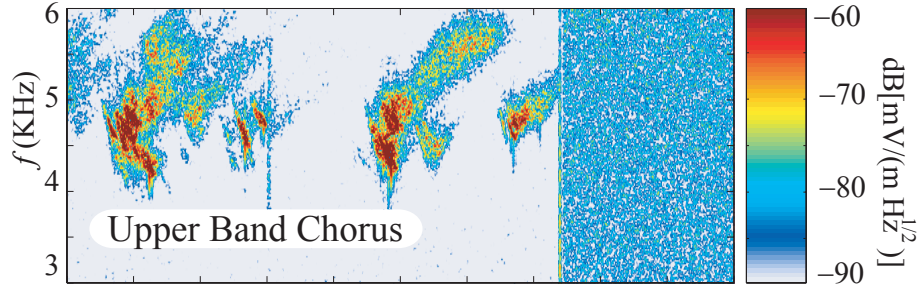
SC1, 09/06/2004, 21:50:30, $L = 4.68$, $\lambda_m = -3.42^\circ$, MLT = 12:12, $Re = 4.66$



SC2, 09/06/2004, 21:50:30, $L = 4.75$, $\lambda_m = -8.81^\circ$, MLT = 12:14, $Re = 4.63$



SC4, 09/06/2004, 21:50:30, $L = 4.58$, $\lambda_m = -3.98^\circ$, MLT = 12:13, $Re = 4.55$



UT :30 :31 :32 :33 :34 :35 :36 :37 :38 :39 :40

Figure 1.7: WBD spectrograms of plasma waves observed by the Cluster spacecraft during passes on 09/06/2004. The vertical axis represents frequency (kHz) and the horizontal axis represents Universal Time UT. Also indicated are the geomagnetic coordinates of the spacecraft for each case. The color scale represents the amplitude of the electric field with respect to $1 \text{ mV}/(\text{m}\sqrt{\text{Hz}})$.

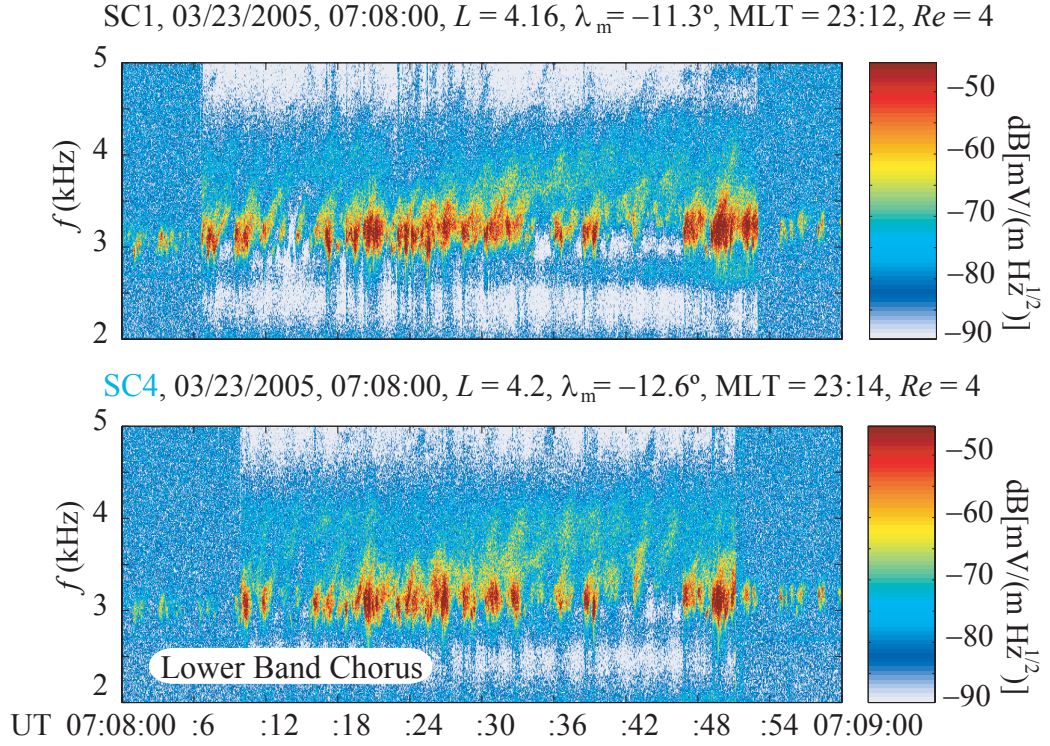


Figure 1.8: WBD spectrograms of plasma waves observed by the Cluster spacecraft during passes on 03/23/2005. The vertical axis represents frequency (kHz) and the horizontal axis represents Universal Time UT. Also indicated are the geomagnetic coordinates of the spacecraft for each case. The color scale represents the amplitude of the electric field with respect to $1 \text{ mV}/(\text{m}\sqrt{\text{Hz}})$.

but during the rest of the day the occurrence of two types of waves was roughly equal.

The first simultaneous observations of chorus emissions on multiple Cluster satellites revealed the surprising result that some individual chorus elements were observed at different frequencies on different spacecraft [Gurnett *et al.*, 2001]. Based on these results, Inan *et al.* [2004] provided the first calculations of chorus source velocity, interpreting the frequency differences observed on different spacecraft in terms of the rapid motion of the compact source(s) of chorus, leading to the observed frequency differences via a differential Doppler shift. This differential Doppler shift differs markedly from that which can be observed from moving sources in free space, due to the unique dependence of the whistler-mode refractive index on the wave normal angle ψ , the angle between the wave vector \mathbf{k} and the Earth's ambient magnetic field \mathbf{B}_0 . The results of Inan *et al.* [2004] supported the idea of compact sources rapidly moving in a field-aligned fashion.

It is important to note that rapid motion of chorus sources is not inconsistent with any aspect of our basic theoretical understanding of chorus being produced as a result of gyroresonant interactions with counterstreaming energetic electrons. In fact, the drift motion of the chorus interaction region was discussed explicitly by Helliwell [1967], based on heuristic arguments, noting that such drifts could occur either in the direction of chorus propagation or opposite to it, and at speeds ranging from zero to the wave group velocity or parallel velocity of the resonant electrons. In Chapters 4 and 5, we show indeed that rapid motion of chorus sources is a necessary consequence of other measured and known properties of chorus emissions, namely the rapid temporal growth, saturation of growth, and the frequency-time shapes.

Prior to the Cluster mission, most of the past observations of ELF/VLF chorus have been made on single spacecraft [Lauben *et al.*, 2002 and references therein], with the exception of a large amount of chorus data collected from the ISEE 1 and 2 spacecraft, as reported by Gurnett *et al.* [1979a]. It was shown by Gurnett *et al.* [1979a] that simple comparison of chorus spectrograms indicated the size of the wave packets responsible for the chorus emissions to be less than a few hundred kilometers. In all of the data examined from ISEE 1 and 2, it was generally not possible to find a one-to-one correlation between any of the chorus elements, probably either because the

separation between these two spacecraft was often too large (up to several thousand kilometers), or that wideband data from both spacecraft were not simultaneously available in many cases when they were close (hundreds of kilometers).

The direction of the wave vector \mathbf{k} of observed chorus waves appears to be highly variable, with wave normal angle observations showing different results: According to *Goldstein and Tsurutani* [1984], at angular frequencies $\omega = 2\pi f < 0.3 \omega_{ce}$, wave normal angles are around 0° . According to *Hayakawa et al.* [1984], as also discussed by *Inan et al.* [1992], some emissions at $\omega < \omega_{ce}/2$ are generated near the equator at wave normal angles close to the resonance cone. According to *Lauben et al.* [2002], emissions at $\omega < \omega_{ce}/2$ have a value of ψ (the wave normal angle, the angle between \mathbf{k} and \mathbf{B}_0 , is more rigorously defined in section 1.3) close to the Gendrin angle [*Gendrin*, 1961] and emissions at frequencies $\omega > \omega_{ce}/2$ with a wave normal angle close to 0° .

Previous chorus observations, such as those documented by *Lauben et al.* [2002], suggest that the location of the source of chorus waves lies in the vicinity of the geomagnetic equator. *Lauben et al.* [2002] found that the generation of chorus waves occurs at wave normal angles for which the wave group velocity vector is parallel to the magnetic field lines. Such generation may occur at values of $\psi = 0^\circ$ or $\psi = \psi_G$, the so-called Gendrin angle [*Gendrin*, 1961]. Such wave normal angles lead to ray paths (i.e., direction of wave group velocity) that tend to stay parallel to the magnetic field lines for latitudes near the geomagnetic equator. For the cases studied by *Lauben et al.* [2002], the sources were found to be located in the vicinity of the geomagnetic equator, where the static magnetic field exhibits a minimum inhomogeneity. This is a result that agrees with other estimations of chorus source location [*Burtis and Helliwell*, 1969 and 1976; *LeDocq et al.*, 1998; *Santolík et al.*, 2003; *Parrot et al.*, 2003] to be within $-25^\circ < \lambda_m < 25^\circ$ in magnetic latitude of the geomagnetic equator. *Lauben et al.* [2002] concluded that sources located at large distances from the spacecraft must emit chorus waves at $\psi \simeq 0^\circ$ or $\psi \simeq \psi_G$. Waves propagating with other wave normal angles tend to diverge away from the field lines. Waves emitted at the Gendrin wave normal angle tend to remain more tightly focused and provide a more coherent illumination of points along a given field line over large distances than do waves at other angles, in the absence of field-aligned plasma irregularities. Furthermore, the

fact that the wave energy stays along the field lines to which the resonant electrons are also confined may be important in the generation mechanism of these emissions.

1.1.2 Proposed Mechanisms of Generation of Chorus

Although chorus has been studied for a number of decades, the generation mechanism of chorus waves is not yet understood. Discussion of early work on the mechanism of chorus can be found in review papers such as *Sazhin and Hayakawa* [1992]. More recent work on this topic is discussed in *Trakhtengerts* [1995 and 1999], *Trakhtengerts et al.* [2004] and *Nunn et al.* [1997]. It is generally believed that the mechanism of generation of chorus emissions involves a cyclotron resonance interaction between whistler-mode waves and energetic electrons in the vicinity of the geomagnetic equatorial plane [*Burtis and Helliwell*, 1969; *Burton and Holzer*, 1974; *LeDocq et al.*, 1998; *Lauben et al.*, 2002] in the inner magnetosphere outside the plasmasphere.

The close similarity between the spectral forms of chorus emissions and the artificially stimulated VLF emissions triggered by whistler mode waves within the plasmasphere [*Helliwell*, 1967] strongly suggests that both types of emissions are generated through the same mechanism. A phenomenological model to explain the artificially stimulated VLF emissions within the plasmasphere was described in *Helliwell* [1967] and later developed in *Helliwell and Crystal* [1973]. A model of triggered emissions based on phase trapping of energetic electrons was described by *Nunn* [1974b and 1990]. The general idea of cyclotron resonance interaction as the basic mechanism for both chorus and triggered emissions is supported by the works of, for example, *Bell* [1964a], *Brice* [1964], *Kennel and Petschek* [1966], *Tsurutani et al.* [1979] and *Isenberg et al.* [1982]. The authors of these studies conclude that the velocity-space anisotropy of the energetic electrons constitutes the energy reservoir for the emissions and the energy transfers from the energetic electrons to the wave through cyclotron resonance. *Burton and Holzer* [1974] and *Burton* [1976] also concluded that chorus is observed only when high anisotropy of the energetic electrons is present, supporting the general cyclotron resonance model.

Efforts to understand the underlying details of chorus generation based on cyclotron resonance have been extensively undertaken from a number of viewpoints. For example, *Nunn* [1974a and 1986] proposed that chorus is generated from pre-existing incoherent noise by mutual non-linear interactions between waves and resonant electrons, resulting in amplification of some waves and damping of others, producing the coherent group of waves that constitutes chorus. *Trakhtengerts* [1995 and 1999] and *Trakhtengerts et al.* [2004] proposed a new generation regime, based on the backwards wave oscillator mechanism for laboratory electronic devices. *Nunn* [1974a] proposed a theory for the generation of chorus based on non-linear trapping of energetic electrons. Part of this model has been used to explain certain features of discrete chorus waves via computer simulation [*Nunn et al.*, 1997], one important finding being that non-linear growth rates can be larger than linear ones by a factor of 2 to 5. However, it should be noted that such non-linear theories exclusively consider an absolute instability responsible for rapid wave growth everywhere in the source [*Trakhtengerts*, 1995; *Nunn et al.*, 1997; *Smith and Nunn*, 1998] and thus do not take into account the compact form [*Santolík et al.*, 2003 and 2004; *Santolík and Gurnett*, 2003] or any rapid motion [*Inan et al.*, 2004] of the source. In addition, non-linear trapping requires high wave field amplitudes, which are eventually attained by chorus elements at the termination of their rapid growth, but the spontaneous initiation of chorus emission must necessarily occur with much smaller wave fields, basically at the levels of ambient noise.

1.2 The Cluster Mission

This dissertation is based almost entirely on observations from the Cluster spacecraft [*Escoubet et al.*, 1997]. The Cluster mission consists of a group of four spacecraft, each with 11 instruments, in orbit around the Earth in close formation. Their orbit (illustrated in Figure 1.9) is designed to study different regions of the magnetosphere, with a $\sim 4 Re$ perigee, a $\sim 19.6 Re$ apogee, an inclination of $\sim 90^\circ$ and an orbital period of ~ 57 hrs. During all the Cluster passes shown in the present study, the spacecraft move northbound at a nearly constant dipole L shell at locations close to

the geomagnetic equator. The spacecraft separation varied between 200 km and 2000 km [Escoubet *et al.*, 1997].

The Cluster mission is planned and managed by the European Space Agency (ESA) and is part of an international activity organized by the Inter-Agency Consultative Group (IACG) consisting of ESA, The Institute of Space and Astronautical Science (ISAS, from Japan), The National Aeronautics and Space Administration (NASA) and the Russian Space Agency [Ferri and Warhaut, 1997]. The European Space Operations Center (ESOC) was in charge of the transfer of the four Cluster satellites into their operational orbits in the correct relative positions after their launch on June 4, 1996 for the first flight of the new Ariane-5 launcher. ESOC performs the combined operation of the four spacecraft and their payload throughout their in-orbit lifetime according to the mission requirements and the requests generated by the Principal Investigators (PIs) of each of the 11 Cluster experiments during the mission itself. ESOC also oversees the collection and transfer to the scientific community of all the raw science data generated by the payload instruments, in conjunction with selected spacecraft and mission auxiliary data. [Ferri and Warhaut, 1997]

Cluster instrumentation [Escoubet *et al.*, 1997] consists of a set of electric and magnetic antennas (two each) connected to 5 wave instruments, and a set of 6 particle instruments with their own sensors. The instruments used in this dissertation are three. First of all, the Wide Band Data (WBD) instrument [Gurnett *et al.*, 1997] which performs electric and magnetic field measurements of ELF/VLF waves and with which chorus emissions are observed. Also the Waves of High frequency and Sounder Probing of Electron density by Relaxation (Whisper) instrument [Décréau *et al.*, 1997], which stimulates plasma resonances by active sounding to determine plasma densities. And finally the Plasma Electron And Current Experiment (PEACE) instrument [Johnstone *et al.*, 1997] which performs energetic electron and ion flux measurements. The WBD instrument can be connected to any of the four antennas, but only one at a time. It can be used in several different modes, but for the purpose of this work and when acquiring chorus data, it was used exclusively in a mode with a bandwidth of 9.5 kHz in baseband, a time resolution of 37 μ sec (i.e., 27443 kHz sampling rate) and

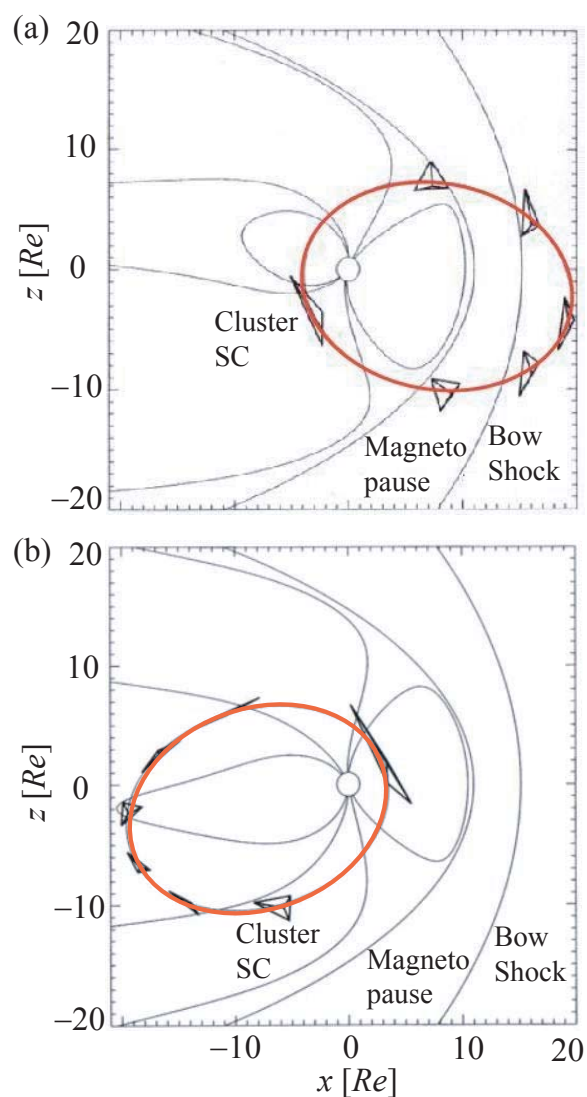


Figure 1.9: Cluster spacecraft orbit for two different configurations (a) with the perigee in the night-side, (b) with the perigee in the day-side. The spacecraft are located at the tips of the tetrahedrons (not to scale) located along the orbit in red. The coordinates are solar magnetic, the Sun is located to the right in both cases. Highlighted are the Magnetopause and Bow Shock. The other black lines represent the Earth's magnetic field.

a dynamic resolution of 8 bits [Gurnett *et al.*, 1997]. All the observations of chorus presented in this study are from perigee passes near the magnetic equatorial plane where chorus waves are usually observed.

1.3 A Review of Whistler Mode Propagation

Chorus waves propagate in the whistler mode, an electromagnetic propagation mode that occurs for waves with frequencies in the range of $\omega_{ce} > \omega > 0$ for $\omega_{pe} > \omega_{ce}$, and $\omega_{pe} > \omega > 0$ for $\omega_{ce} > \omega_{pe}$. The ω here is the angular wave frequency, ω_{pe} is the angular electron plasma frequency, proportional to the square root of the electron density, and ω_{ce} is the angular electron gyrofrequency, proportional to the magnitude of the Earth's static magnetic field \mathbf{B}_0 . In Figure 1.10a, a generalized plane wave packet is shown in an anisotropic medium such as the cold magnetized plasma of the inner magnetosphere. The wave packet consists of plane waves whose wave vector \mathbf{k} is always perpendicular to the wave fronts, i.e., surfaces of constant wave phase. In this type of medium, the wave vector and the direction of energy propagation, given by the direction of the group velocity vector \mathbf{v}_g , are usually not coaligned.

In the present work, the angle between the wave group velocity \mathbf{v}_g and the wave vector \mathbf{k} is denoted θ while the angle between the wave vector \mathbf{k} and \mathbf{B}_0 is denoted as ψ , and is often referred to as the wave normal angle. Since the angle ψ is defined in a 3D space, a fixed value of ψ does not completely define the direction of \mathbf{k} , without the knowledge of the azimuthal angle of the \mathbf{k} vector about \mathbf{B}_0 . For electromagnetic propagating whistler-mode waves, ψ can only have values $0 < \psi < \psi_{\text{res}}$, or $\pi - \psi_{\text{res}} < \psi < \pi$, where ψ_{res} is the wave normal angle at which the \mathbf{k} vector approaches infinity for propagation in the whistler mode at frequencies higher than the lower hybrid resonance ($\omega > \omega_{\text{LHR}}$). It should be noted that for $\psi = 0$, \mathbf{k} and \mathbf{B}_0 are parallel, while for $\psi = \pi$, \mathbf{k} and \mathbf{B}_0 are anti-parallel. The angle ψ is measured clockwise from the ambient static magnetic field \mathbf{B}_0 in the plane containing \mathbf{k} and \mathbf{B}_0 . The angle θ is measured counter-clockwise from \mathbf{k} in the same plane.

The refractive index vector \mathbf{n} is defined through the relation $\mathbf{n} = \mathbf{k}c/\omega$, and has the direction of \mathbf{k} , and the magnitude of the refractive index in the medium. The

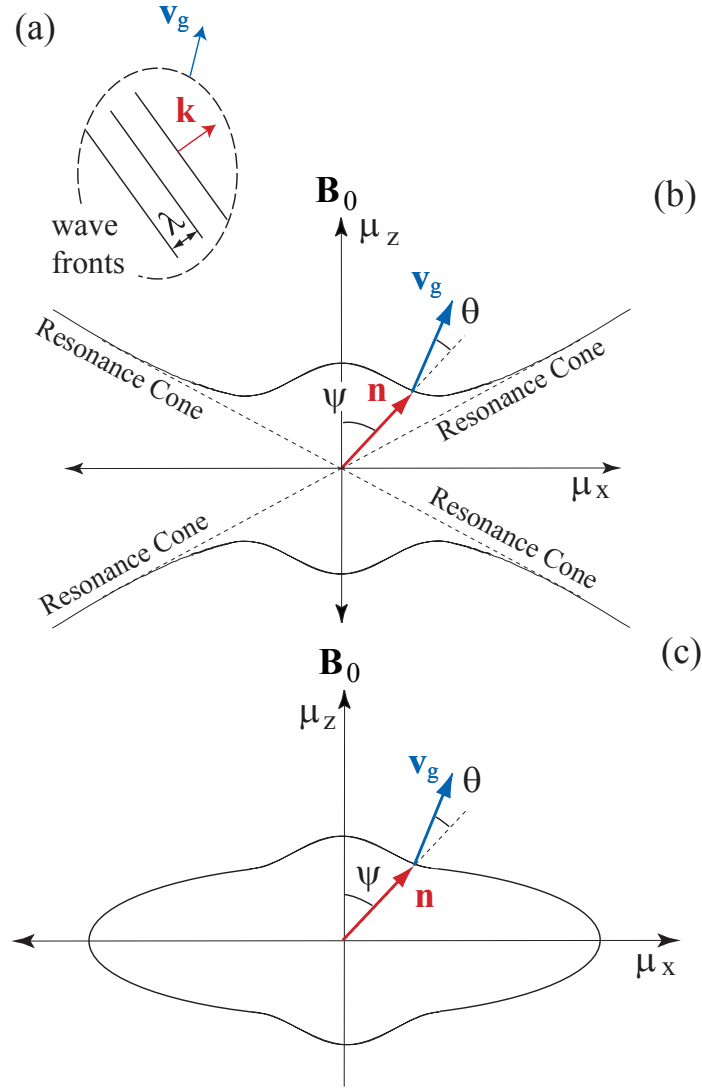


Figure 1.10: (a) A generalized whistler mode electromagnetic wave packet. The wave fronts are indicated in black solid lines, while the group velocity \mathbf{v}_g vector is indicated in blue and the wave vector \mathbf{k} in red. (b) Cross section of the refractive index surface for $\omega > \omega_{\text{LHR}}$. (c) Cross section of the refractive index surface for $\omega < \omega_{\text{LHR}}$. In both cases the x axis is perpendicular to \mathbf{B}_0 , while the z axis is parallel to \mathbf{B}_0 . The refractive index surface has rotational symmetry about the z axis.

magnitude of the refractive index vector is denoted by $\mu = |\mathbf{n}|$. The relationship between ψ , the direction of \mathbf{v}_g , and \mathbf{n} is represented by the refractive index surface, which is determined by the rotation around \mathbf{B}_0 of the curve obtained by plotting the tip of the \mathbf{n} vector at different values of ψ . The direction of propagation of the wave energy, given by the direction of the \mathbf{v}_g vector, is always perpendicular to the tangent of the refractive index surface at the tip of the \mathbf{n} vector for a given ψ , as shown in Figures 1.10b and 1.10c, for two different types of refractive index surfaces.

The surface in Figure 1.10b corresponds to the case usually observed in Cluster perigee passes near the geomagnetic equator, where the frequency ω of the observed waves is higher than the lower hybrid resonance frequency ω_{LHR} . In this case there is a maximum value of ψ for which whistler mode propagation is possible. This value of ψ is called the resonance cone angle (ψ_{res}). In Figure 1.10b, the refractive index surface is ‘open’, meaning that for certain values of ψ ($\psi_{\text{res}} < \psi < \pi - \psi_{\text{res}}$) whistler mode propagation is not possible, as is the case when $\omega > \omega_{\text{LHR}}$. In this parameter regime, for values of ψ close to the resonance cone (ψ_{res}), the wave becomes quasi-electrostatic and $k \rightarrow \infty$. Figure 1.10c corresponds to the case when the frequency ω of the observed waves is lower than the lower hybrid resonance frequency ω_{LHR} . In this case the refractive index surface is ‘closed’, there is no resonance cone, and the magnitude of the refractive index is bounded.

In a magnetized, collisionless plasma, as is the medium considered here, each charged particle of the plasma moves under the influence of the ambient \mathbf{B}_0 . For the perturbed state of the plasma, small-amplitude motions of the particles are considered under the influence of electromagnetic waves, and the magnitude of the oscillating magnetic fields induced by currents in the plasma is assumed to remain small compared to the magnitude of \mathbf{B}_0 . In this model of the cold plasma, it is assumed that the unperturbed values of density and composition of the plasma and the Earth’s magnetic field are static in time and uniform in space. Under these assumptions, the medium can be characterized by a dielectric tensor \mathbf{K} of the form [Stix, 1962, p. 10]:

$$\mathbf{K} = \begin{bmatrix} s & -i m & 0 \\ i m & s & 0 \\ 0 & 0 & p \end{bmatrix} \quad (1.1)$$

The p , s and m coefficients are obtained from the values of plasma frequency ω_{pu} and gyrofrequency ω_{cu} for each species u :

$$\begin{aligned} w &= 1 - \sum_u \left[\frac{\omega_{pu}^2}{\omega^2} \frac{\omega}{(\omega + \omega_{cu})} \right] \\ l &= 1 - \sum_u \left[\frac{\omega_{pu}^2}{\omega^2} \frac{\omega}{(\omega - \omega_{cu})} \right] \\ p &= 1 - \sum_u \left[\frac{\omega_{pu}^2}{\omega^2} \right] \\ s &= \frac{w + l}{2} \\ m &= \frac{w - l}{2} \end{aligned} \quad (1.2)$$

Transforming Faraday's and Ampere's laws via Fourier analysis in time and space, the electromagnetic wave equation can be derived for a magnetized cold plasma, yielding:

$$\mathbf{k} \times (\mathbf{k} \times \mathbf{E}) + \frac{\omega^2}{c^2} \mathbf{K} \cdot \mathbf{E} = 0 \Rightarrow \mathbf{n} \times (\mathbf{n} \times \mathbf{E}) + \mathbf{K} \cdot \mathbf{E} = 0 \quad (1.3)$$

Using the components of \mathbf{K} , the wave equation is reduced to a matrix equation which can be written as:

$$\begin{bmatrix} s - \mu^2 \cos^2(\psi) & -i m & \mu^2 \cos(\psi) \sin(\psi) \\ i m & s - \mu^2 & 0 \\ \mu^2 \cos(\psi) \sin(\psi) & 0 & p - \mu^2 \sin^2(\psi) \end{bmatrix} \cdot \mathbf{E} = 0 \quad (1.4)$$

The symbol i in equations (1.1) and (1.4) represents the imaginary unit i.e. $i = \sqrt{-1}$. In order to have a nontrivial solution ($\mathbf{E} \neq 0$), the determinant of the matrix in (1.4) must be equal to zero. This requirement yields a quadratic equation for μ^2

called the dispersion relation:

$$a \mu^4 - b \mu^2 + h = 0 \quad (1.5)$$

where:

$$\begin{aligned} a &= s \sin^2(\psi) + p \cos^2(\psi) \\ b &= w l \sin^2(\psi) + p s (1 + \cos^2(\psi)) \\ h &= p w l \end{aligned} \quad (1.6)$$

Solving the dispersion relation gives us the magnitude of μ^2 in terms of the plasma parameters [Stix, 1962, pp. 11, 38]:

$$\mu^2 = 1 - \frac{2(a - b + h)}{2a - b \pm \sqrt{b^2 - 4a h}} \quad (1.7)$$

where the (+) sign corresponds to the ordinary mode and the (−) sign corresponds to the extraordinary mode, the latter one being the one used in the calculations of this study (also called the ‘whistler’ mode). In the present dissertation we are not considering the effect of ions or other energetic particles besides electrons. Therefore, the magnitude of μ^2 can be simplified to a more familiar form in terms of ψ , ω , ω_{ce} and ω_{pe} , known as the Appleton-Hartree expression (for a cold magnetized plasma) [Helliwell, 1965, p. 23]:

$$\mu^2 = 1 - \frac{\left(\frac{\omega_{pe}}{\omega}\right)^2}{1 - \left[\frac{\omega_{ce}^2 \sin^2(\psi)}{2(\omega^2 - \omega_{pe}^2)}\right] \pm \sqrt{\left[\frac{\omega_{ce}^2 \sin^2(\psi)}{2(\omega^2 - \omega_{pe}^2)}\right]^2 + \left(\frac{\omega_{ce}}{\omega}\right)^2 \cos^2(\psi)}}$$

that is equivalent to (1.7) when only energetic electrons are considered. This equation can be simplified even further for quasi-parallel propagation ($\psi \simeq 0^\circ$), choosing the (−) sign for whistler mode propagation:

$$\mu^2 \simeq \frac{(\omega_{pe}/\omega)^2}{(\omega_{ce}/\omega) |\cos(\psi)| - 1} + 1$$

1.4 An Overview of Cyclotron Resonance

The cyclotron resonance interaction between discrete waves (e.g., triggered emissions or chorus) and energetic particles can be illustrated using the diagram introduced by *Helliwell* [1967], as shown in Figure 1.11. An electron with a given kinetic energy in the presence of a static magnetic field \mathbf{B}_0 tends to gyrate around the field lines, with its center of gyration drifting along \mathbf{B}_0 as shown in Figure 1.11b. When a group of these charged particles interacts with a whistler mode wave, they can become bunched in gyrophase, a process that is described in more detail in Chapter 4. Figure 1.11a adapted from *Helliwell* [1967] shows waves amplified by interaction with the energetic electrons in what is called an ‘interaction region’. During this process there is a net total radiating current different than zero at the local gyrofrequency. The motion of the particles along the z -axis parallel to \mathbf{B}_0 produces a Doppler shift in the frequency of the radiated wave, and if the wave is emitted in the opposite direction of the moving particles, there is a negative Doppler shift which allows the radiated wave to propagate in the whistler mode.

When spontaneously generated without an external triggering wave, these radiated waves are observed as what we call chorus in the whistler mode at frequencies below ω_{ce} . It is not yet clear as to why chorus is emitted as elements with rising or falling frequency, although *Helliwell* [1967] heuristically ascribed this behavior to the motion of the source with respect to the particle streaming direction and the location of the interaction region with respect to the geomagnetic equator, as discussed later in Chapter 6. *Helliwell* [1967] predicted a source motion at a velocity in the range between the group velocity of the wave in one direction and the parallel resonant velocity in the other. In the present dissertation, we take the frequency-time characteristics of chorus to be an inherent feature of the generation mechanism, and show such frequency change to be consistent with rapid drifts of the sources, for emissions

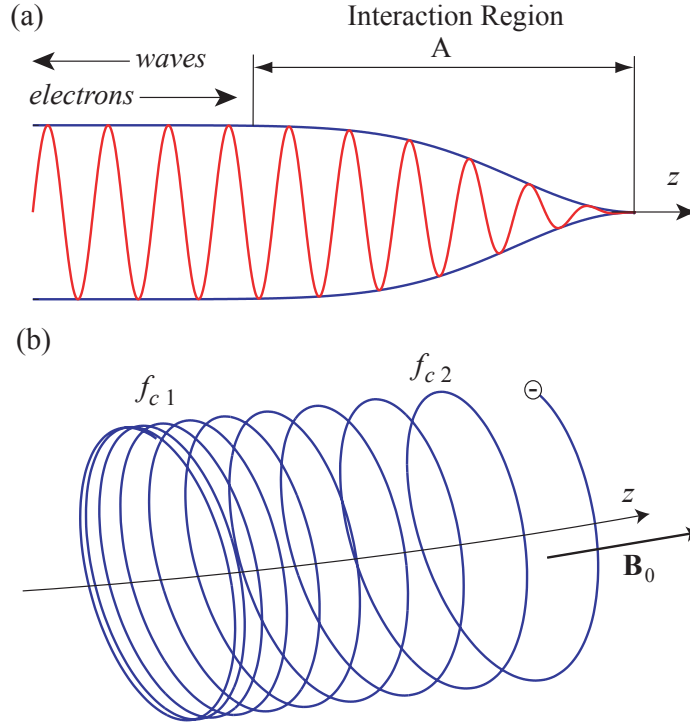


Figure 1.11: (a) Diagram of the wave-particle interaction during cyclotron resonance, adapted from Figure 2 in *Helliwell* [1967]. The z -axis is located along \mathbf{B}_0 . The ‘interaction region’ of length A is defined as the segment along z where waves are being amplified due to the gyrating motion of the electrons. (b) Gyration of an electron in the presence of a magnetic field \mathbf{B}_0 . The motion of the center of gyration to regions of lower (higher) \mathbf{B}_0 can cause the gyration frequency f_c to change from f_{c1} to a smaller (larger) value f_{c2} . The particle trajectory also changes its gyration radii inversely proportional to the magnitude of \mathbf{B}_0 changes, even though the change in (b) is not large enough to be noticeable.

that exhibit rapid growth and saturation.

Electrons gyrating about \mathbf{B}_0 during cyclotron resonance move along \mathbf{B}_0 at the resonant parallel velocity v_{\parallel} . The only waves which can propagate in the whistler mode (i.e. $\omega < \omega_{ce}$) are those radiated in the counterstreaming direction, i.e., a direction of propagation in which the wave motion is opposite to the motion of the particles. The energy and momentum exchange between the waves and energetic electrons are maximized when the resonance condition is satisfied for the particles having a parallel motion with a velocity v_{\parallel} , where:

$$v_{\parallel} = \frac{\omega - \omega_{ce}}{k} \quad (1.8)$$

This motion with velocity v_{\parallel} produces a Doppler shift that is negative for waves propagating in the opposite direction.

1.5 Overview and Contributions

In this dissertation, a general formulation is developed for unambiguous determination of the chorus source and its speed of motion based on measurements of the same discrete emissions on 4 spacecraft. The model described previously by *Inan et al.* [2004] is expanded and generalized to three dimensions, relaxing the original assumptions and demonstrating that the location of the source can be identified by taking into account the simultaneous wideband (waveform) observations of chorus waves by four Cluster spacecraft in regions near the geomagnetic equator at a radial distance of $\sim 4.5 Re$. This analysis is mainly based on high-resolution measurements with the wideband (WBD) wave instrument [*Gurnett et al.*, 2001], data from the Whisper sounders [*Décrou et al.*, 2001] to determine the local plasma density, and the measurements of particle flux from the PEACE instrument [*Johnstone et al.*, 1997], to infer energetic particle velocity distribution function from data using a method described by *Bell et al.* [2000]. For the four cases presented and studied in the following chapters, the observed motion of the chorus source is qualitatively characterized using a model of cyclotron resonance wave growth and the known properties of whistler

mode chorus waves. The contributions of this work can be succinctly summarized as follows:

1. A new method is developed for three dimensional determination of the location and motion of radiating sources in an anisotropic medium.
2. The location and rapid motion of compact sources of whistler-mode chorus emissions are determined for several selected cases.
3. An interpretation is provided of the rapid motion of chorus sources in terms of other known properties of chorus emissions, such as anisotropy-driven cyclotron resonant exponential growth, phase bunching and saturation.

Chapter 2

Estimation of Chorus Source Location

‘Thin-lipped wisdom spoke at her from the worn chair, hinted at prudence, quoted from that book of cowardice whose author apes the name of common sense.’ ¹

‘Eppur si muove...’ ²

2.1 Doppler Shift due to Source Motion

Before introducing specific observations and their quantitative interpretation, the Doppler shifts that are expected to result from source motion are considered, in order to demonstrate that this effect could lead to the observation of individual wave packets (emanating from the same source) at different frequencies on two different spacecraft. The method by which we use the measured values of differential Doppler shift and time delay to determine the location of the chorus source as a function of time is then described.

¹Oscar Wilde, *The Picture of Dorian Gray*, first published as a novel in 1891

²‘And yet it moves...’.- Galileo Galilei, as he left the Inquisition trial against his blasphemous claims about the Earth and the Sun. Well, he may not actually have said it, in fact it would have been extremely dangerous for him to do that, but he most certainly thought it.

Consider a compact source located at $z_S = S_Z(t)$, $x_S = 0$, (S_Z is a function of time only) emitting electromagnetic waves at a frequency $\omega(t)$ while moving along \mathbf{B}_0 at a speed $v_S = dS_Z/dt$ in a homogeneous medium. For simplicity, it is assumed that \mathbf{k} is in the $x-z$ plane with the z -axis along \mathbf{B}_0 and the x -axis perpendicular to \mathbf{B}_0 . In a homogeneous medium, the signal phase $\varpi(\psi, t)$ observed on a spacecraft located at x, z is given by:

$$\varpi = \int_0^t \omega(t) dt - k_x(\psi, t) x - k_z(\psi, t) [z - S_Z(t)] \quad (2.1)$$

where ψ is the wave normal angle, i.e., the angle between the \mathbf{k} -vector and the static magnetic field \mathbf{B}_0 . The observed frequency is thus given by:

$$\frac{d\varpi}{dt} = \omega(t) - \underbrace{\left[\frac{x}{v_{gx}(\psi, t)} - \frac{z - S_Z(t)}{v_{gz}(\psi, t)} \right] \frac{\partial \omega}{\partial t}}_{\text{Normal Propagation Delay}} + \underbrace{k_z(\psi, t) \frac{\partial S_Z(t)}{\partial t}}_{\text{Doppler Shift}} \quad (2.2)$$

where the spacecraft motion is neglected and it is assumed that the wave-normal angle ψ remains constant over the relatively short propagation path from the source to the observer. The spacecraft motion can be neglected for normal spacecraft velocities (~ 5 km/sec), since the Doppler shift due to spacecraft motion is very small (< 1 Hz) for refractive index values $\mu < 500$.

The geometry for the observation of same chorus waves at different frequencies by different observers due to differential Doppler shift is illustrated in Figure 2.1 for two general cases. The simplest case is described in Figure 2.1a, for a medium which is ideal and isotropic, with the refractive index being constant and the direction of propagation of the wave energy being the same as the direction of the wave vector. Four receivers located at different points in space can observe four different frequencies emitted by a moving source. The difference in frequency between that of the observed wave and that of the emitted wave is equal to the dot product of the source velocity vector \mathbf{v}_S and the \mathbf{k} vector, i.e., $\omega_i - \omega = \mathbf{k}_i \cdot \mathbf{v}_S = \omega \mu_i v_S \cos(\psi_i)/c$, for each observer SC i ($i=1, \dots, 4$). In an isotropic medium (Figure 2.1a), any frequency differences at different observers can only result due to the geometry, i.e., due to the fact that the angle ψ is different for different observers. In an anisotropic medium like a magnetized

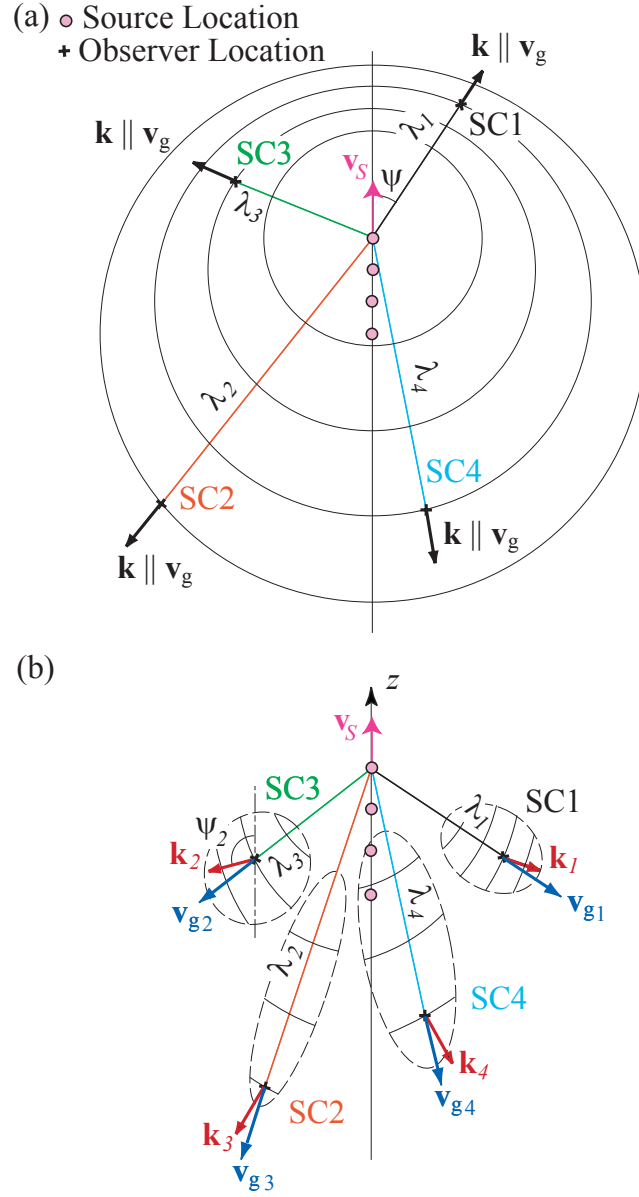


Figure 2.1: Diagram of the frequency Doppler shift observed in four different locations in space by four spacecraft SC1 to SC4. The ray path to each observer is highlighted in a different color. The curved solid black lines represent wavefronts. (a) Wave propagation in an ideal isotropic medium. Wave group velocity vector \mathbf{v}_g and wave vector \mathbf{k} are aligned (b) Wave propagation in an anisotropic medium such as the magnetized collisionless inhomogeneous cold plasma of the inner magnetosphere. Wave group velocity vector \mathbf{v}_g and wave vector \mathbf{k} are not necessarily aligned and the magnitude of \mathbf{k} is a function of ψ .

plasma shown in Figure 2.1b, the wave cannot propagate in all directions. In this kind of medium the same expression is valid as long as μ_i is real. The angle ψ_i is the observed wave normal angle if the coordinate system is chosen in such a way that one of the axes along which \mathbf{B}_0 is oriented parallel to the source velocity \mathbf{v}_S . In this anisotropic medium, the different values of refractive index and corresponding wave normal angles at each observer must also be taken into account. Doppler shift can now result not only due to the different values of ψ for different observers, but also because the magnitude of \mathbf{k} is a function of ψ .

The black circles in Figure 2.1a represent wave fronts or crests (i.e., surfaces of constant phase shown as contour lines perpendicular to the wave vector \mathbf{k} at each point in space) of the radiated electromagnetic wave, and the corresponding wave length λ at a given location is illustrated. Wave fronts are also drawn in Figure 2.1b as black curves within each of the four wave packets that are observed at each SC j , with their corresponding observed wavelength λ_i , for $i = 1, \dots, 4$. As illustrated in Figure 2.2a, waves emanating from a compact source can reach two different observers SC1 and SC2 only by propagating at two different wave normal angles ψ_1 and ψ_2 , and are thus observed at two different ‘apparent’ frequencies ω'_1 and ω'_2 , where:

$$\Delta\omega = \omega'_1 - \omega'_2 = [k_z(\psi_1, t) - k_z(\psi_2, t)] \frac{\partial S_Z(t)}{\partial t} \quad (2.3)$$

It is evident from Figure 2.2b that the observed differential Doppler shift $\Delta\omega$ would be relatively small for cases in which (i) all of the sources are at large distances (e.g., compared to the spacing between observers) from the observers, and (ii) the two observers are close to one another (compared to the distance between them and the sources). If the source has a large spatial extent perpendicular to \mathbf{B}_0 , the resulting beamwidth of the radiating pattern can be too narrow to have emitted waves with \mathbf{k} that have significant components perpendicular to \mathbf{B}_0 . In such a case, the frequency difference produced by Doppler shift observed at two different locations in space would be very small. To further quantify the transverse extent of the sources, note that any finite extent (perpendicular to \mathbf{B}_0) of source(s) limits the observability of chorus in planes perpendicular to \mathbf{B}_0 , independent of accessibility issues due to limited group

velocity directions. Assume, for example, source currents (which radiate the chorus emissions) to be pointing in the same direction distributed over a circular region of radius r (perpendicular to \mathbf{B}_0). Assume further that the radiation produced at any given time (at a given frequency) originates from radiating currents distributed only over a distance of $\Delta z \ll \lambda$ along \mathbf{B}_0 , where λ is the wavelength along \mathbf{B}_0 . The currents within the circular region represent an array of sources of electromagnetic waves, with an array factor that will increase with r , decreasing the transverse size of the beamwidth of the resulting radiation pattern of the distributed sources along the circle of radius r . Observation of significant differential Doppler shifts on the Cluster spacecraft can generally occur if the radius r of the region is of the order of a wavelength λ or less, but the actual value of r depends on the signal to noise ratio at the receiver. If this ratio is large, the waves with large Doppler shift may still be detectable even when r is large.

Given the fact that the underlying mechanism for generation of ELF/VLF chorus is believed to be the cyclotron resonance interaction, and assuming that the velocity of the ‘source’ of the radiation is of the same order as the velocity of the counter-streaming electrons moving at the parallel resonant velocity v_{\parallel} (even though this is not necessarily the case as discussed later), the magnitude of the differential Doppler shift may be estimated by taking the source velocity to be given by the cyclotron resonance condition (1.8), rewritten here for parallel propagation ($\psi = 0$):

$$v_S = -v_{\parallel} = \frac{\omega_{ce} - \omega_0}{k_0} \simeq \frac{(\omega_{ce} - \omega_0)^{3/2}}{\omega_{pe} \omega_0^{1/2}} c \quad (2.4)$$

where ω_{pe} and ω_{ce} are the electron plasma and gyrofrequencies respectively, $k_0 = k_z(\psi = 0)$, and the last equality holds when $\mu^2 \gg 1$. The subindex 0 refers to waves with \mathbf{k} vector in the direction of the Earth’s magnetic field line. (Note that the source velocity is adopted here to be equal to the resonant parallel velocity solely for the purposes of an initial evaluation of the Doppler shift as shown in Figure 2.2). The last term of equation (2.4) is obtained replacing $k_0 = \mu_{\psi=0} \omega / c$, where $\mu_{\psi=0}$ can be obtained from (1.7) by setting $\psi = 0$. From (2.4), the Doppler shift ω_D is then given by:

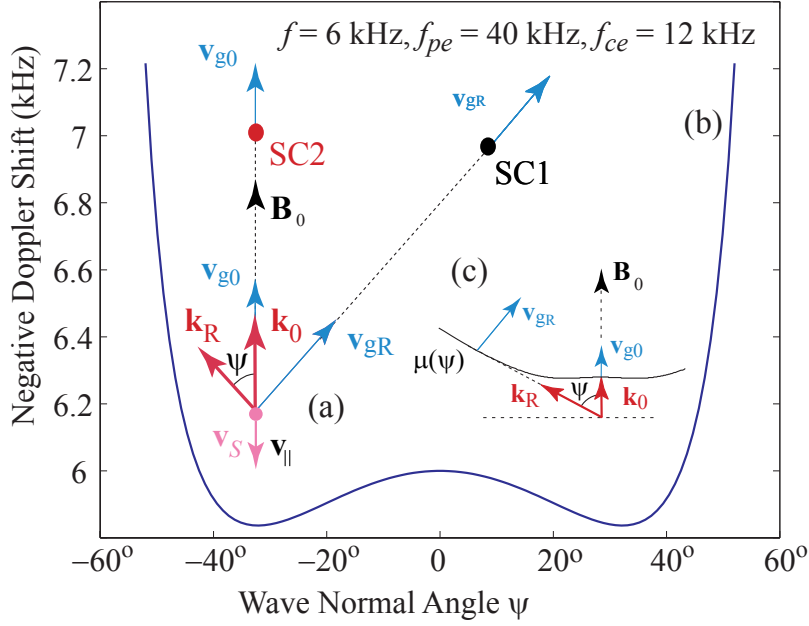


Figure 2.2: (a) Placement of the source location with respect to the Cluster spacecraft; (b) Doppler shift as a function of the wave normal angle ψ . Calculation assumes an electron plasma frequency of 40 kHz and an electron gyrofrequency of 12 kHz. Results are shown for a source frequency of 6 kHz and for a source velocity assumed (only for the purposes of this plot) to be equal to the parallel velocity of gyroresonant electrons. (c) The refractive index surface, and the corresponding orientations of the wave group velocities \mathbf{v}_g and wave vector \mathbf{k} at $\psi = 0$ (labeled \mathbf{v}_{g0} and \mathbf{k}_0 , respectively) and for $\psi \simeq \psi_{\text{res}}$, i.e., the resonance cone angle (labeled \mathbf{v}_{gR} and \mathbf{k}_R , respectively).

$$\omega_D = -k_z v_S = -\omega \mu_z \left[\frac{(\omega_{ce} - \omega_0)^{3/2}}{\omega_{pe} \omega_0^{1/2}} \right] \simeq -\omega \mu \cos(\psi) \left[\frac{(\omega_{ce} - \omega_0)^{3/2}}{\omega_{pe} \omega_0^{1/2}} \right] \quad (2.5)$$

where ω refers to the frequency of the wave with \mathbf{k} vector at an angle ψ with respect to the Earth's magnetic field line, and the refractive index μ is given by (1.7). The Doppler shift calculated using (2.3), (2.4), (2.5), and (1.7) for the case of $f_{ce} = 12$ kHz, $f_{pe} = 40$ kHz, and for $\omega_0/2\pi = f_{ce}/2 = 6$ kHz is shown in Figure 2.2a as a function of wave-normal angle ψ . Also shown plotted as a function of ψ in Figure 2.2c is the magnitude of the refractive index μ . Noting that the cold plasma parameters chosen are representative of the Cluster observations presented in later chapters, two points at different values of ψ can be picked (e.g., $\psi_1 = 40^\circ$ and $\psi_2 = 50^\circ$) from Figure 2.2b to show that even for refractive index values $\mu < 100$ (for both ψ_1 and ψ_2), Doppler shifts observed at different wave normal angles ψ_1 and ψ_2 can differ by as much as ~ 1.2 kHz. Two observers, SC1 and SC2, would in general observe any discrete chorus wave packets emitted at the source at slightly different times, in view of the known dependence of the whistler-mode group velocity on wave normal angle ψ . Such a differential time delay would in general be expected to be present whenever a differential Doppler shift is observed, although the reverse is not necessarily the case, noting that differential time delay would also be observed if both spacecraft were along the field line of the source (in which case they would observe the waves with identical Doppler shift) but displaced in the direction along the field line. It is also useful to note that a differential Doppler shift would result in those cases when the two observers SC1 and SC2 are displaced (with respect to one another) in the direction perpendicular to the local magnetic field \mathbf{B}_0 . The differential Doppler shift and time delay are only function of the wave normal angle ψ .

2.2 Previous Work on Moving Sources of Chorus

The motivation for this study originates from Cluster observations of chorus emissions on November 27, 2000, first reported by *Gurnett et al.* [2001] and interpreted by *Inan*

et al. [2004]. A set of these emissions is shown in Figure 2.3, adapted from *Inan et al.* [2004].

The case studied in *Inan et al.* [2004] was from a time when the Cluster spacecraft passed through perigee at a radial distance of $3.85 R_e$, at 06:42 MLT, and close to the magnetic equatorial plane, when the two spacecraft observed with their respective WBD instruments the same set of chorus emissions at different frequencies. These two point observations were used to estimate the location of the source and its motion in 2D space [*Inan et al.*, 2004], assuming that one of the spacecraft was located close to the magnetic field line intersecting the source. Observations from the WBD instruments onboard Cluster spacecraft 1 and 2 showed the same chorus waves with a shift in frequency (In Figures 2.3 and 2.4, the spectrograms show the starting time and geomagnetic coordinates of each spacecraft on the top).

Figure 2.4a shows the basic principle of the *Inan et al.* [2004] model, where a compact source is assumed to be located along the same field line as one of two satellites (SC2), so that waves emanating at $\mathbf{k} \parallel \mathbf{B}_0$ (i.e., $\psi = 0$) reach SC2 propagating with a refractive index $\mu_{\psi=0}$ and a group velocity v_{g0} . The second satellite (SC1) is displaced in longitude and/or latitude as well as L -shell, so that it is accessible from the same compact source only by waves emanating at a relatively large wave normal angle ψ , corresponding to a refractive index $\mu(\psi) > \mu_{\psi=0}$ given by equation (1.7) (subscript index 0 is used for parameters corresponding to waves traveling parallel to the static magnetic field \mathbf{B}_0 ; the parameters with no subscript index correspond to waves traveling at a nonzero wave normal angle ψ).

Figure 2.4b shows chorus emissions observed on spacecraft SC1 and SC2, highlighting the significant frequency differences observed on the two spacecraft and the differential time delay between the two spacecraft. Highlighted are the frequency span of each element f_s as well as their duration in time t_d . The differences in time between the points at the lower frequency end ($f = 6.9$ kHz on SC2) and the highest frequency end ($f = 8.75$ kHz on SC2) of the observed elements in both spacecraft are indicated as Δt . The black lines along each element in the top and lower spectrograms indicate the linear dispersion of each element at each spacecraft (SC1 on the top spectrogram and SC2 in the lower one), overlaying the spectral shape observed

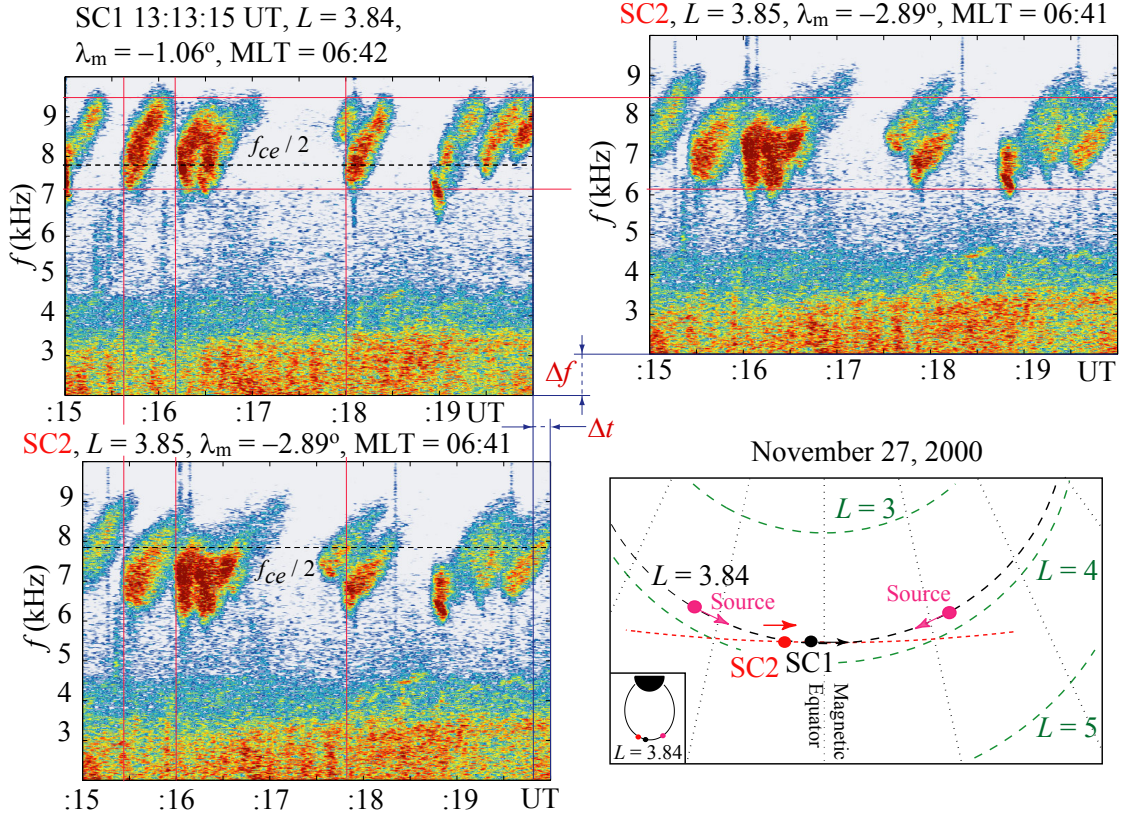


Figure 2.3: Spectrograms of 5-sec duration, starting at 13:13:15 UT, on November 27, 2000, showing a sequence of individual chorus elements observed on both Cluster SC1 and SC2. The SC2 panel is repeated on the right to illustrate the differential Doppler shift. Also shown in the bottom right panel, is the location of the spacecraft with respect to the two possible source locations (as derived from our analysis) along the field line. The small panel on the bottom left of this diagram shows the source location with respect to the Earth.

in the other spacecraft on top as a red dashed line (SC2 on the top spectrogram and SC1 in the lower one).

According to (2.3) the source velocity v_S is related to the measured differential Doppler shift $\Delta\omega$ as:

$$v_S = \frac{\Delta\omega}{\Delta k_z(\psi)} = \frac{c\Delta\omega}{[\omega\mu_R \cos(\psi) - \omega\mu_{\psi=0}]} \quad (2.6)$$

The difference between refractive indexes μ_R and $\mu_{\psi=0}$ and the group velocities \mathbf{v}_{gR} and \mathbf{v}_{g0} resulting from the difference of the wave normal angles of the waves received at SC1 and SC2 is observed as a difference in frequency and time of arrival at each spacecraft. Two spacecraft can thus observe individual waves originating from the same compact source at two different apparent frequencies differing from each other by a given amount of the differential Doppler shift. According to this model, different observers would in general observe any discrete chorus wave packets emitted at the source at slightly different times, based on the dependence of the whistler-mode group velocity on wave normal angle ψ . Differential Doppler shift would result in those cases when the observers are displaced (with respect to one another) either in the radial or longitudinal direction, or both. At relatively short distances from the source, when the whistler-mode raypaths can be taken to be simple straight lines, the differential Doppler shift and time delay are only a function of the wave normal angle ψ . It is useful to enumerate here the primary conclusions and observations of *Inan et al.* [2004]:

1. The magnitude of observed differential Doppler shift and time delay are consistent with model calculations for source velocities, comparable in magnitude to either the absolute values of particle parallel velocity or the wave group velocity.
2. Discrete chorus emissions appear to be produced by sources that are compact (one wavelength in size or less) in the direction perpendicular to \mathbf{B}_0 .
3. Different frequencies of individual discrete chorus elements are emitted at different points along the field line. Multiple, simultaneously active source(s) are likely distributed in L -shell and longitude (and latitude), continually emitting

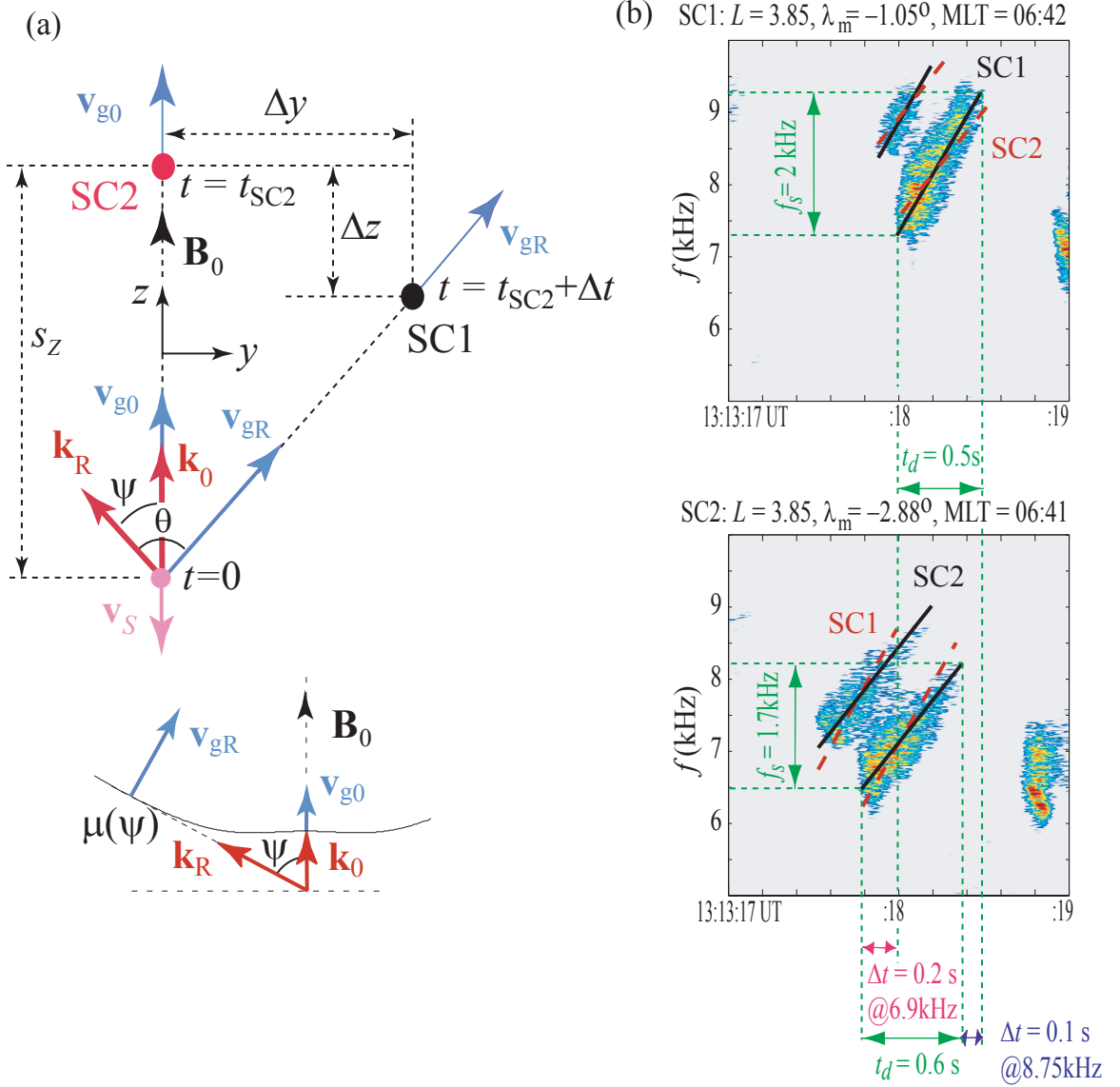


Figure 2.4: (a) Parameters involved in the determination of the source location with respect to the Cluster spacecraft. Highlighted are the two spacecraft SC1 and SC2, as well as the pertinent vector magnitudes of group velocity \mathbf{v}_g , wave vector \mathbf{k} and source velocity \mathbf{v}_S . For the case shown, the wave arrives first at SC2 at time $t = t_{SC2}$ and later at SC1 at time $t = t_{SC2} + \Delta t$. Included is a plot of the calculated refractive index surface at different wave normal angle values. (b) Detailed measurement of differential Doppler frequency shift and time delay between two Cluster spacecraft for chorus elements with increasing frequency (risers) on November 27, 2000, at 13:13:18 UT.

waves.

In the context of the *Inan et al.* [2004] model, sources of emissions are compact in the direction transverse to the field line while moving along the field line. *Santolík et al.* [2003] and *Santolík and Gurnett* [2003] examined the April 18, 2002 case which was also analyzed by *Inan et al.* [2004]. Relatively small differential Doppler Shifts of ~ 24 Hz were deduced by *Inan et al.* [2004] for this case, consistent with the fact that the spacecraft were located very close (< 180 km) to one another. While the purpose of *Santolík and Gurnett* [2003] analysis was also to determine the source characteristics, a completely different approach was used by these authors. The results of *Santolík et al.* [2003] primarily concern the propagation and internal fine structure of chorus elements, while *Santolík and Gurnett* [2003] present a correlation analysis of chorus spectrograms to estimate the transverse dimensions of chorus wave packets. Differences in fine structure of the chorus elements analyzed in *Santolík et al.* [2003] can in principle be used to explain the small frequency changes observed during April 18, 2002 between chorus waves observed simultaneously in the four Cluster spacecraft. The results show fine structure inside the individual chorus elements, which is discernibly different on each spacecraft, possibly involving differences in instantaneous frequencies observed on different spacecraft. Using a parametric waveform analysis method, several examples given by *Santolík et al.* [2003] show instantaneous frequency with a resolution better than 10 Hz, so that differences of ~ 24 Hz as deduced by *Inan et al.* [2004] are also resolvable with this method [*O. Santolík, private communication*].

The interpretation of frequency differences between individual discrete chorus elements observed on different Cluster spacecraft in terms of Doppler shifts resulting from source motion is consistent with an overall disposition of chorus sources as shown in Figure 2.5. The left panel of Figure 2.5 shows a view of the inner magnetosphere and the locations in MLT where different types of plasma waves are observed, plasmaspheric VLF hiss, electromagnetic ion cyclotron ELF waves and ELF/VLF chorus, typically observed in the dawn side, extending from midnight to noon. Within the macroscopic source of chorus, a so called ‘bubbling’ structure of elemental chorus sources is envisioned; a region of different simultaneously active compact sources

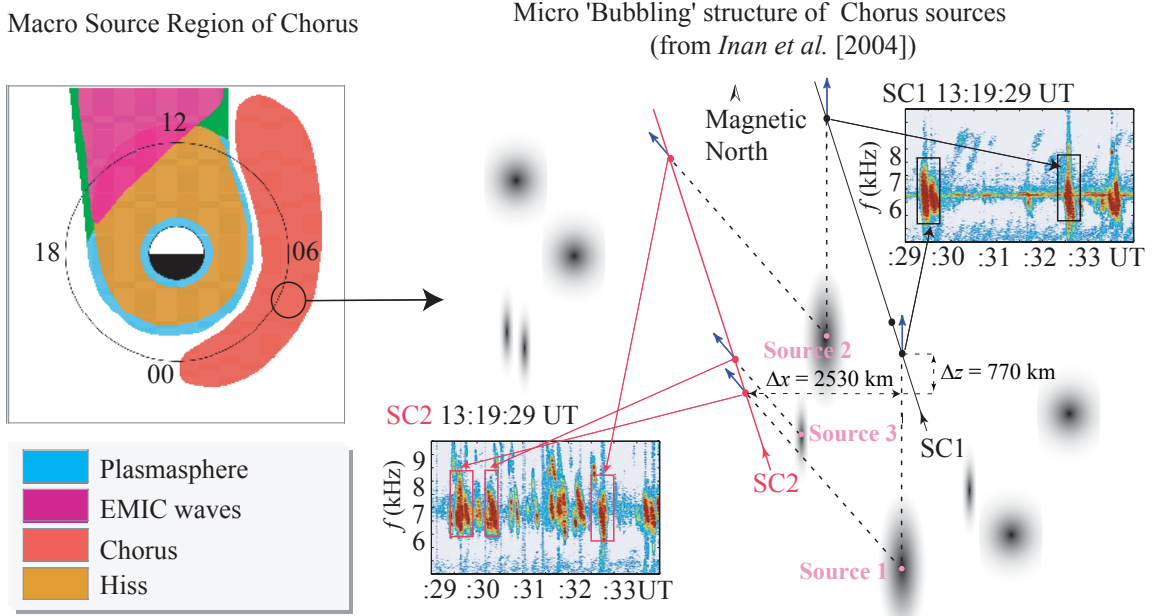


Figure 2.5: Proposed model of different localized sources of ELF/VLF chorus. The left-hand panel shows the regions in the magnetosphere where chorus waves are observed. The Sun is located in the plane of the paper beyond the top edge in the figure. The right-hand panel shows a zoom in on the dawn sector where chorus is usually observed. Data from 11/27/2000 on the Cluster spacecraft using the WBD instrument is shown. Highlighted are the trajectories of Cluster spacecraft SC1 and SC2 and the points where the emissions are observed.

emitting at different instantaneous times in different directions. Each active compact source is assumed to be moving along the Earth's magnetic field line. As described in this example, two spacecraft crossing this region in a fixed orbit can sometimes observe the same waves emanating from the same source, depending on whether the ray paths from the source reach the spacecraft orbit at the time of the observation or not, as highlighted in the spectrograms. The other chorus elements on the spectrograms that are only observed on one spacecraft or the other emanate from other sources, the rays from which reach only one spacecraft because of their respective locations.

The narrow blue boundary in Figure 2.5 represent the outer limits of the plasmasphere. Actually, the plasmasphere is comprised of the entire region inside those

strips, not including the Earth, but this blue region is overlapped by the brown region representing the locations in space where plasmaspheric hiss is observed (usually inside the plasmasphere) [Burtis, 1974].

In the present work, these 2D results of *Inan et al.* [2004] are expanded and generalized to 3D, using calculations based on source triangulation for wave propagation in the whistler mode, as explained in detail below.

2.3 Determination of Source Location and Velocity in 3D from Measured Differential Doppler Shift and Time Delay

In the present work, we relax the assumption of *Inan et al.* [2004] that one of the observing spacecraft is positioned along the same magnetic field line as the source. A wave at frequency $\omega(t)$, emanating from a compact source located at S_Z , while moving along \mathbf{B}_0 at a speed \mathbf{v}_S in a homogeneous medium, can reach two different observers SC*i* and SC*j* only by propagating at two different wave normal angles ψ_i and ψ_j , and is thus observed at two different ‘apparent’ frequencies ω'_i and ω'_j , where the difference in frequency obtained from (2.3) can now be expressed for any *i* and *j* as:

$$\Delta\omega_{i,j} = \omega'_i - \omega'_j = [k_z(\psi_i, t) - k_z(\psi_j, t)] \frac{\partial S_Z(t)}{\partial t} \quad (2.7)$$

where ψ is the wave normal angle, i.e., the angle between the \mathbf{k} -vector and the static magnetic field \mathbf{B}_0 . (The z -axis is assumed to be parallel to \mathbf{B}_0). In the system of coordinates used for the calculations in this study, the origins of the x and y -axis lie in the center of the Earth and the z coordinate has its origin at the geomagnetic equator. The positive x points in the sunward direction. All distances along the z -axis are measured from the geomagnetic equator along the Earth’s magnetic field lines. The location of the corresponding magnetic field line is determined by their x – y coordinates as distances to the Earth at the geomagnetic equator plane. Even though

the lines along z in Figures 2.6, 3.3b, 3.4b, 3.5, 3.7, 5.3b, 5.4b, 5.5, 5.6, 5.7 and 5.8 are straight lines, they correspond to curves along the field lines of \mathbf{B}_0 in a regular geomagnetic system of coordinates. Distances across the field line are assumed to be perpendicular to z . Therefore, the reader should assume all parallel lines in the z directions to be magnetic field lines as identified by their $x-y$ coordinates at the geomagnetic equator. Distances across z , given by x are taken to be perpendicular to z for locations close to the geomagnetic equator, i.e., for geomagnetic latitudes $\lambda_m \simeq 0^\circ$, noting that they are strictly perpendicular only at $\lambda_m = 0^\circ$. We note that our calculations in Chapters 3 and 5 lead to chorus source locations along z to be in the vicinity of the equator. This result is consistent also with that found in other works (i.e. the source geomagnetic latitudes obtained that result from our calculations are within $-25^\circ < \lambda_m < 25^\circ$).

The maximum error introduced by the adopted coordinate system in the results presented in Chapters 3 and 5 can be quantified by measuring the distance from a point $\mathbf{a}_1 = [x_1 \ y_1 \ z_1]$, $x_1 = 29000$ km, $y_1 = 0$ km, $z_1 = 7000$ km and a point $\mathbf{a}_2 = [x_2 \ y_2 \ z_2]$, $x_2 = 28400$ km, $y_2 = 0$ km, $z_2 = 0$ km, at which the absolute difference between the coordinates x_1 and x_2 is 600 km and that between z_1 and z_2 is 7000 km, representing the situations encountered in Cases 1 to 4 described in Chapters 3 and 5. Distances in our defined coordinate system are calculated as in a regular Cartesian system where the distances along axes x , y or z are perpendicular to each other, while in the geomagnetic coordinate system, distances along z are calculated by integrating along the corresponding magnetic field line (assuming a centered dipole configuration) and distances across x and y are only perpendicular to z at the geomagnetic equator. For the above mentioned case, the difference between the calculated distances in a geomagnetic coordinate system and our coordinate system is no more than $\sim 7\%$. The calculation of percent error mentioned in the previous sentence is performed by estimating the distances in our coordinate system and the actual distance in a geomagnetic coordinate system where points a_1 and a_2 are located in what should be the equivalent geomagnetic locations for the given values of $[x_1 \ y_1 \ z_1]$ and $[x_2 \ y_2 \ z_2]$.

It is assumed that the source emits waves at different values of wave normal angle with magnitudes smaller than the resonance cone angle, and that those wave packets

with a specific value of ψ_i reach the corresponding SC*i* spacecraft. This assumption is then applied to all of the possible i, j combinations of frequency difference that can be observed with 4 spacecraft, i.e., six possible combinations, at a given frequency $\omega(t)$. The spacecraft motion can be neglected for typical spacecraft velocities (~ 5 km/sec), since the Doppler shift due to spacecraft motion is very small (< 1 Hz) for refractive indexes of magnitudes below 500. To a first approximation, the wave-normal angle ψ is assumed to remain constant over the relatively short propagation path from the source to the observer. This assumption is later verified using raytracing for all the four cases considered here. When the distance from the source to the spacecraft becomes close to $1Re$, as in our Case 2 illustrated below, the wave normal angle obtained is corrected using raytracing, estimating the correct value of it for the given distance and by recalculating this distance. From Equation (2.7), the measurements of differential Doppler shift ($\Delta\omega_{i,j}$) between spacecraft SC*i* and SC*j* are used to estimate the value of the source velocity v_S :

$$v_S = \frac{c\Delta\omega_{i,j}}{\omega\mu_i \cos(\psi_i) - \omega\mu_j \cos(\psi_j)} \quad (2.8)$$

noting that we must satisfy the premise of having the same frequency ω at the source location, i.e., the frequency observed at SC*i*, ω'_i , must be equal to the frequency ω at the source plus the Doppler shift $\Delta\omega_i$. This condition can be satisfied by adding another set of equations to be satisfied for each of the four spacecraft SC*i*, namely:

$$\omega' = \omega + \Delta\omega_i = \omega + \omega\mu_i \frac{v_S}{c} \cos(\psi_i) \quad (2.9)$$

The six equations obtained from (2.8) and the four resulting from (2.9), are part of the system of equations used to calculate the position of the source at a given frequency ω . The two sets are not independent, i.e., (2.8) can be derived from (2.9). Nevertheless, due to the non-linear nature of the equations involved, the inclusion of both sets is necessary for the numerical calculation, since a solution can be found that does comply with one set but not the other one. The value of the refractive index μ_i is uniquely given by the following relation for whistler-mode waves [Stix, 1962, p. 38]:

$$\mu_i^2 = 1 - \frac{2(a_i - b_i + h)}{2a_i - b_i - \sqrt{b_i^2 - 4a_i h}} \quad (2.10)$$

The parameters a , b and h are obtained from:

$$\begin{aligned} a_i &= s \sin^2(\psi_i) + p \cos^2(\psi_i) \\ b_i &= w l \sin^2(\psi_i) + p s (1 + \cos^2(\psi_i)) \\ h &= p w l \end{aligned} \quad (2.11)$$

where w , l , p and s are obtained from the values of plasma frequency ω_{pu} and gyrofrequency ω_{cu} for each species u using equations (1.2).

Expressions (2.10) and (2.11) are the same as (1.7) and (1.6) respectively, rewritten here with subindexes i corresponding to each observer SC*i*. Our calculations apply to frequencies near $\omega_{ce}/2$ for which ion effects are negligible; therefore, $u = e$ (for ‘electron’) and the corresponding electron plasma frequency and electron gyrofrequency was used. In the rest of the article the u subscript is omitted so that we refer to these quantities simply as ω_p and ω_c . A similar construction to (2.8) and (2.9) can be carried out for the time delay ($\Delta t_{i,j}$), using the observed time difference between spacecraft SC*i* and SC*j*, leading to another group of six equations of the form:

$$\Delta t_{i,j} = \frac{d_i}{v_{gi}} - \frac{d_j}{v_{gj}} \quad (2.12)$$

where d_i is the distance traveled by the wave from the source to the spacecraft SC*i*, and the magnitude of the group velocity v_{gi} can be found from $v_{gi} = |d\omega_i/d\mathbf{k}_i|$. However, for wave vectors whose direction is quasi-parallel to \mathbf{B}_0 , i.e., for $0^\circ < \psi < 15^\circ$ and $165^\circ < \psi < 180^\circ$, it is convenient to use a simpler expression for v_{gi} as the quasi-longitudinal approximation [Helliwell, 1965, p. 41] for $0^\circ < \psi_i < 15^\circ$:

$$v_{gi} \simeq \frac{2c\sqrt{\omega/\omega_c}}{\omega_p/\omega_c} \sqrt{\frac{\tan^2(\psi_i)(\cos(\psi_i) - \omega/\omega_c)}{4} + \frac{(\cos(\psi_i) - \omega/\omega_c)^3}{\cos^2(\psi_i)}} \quad (2.13)$$

and for $165^\circ < \psi_i < 180^\circ$:

$$v_{gi} \simeq \frac{2c\sqrt{\omega/\omega_c}}{\omega_p/\omega_c} \sqrt{\frac{\tan^2(\pi - \psi_i) (\cos(\pi - \psi_i) - \omega/\omega_c)}{4} + \frac{(\cos(\pi - \psi_i) - \omega/\omega_c)^3}{\cos^2(\pi - \psi_i)}} \quad (2.14)$$

Finally, to complete the set of equations, the geometry of the satellite locations with respect to the source must be taken into account. To illustrate this, Figure 2.6 shows the distance vectors \mathbf{d}_i in different colors, from two different points of view, and the corresponding location of the source with respect to the spacecraft. The magnitude of S_Z is the projection of the distance from the geomagnetic equator to the location of the source, taken to be along the field line.

The distance from the source to the satellites is assumed to be small enough to consider the propagation paths as straight lines. We also neglect the spacecraft motion, since it is small compared to the wave group velocity. The distance from the source to the spacecraft d_i is noted, as well as the trajectory traveled by the wave toward each spacecraft, which has an angle with respect to the static magnetic field (z -axis) of $\theta_i - \psi_i$. The angle θ_i represents the angle between the group velocity vector \mathbf{v}_{gi} and \mathbf{k}_i . A simple approximate expression for θ_i for the quasi longitudinal case is given by [Helliwell, 1965, p. 41] for $0^\circ < \psi_i < 15^\circ$:

$$\theta_i \simeq \cos^{-1} \left[\frac{1 - \frac{\omega}{\omega_c \cos(\psi_i)}}{\sqrt{\frac{\tan^2(\psi_i)}{4} + \left(1 - \frac{\omega}{\omega_c \cos(\psi_i)}\right)^2}} \right] \quad (2.15)$$

and for $165^\circ < \psi_i < 180^\circ$:

$$2\pi - \theta_i \simeq \cos^{-1} \left[\frac{1 - \frac{\omega}{\omega_c \cos(\pi - \psi_i)}}{\sqrt{\frac{\tan^2(\pi - \psi_i)}{4} + \left(1 - \frac{\omega}{\omega_c \cos(\pi - \psi_i)}\right)^2}} \right] \quad (2.16)$$

The angles ψ_i are measured clockwise from the ambient static magnetic field \mathbf{B}_0 in the plane containing \mathbf{k} and \mathbf{B}_0 . The angles θ_i are measured counter-clockwise from \mathbf{k} , in the plane defined by \mathbf{v}_g and \mathbf{k} . Equations (2.13) and (2.15) from Helliwell [1965] are applicable for wave normal angles $0^\circ < \psi < 15^\circ$. According to our definition

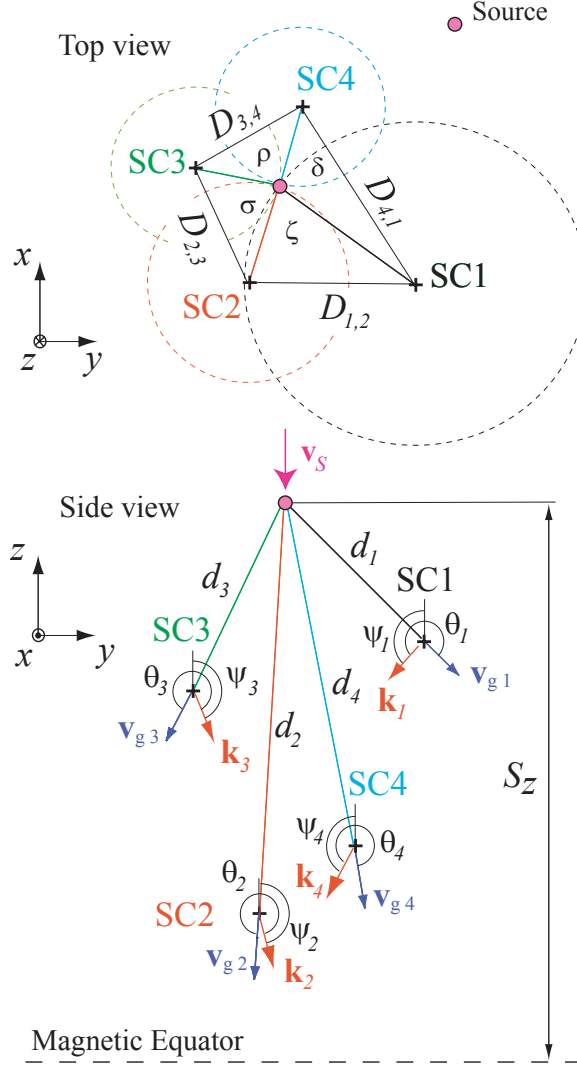


Figure 2.6: Schematic of the chorus emission model of a moving source, traveling along a magnetic field line. The top panel represents the top view of the system while the lower panel represents the side view. For $i = 1, \dots, 4$, shown are the wave normal angles ψ_i , distance to the source, d_i , wave vectors \mathbf{k}_i , source velocity v_s , the distances perpendicular to the magnetic field lines $D_{i,j}$ between spacecraft, the source location, given by the angles ζ , σ , ρ , δ and S_Z , the component along the field line of the distance from the geomagnetic equator to the source. The dashed circles represent all the points for each spacecraft where a source can be located for a given set of ψ_i values. The intersection of the four of them, in conjunction with S_Z , determines the unique location of the source.

of ψ these equations could not be used if $165^\circ < \psi < 180^\circ$, as happens in Case 2, described in Chapter 3. However, we know that the solution μ of equation (1.7) for a given ψ is identical to that for $180^\circ - \psi$. If we observe carefully the dependence of (1.7) on ψ , as is expressed in the set of equations (1.6), we observe that ψ appears in those expressions only as the argument of sines and cosines raised to the square power. This fact implies that the behavior of (1.7) is exactly the same for ψ as it is for $180^\circ - \psi$, simply because $\cos^2(\psi) = \cos^2(\pi - \psi)$ and $\sin^2(\psi) = \sin^2(\pi - \psi)$. Therefore, these equations redefined for $165^\circ < \psi_i < 180^\circ$ as (2.14) and (2.16) changing the sign of the z -axis can be used. For the cases where the estimated value of ψ falls outside the mentioned ranges, the full expression of $v_{gi} = |d\omega_i/d\mathbf{k}_i|$ is used. Notice that even though in Figure 2.6 some of the ψ_i and θ_i angles seem to be measured clockwise and some counterclockwise, this is not actually the case. The definition of these two angles is formulated in a 3D space and Figure 2.6 show a projection in 2D of the diagram into two different planes. The planes containing \mathbf{k} and \mathbf{B}_0 used in the definition of ψ , and the one defined by \mathbf{v}_g and \mathbf{k} used for the definition of θ can both rotate around \mathbf{B}_0 . Therefore the views in Figure 2.6 do not necessarily coincide with these two planes containing the corresponding angles.

Along the z -axis, parallel to \mathbf{B}_0 , the projection of the trajectory of the waves backward from each spacecraft must intersect at a single point, i.e., at the source location. This condition is fulfilled by the set of equations:

$$S_Z = z_{SCi} - d_i \cos(\theta_i - \psi_i) = z_{SCj} - d_j \cos(\theta_j - \psi_j) \text{ for } i \neq j \quad (2.17)$$

The value of z_{SCi} is measured as the projection of the vector location of each spacecraft along the z -axis, with respect to a reference. For our calculations $x = 0$ and $y = 0$ is at the center of the Earth while the $z = 0$ position is located at the geomagnetic equator on the L -shell of interest. The values of z_{SCi} are the projection along the z -axis of the distance between each spacecraft and the geomagnetic equator, in our coordinate system. Equation (2.17) implies another set of four equations. In the x - y plane, at the source location S_Z , the trajectories of the waves converge to one point, the field line of the source, defined by the angles ζ , σ , ρ and δ . As observed in

Figure 2.6, the solution of this set of equations lies in the intersection of four circles, each corresponding to all of the points which are a possible solution of equations (2.8), (2.9), (2.12) and (2.17) for a given set of values of d_i , ψ_i , θ_i , S_Z , and which define a unique point in space in the $x-y$ plane intersecting the \mathbf{B}_0 field line at S_Z . This point is then completely specified by the angles ζ , σ , ρ , δ as follows:

$$\begin{aligned}
D_{1,2}^2 &= d_1^2 \sin^2(\theta_1 - \psi_1) + d_2^2 \sin^2(\theta_2 - \psi_2) - 2|d_1 \sin(\theta_1 - \psi_1) d_2 \sin(\theta_2 - \psi_2)| \cos(\zeta) \\
D_{2,3}^2 &= d_2^2 \sin^2(\theta_2 - \psi_2) + d_3^2 \sin^2(\theta_3 - \psi_3) - 2|d_2 \sin(\theta_2 - \psi_2) d_3 \sin(\theta_3 - \psi_3)| \cos(\sigma) \\
D_{3,4}^2 &= d_3^2 \sin^2(\theta_3 - \psi_3) + d_4^2 \sin^2(\theta_4 - \psi_4) - 2|d_3 \sin(\theta_3 - \psi_3) d_4 \sin(\theta_4 - \psi_4)| \cos(\rho) \\
D_{4,1}^2 &= d_4^2 \sin^2(\theta_4 - \psi_4) + d_1^2 \sin^2(\theta_1 - \psi_1) - 2|d_4 \sin(\theta_4 - \psi_4) d_1 \sin(\theta_1 - \psi_1)| \cos(\delta)
\end{aligned} \tag{2.18}$$

$$\zeta + \sigma + \rho + \delta = 2\pi$$

where $D_{i,j}$ is the distance between spacecraft SC*i* and SC*j* projected on the $x-y$ plane, shown in Figure 2.6.

Now our system of equations is completely specified by the six equations from (2.8), the four equations from (2.9), the six equations from (2.12), the four equations from (2.17) and the five equations from (2.18). The 15 unknowns for this system of 25 equations are: the frequency of the wave at the source ω , the source velocity v_S , the four distances from the source to the spacecraft d_i , the four wave normal angles ψ_i , the angles ζ , σ , ρ , δ and the source location S_Z . This system of equations, even though over-specified, gives us the opportunity to take into account any errors that may exist in the measured parameters of the background plasma, such as ω_c and ω_p as well as the measured values of frequency, time, and spacecraft location.

Data from the Whisper sounder instrument [Décr  au *et al.*, 1997] onboard the four Cluster spacecraft is used to measure the plasma density and therefore the plasma frequency ω_p , and the spacecraft magnetometer to obtain the value of \mathbf{B}_0 , and ω_c [Balogh *et al.*, 1997]. These values have an inherent error of approximately $\pm 10\%$ for ω_p and $\pm 1\%$ for ω_c , which is taken into account in the solution of our system of equations. This system of equations is solved using a minimum square error approach, with the initial values of the variables determined by trial and error, and with the constraints

$|\omega_c - \omega_{co}|/\omega_{co} < 0.01$ and $|\omega_p - \omega_{po}|/\omega_{po} < 0.1$, where ω_{po} and ω_{co} are the observed values of the plasma and the electron gyrofrequency respectively. The differences in the uncertainties of ω_c and ω_p are due to the difference in the methods applied to obtain them: the onboard magnetometer for ω_c and the Whisper observations for ω_p .

Chapter 3

Source Location and Velocity Results for Cases 1 and 2

‘The human mind is not capable of grasping the universe. We are like little children entering a huge library. The walls are covered to the ceilings with books in many different languages. The child knows that someone must have written these books. He does not know who or how. He does not understand the languages in which they are written. But the child notes a definite plan in the arrangement of books: a mysterious order which he does not comprehend, but only dimly suspects’¹

3.1 Observations on July 24, 2003

In this section, observations of chorus on all four Cluster spacecraft on July 24, 2003, are presented, specifically from two regions before and after the spacecraft crossing of the geomagnetic equator. This particular perigee pass was selected because the spacecraft crossed the equator around $L \simeq 4$, with a spacecraft separation of no more than 500 km. The time and frequency differences between chorus elements on different spacecraft were obtained using the method of visual overlaying of 10-second long spectrograms, similar to the analysis performed by *Inan et al.* [2004]. The

¹Albert Einstein

time resolution of the WBD measurements of the electric field [Gurnett *et al.*, 1997] is $\sim 37 \mu\text{sec}$, while the spectral-overlay method (with 10-second long spectrograms) yields a time and frequency resolution (for the identification of individual chorus element features) respectively of $\sim 10 \text{ msec}$ and $\sim 10 \text{ Hz}$.

3.1.1 Geomagnetic Conditions

The geomagnetic K -index [Bartels *et al.*, 1939] is related to the maximum fluctuations of the horizontal component of \mathbf{B}_0 observed on a magnetometer relative to a quiet day, during a 3-hour interval. The conversion table from maximum fluctuation of \mathbf{B}_0 (in nT) to K , varies from observatory to observatory in such a way that the historical rate of occurrence of certain levels of K are about the same at all observatories. In practice this means that observatories at higher geomagnetic latitude require higher levels of fluctuation for a given K -index. The maximum positive and negative deviations during the 3-hour period are added together to determine the total maximum fluctuation. These maximum deviations may occur anytime during the 3-hour period. The official planetary K_p index is derived by calculating a weighted average of K -indexes from a network of geomagnetic observatories around the world. The maximum K_p index observed in the 24 hours prior to the events studied in Cases 1 and 2 was 3^+ . The notation of a plus sign after the number means that the actual value is more than 3, but less than 3.5. This notation is used in K_p displays since the actual value does not have more than 1 significant digit. The variation of the geomagnetic activity for this period is presented in Figure 3.1a, showing the K_p index during the day before and up to two days after the observed events shown in this study. The geomagnetic activity is relevant to the present study because it has been shown in previous studies [Smith *et al.*, 2004 and references therein] that there is a direct relation between enhanced chorus activity and geomagnetic storms and substorms. In general, chorus activity is observed during and after periods of medium and high geomagnetic activity ($K_p > 3$). Chorus waves may be observed in space and on the ground [Meredith *et al.*, 2001].

Data from the Whisper resonance sounder [Décr  au *et al.*, 1997] was used to derive

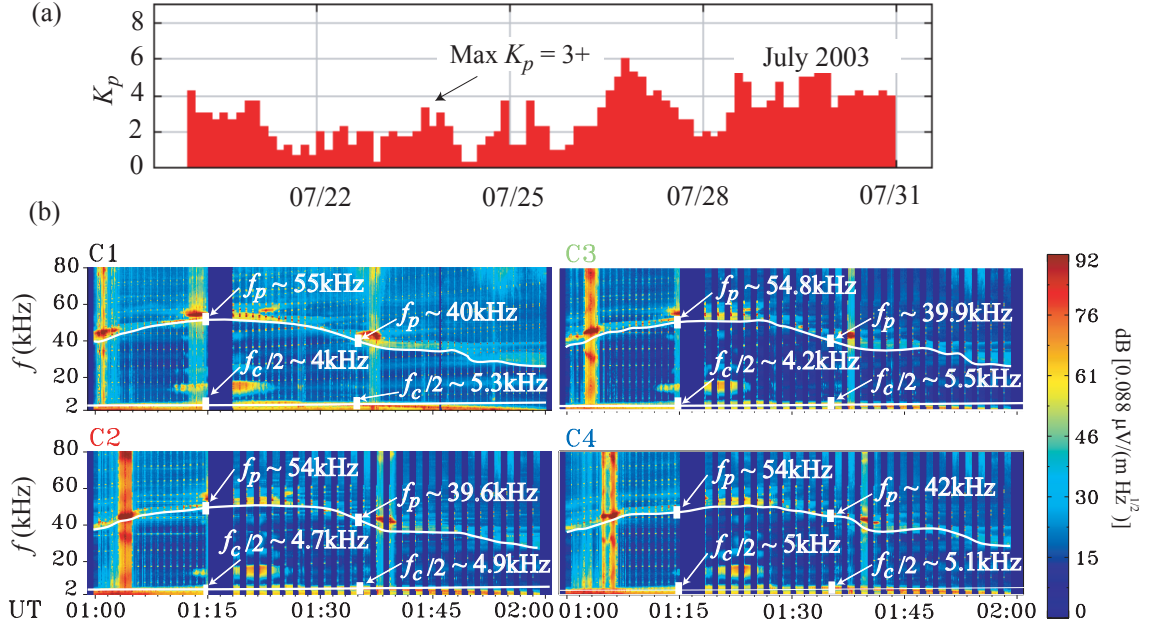


Figure 3.1: (a) Geomagnetic activity index (K_p), for the last week of July, 2003. Highlighted is the local maximum in the K_p index value, as observed in the 24 hours previous to the observations in Figure 3.2. (b) Whisper overview spectrogram of the Cluster satellite pass during July 24, 2003, starting at 01:00:00 UT. The color scale is related to the magnitude of the electric field in dB, measured with respect to a value given by $0.088 \mu\text{V}/(\text{m}\sqrt{\text{Hz}})$. The y -axis indicates frequency, and the x -axis indicates universal time (UT). Highlighted in white are plots showing the plasma frequency f_p and one half of the electron gyrofrequency $f_c/2$ observed in each spacecraft, and the corresponding values used for the calculations in Cases 1 and 2 respectively.

values of local plasma density. Frequency-time spectrograms generated from electric field measurements using the Whisper instrument in the passive mode [Décréau *et al.*, 1997] are shown in Figure 3.1b. The four panels show spectrograms of one of the components of the electric field on spacecraft SC1, SC2, SC3 and SC4, for the pass on July, 24, 2003. The Whisper sounder on the Cluster spacecraft can provide an absolute measurement of the total plasma density within the range $0.2 - 80 \text{ cm}^{-3}$, which cover the range of typical values of electron plasma density observed in the inner magnetosphere near $4 < L < 5$, especially outside the plasmasphere where chorus is typically observed. The data from this instrument allows the identification of the electron plasma frequency by analyzing the time-frequency patterns of resonances excited in the medium by a pulse transmitter. The sounding technique used for this purpose was developed earlier and proved successful in these regions of the magnetosphere by Trotignon *et al.* [1986]. In the basic nominal operational mode, as is the case presented in this study, the density is measured every 52 seconds on SC1. On SC2, SC3 and SC4, it is measured in the same manner during the first 15 minutes of each pass and every 104 seconds during the rest of the time, the frequency and time resolution for the wave measurements being about 300 Hz and 2.2 seconds. These active and passive measurements were used to obtain the electron density through the method specified by Canu *et al.* [2001] and Trotignon *et al.* [2001 and 2003].

3.1.2 WBD Observations

Figure 3.2 shows an overview of the plasma wave electric field observed on the four Cluster spacecraft by the WBD instrument during July 24, 2003. Highlighted in black are the regions of interest for the two cases studied, Case 1 beginning at 01:14:38 UT and Case 2 beginning at 01:35:25 UT. The four spectrograms presented in Figure 3.2 correspond to each of the four Cluster spacecraft, each measuring the same component of the wave electric field. The horizontal axis shows the universal time, as well as the geomagnetic coordinates (the L parameter, MLT, the geomagnetic latitude λ_m , as well as the radial distance R_e) of spacecraft SC4 along the path.

Figure 3.3c consists of four spectrograms of 4 seconds duration, one for each

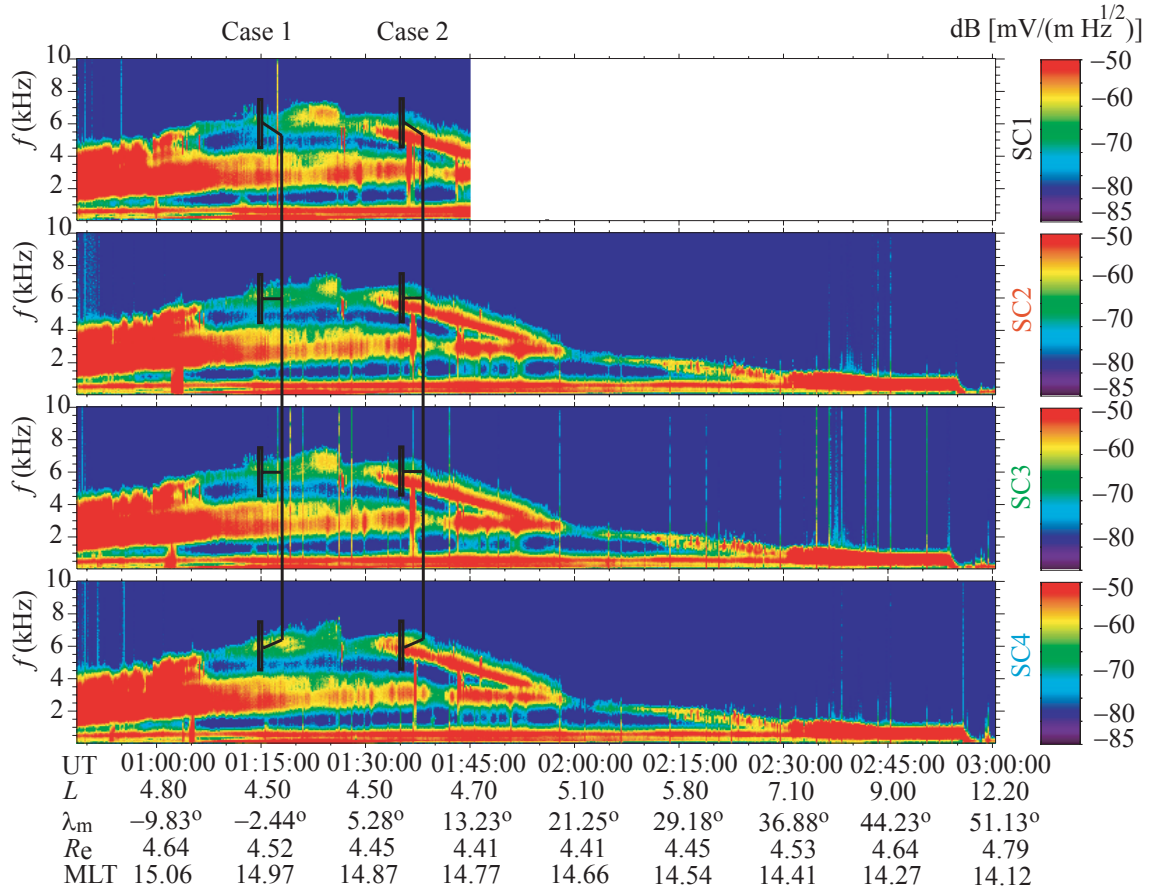


Figure 3.2: WBD overview spectrogram of the Cluster satellite pass during July 24, 2003, starting at 00:49:00 UT. The color scale is related to the magnitude of the plasma wave electric field in dB with respect to $1 \text{ mV}/(\text{m}\sqrt{\text{Hz}})$. The y -axis indicates frequency, and the x -axis indicates universal time (UT), as well as position information for spacecraft SC4, in terms of the L parameter, geomagnetic latitude λ_m , geomagnetic local time MLT and radial distance to the center of the Earth, R_e . Highlighted are the two elements studied in Cases 1 and 2 respectively.

spacecraft, showing data from the region highlighted in Figure 3.2 for Case 1, at 01:14:38 UT. These elements were observed before the geomagnetic equator crossing during this pass. Chorus emission activity was observed on all four spacecraft SC1, SC2, SC3 and SC4. The frequency-time spectrogram displays upper band chorus emissions as observed by the four spacecraft, showing individual elements occurring at different times and frequencies. One particular chorus element observed on all four spacecraft is targeted for study herein, as indicated by four white circles. The spacecraft positions with respect to one another are displayed in Figure 3.3b, in the system of coordinates defined in the previous Chapter. The vector pointing in the direction perpendicular to the page, pointing toward the reader, represents an arrow that shows the direction at which the Earth is located with respect to the spacecraft in that plot. Figure 3.3a shows the location of the spacecraft in the frame of reference of the geomagnetic field, using the L parameter and the geomagnetic latitude λ_m as a coordinate system.

As discussed earlier in Chapter 2, in connection with Figure 2.5, in general wide-band data such as that shown in Figure 3.3c from multiple spacecraft shows a multiplicity of chorus elements, only some of which are individual chorus elements having distinctly similar frequency and time sequencing on different spacecraft, such that they can be assumed to be emanating from the same source. In Figure 3.3c, one particular single element is divided into four points (shown as solid white circles) regularly spaced in time and frequency along the element. The first point is selected at the earliest time when the amplitude of the element reaches the maximum amplitude level (red) at ~ 30 dB (for Cases 1 and 2) or ~ 35 dB (for Cases 3 and 4 shown in Chapter 5) above the background noise level (given by the lowest intensity in the dB color scale). The last point is selected using the same amplitude criteria at the latest time along the element. The intermediate points are selected by dividing the time between the first and last points in regular intervals. Starting from the first point at the earliest time, each sequential point on each spacecraft is assumed to emanate from the same source at the same time. Each point has a corresponding value of frequency and time, so that for each point, the time and frequency differences between the four

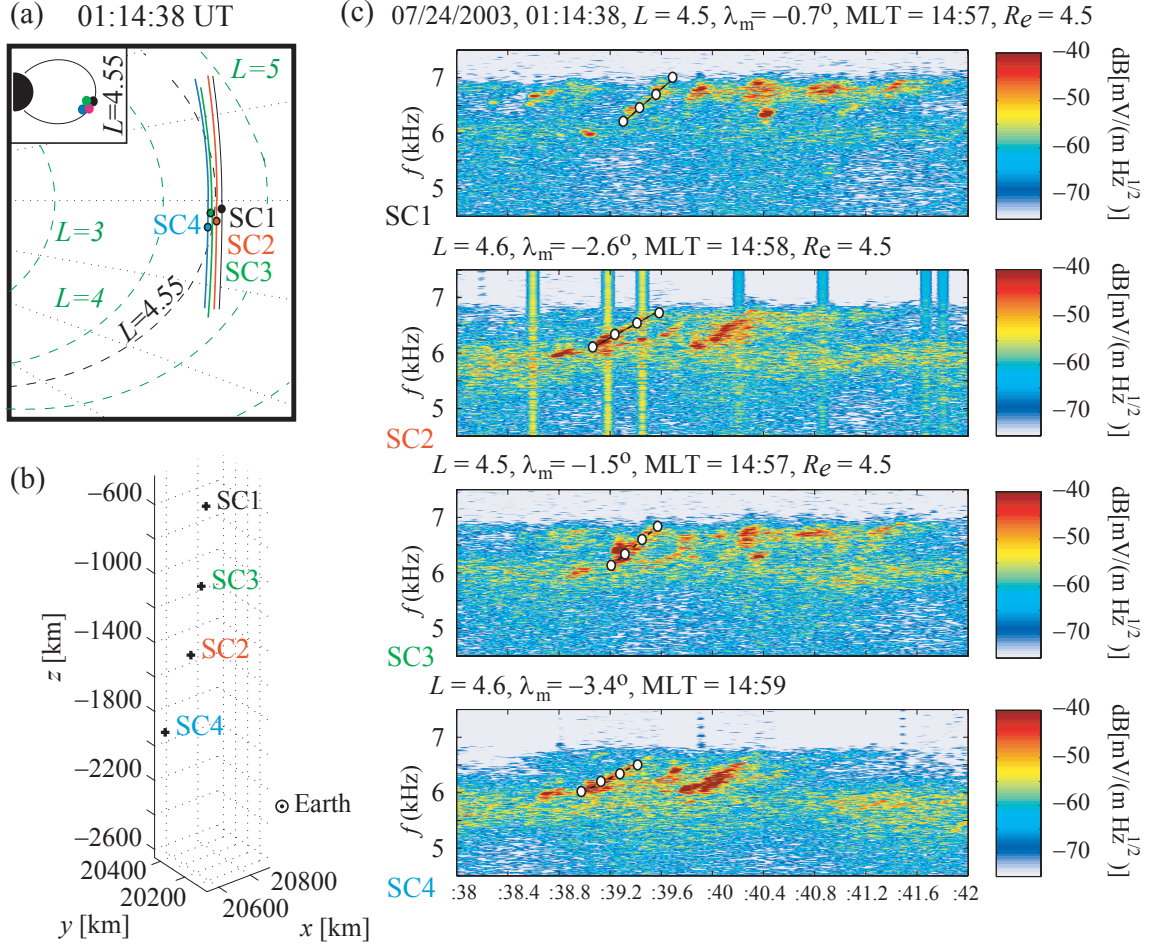


Figure 3.3: (a) Spacecraft location along the orbit for July 24, 2003. Indicated are the lines of constant L (dashed lines), and geomagnetic latitude λ_m (dotted lines). Highlighted are the spacecraft locations at the place in orbit where the observations were performed. (b) Relative position of the spacecraft with respect to each other in space. The system of coordinates in this panel is defined in Chapter 2 (c) Four second spectrograms of electric field data observed by the four Cluster spacecraft, starting at 01:14:38 UT. The color scale is related to the magnitude of the electric field in dB with respect to $1 \text{ mV}/(\text{m}\sqrt{\text{Hz}})$. The vertical axis indicates frequency, while the horizontal axis indicates time in UT. Highlighted (with white circles across its frame) is the chorus element studied in Case 1.

spacecraft are determined as follows: The time and frequency differences in the vertical and horizontal scales of each spectrogram between each point in one spacecraft are compared with the corresponding one in the other spacecraft. The accuracy of this graphical method depends on the resolution in frequency and time of the spectrogram which in our case is 10 msec and 10 Hz. The difference in slope between such similar elements observed at different frequencies is also apparent in Figure 3.3c. This difference is the result of whistler mode propagation, which introduces dispersion in time, as noted in *Inan et al.* [2004], and can be explained in terms of the dependence of the group velocity of whistler-mode waves on the wave-normal angle ψ .

The determination of the chorus source location can now be undertaken by relaxing the assumption of having one of the spacecraft aligned with the source, as was constrained by *Inan et al.* [2004]. We do not need this assumption since our system of equations is complete, allowing us to determine the source location uniquely using measurements from the four spacecraft. The direction of the source movement is also uniquely determined from the solution of the set of equations described in the previous Chapter.

Figure 3.4c consists of 4 spectrograms each of 4 seconds duration, from the time highlighted in Figure 3.2 for Case 2, at 01:35:25 UT. Figure 3.2c shows data observed after the geomagnetic equator crossing during the pass, illustrating the rising tone emissions. Once again, upper-band chorus activity is observed on all four spacecraft SC1, SC2, SC3 and SC4 but with only some elements being observed in multiple spacecraft, consistent with the bubbling source concept of Figure 2.5. The white circles once again are used to indicate the time duration and frequency span of the particular discrete chorus element studied in this work. The spacecraft positions are shown in Figure 3.4b, where the coordinates x , y and z are geomagnetic, i.e., the magnetic equatorial plane corresponds to $z = 0$ while the center of the Earth is specified by $x = 0$ and $y = 0$. Note that the z -axis is not orthogonal to the x -axis, but that it represents the distance along the field line which crosses the geomagnetic equator at the geomagnetic coordinates specified by given values of x and y . Figure 3.4a shows the location of the spacecraft in the frame of reference of the geomagnetic field, using the L parameter and the geomagnetic latitude λ_m as a coordinate system.

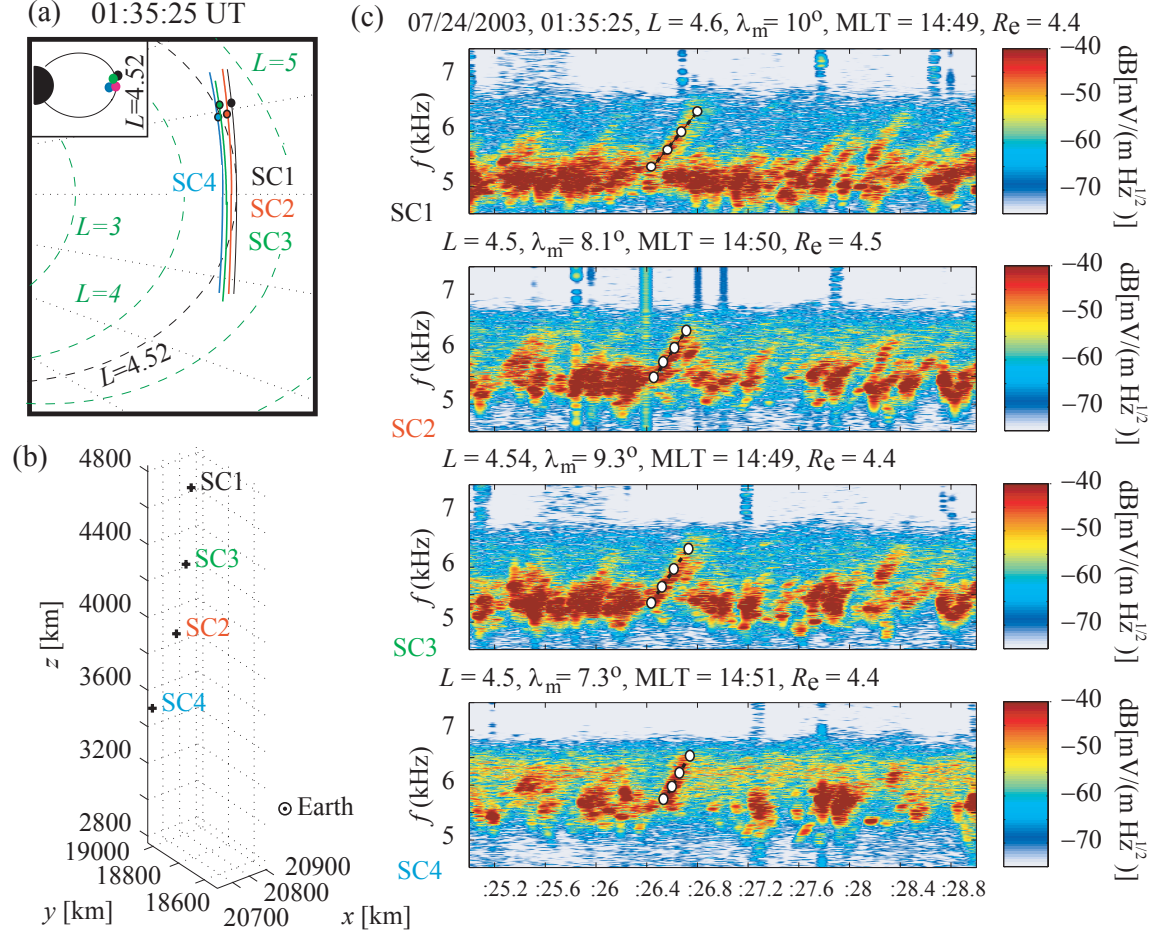


Figure 3.4: (a) Spacecraft location along the orbit for July 24, 2003. Indicated are the lines of constant L , and geomagnetic latitude λ_m . The spacecraft locations along their orbits when the observation was performed are illustrated by the colored dots. (b) Relative positions of the spacecraft with respect to each other in space. The system of coordinates in this panel is defined in Chapter 2. (c) 4 s spectrograms of electric field amplitude as observed by the 4 Cluster spacecraft, starting at 01:35:25 UT. The color scale indicates the magnitude of the electric field in dB with respect to $1 \text{ mV}/(\text{m}\sqrt{\text{Hz}})$. The y -axis indicates frequency, and the x -axis time in UT. Highlighted is the chorus riser element studied in Case 2.

As in Case 1, individual distinct chorus elements, i.e., those with similar frequency and time sequencing on different spacecraft, can be assumed to be emanating from the same source. The single element identified is divided into four points regularly spaced in time and frequency along the element and for each point the time and frequency differences between the four spacecraft are measured. The difference in slope between similar elements is also evident in Figure 3.4c, as the result of whistler mode propagation in the magnetosphere, which introduces dispersion in time, originating from the dependence of group velocity for whistler-mode propagation with frequency and the wave-normal angle ψ . The general appearance of the wideband spectra for this case consists of a multiplicity of chorus emissions generally observed typically only on one of the four spacecraft, mixed in with some elements observed on some of the spacecraft but not on all of them. The element marked in Figure 3.4 is one such particular element that was recognized to be common on all four spacecraft. Note, once again, that the fact that many elements are only observed on one spacecraft, and some on more than one and even fewer on all four is consistent with the general picture of distributed multiple active chorus sources, emitting waves in a range of directions, as described in Figure 2.5.

As pointed out in the previous paragraph, the important feature is the fact that some of the elements are observed in some of the spacecraft, but not in others. In some cases part of the chorus element is observed on one of the spacecraft while the entire element is observed in another. This type of distribution of chorus elements appears to be a common feature of multipoint observations of chorus. Chorus waves emanating from different sources sometimes reach different spacecraft, and sometimes reach all four of them. In such a situation, it can be more difficult to identify similar elements observed on different spacecraft. Nevertheless, simple visual inspection indicates that chorus emissions often have a very unique frequency-time structure, and that this structure, even when shifted in frequency and dispersed (e.g., slight changes in slope), still maintains its distinct frequency-time shape from one spacecraft to another. Visual inspection of 4-second long spectrogram sections like the ones shown in Figures 3.3 and 3.4 are used to measure the frequency-time characteristic of the single elements highlighted in Figure 3.2, which are later used in equations (2.9) and (2.12)

to estimate the variation of differential Doppler shift and time delay respectively as a function of time during the pass.

3.2 Source Location and Velocity for July 24, 2003

The determination of the source location and the direction of its motion follows directly from the calculations described in Chapter 2, by solving the system of equations described by (2.8), (2.9), (2.12), (2.17) and (2.18) using the measured values of the differential time delays and Doppler shifts (over a range of frequencies) as inputs. This solution is dominated by the time sequence of arrival of the chorus wave packet to the different spacecraft and the geometry of the problem, being the configuration in space of the four Cluster spacecraft approximately along a line in the z direction (See Figures 3.3b and 3.4b). This set of equations is highly non linear in terms of the wave normal angle ψ , and is over determined, therefore possibly leading to different solutions depending on the initial values used. The method used to solve this block of equations is the minimization method [Marquardt, 1963]. It consists of defining a square error function $g(\mathbf{x})$ as:

$$g(\mathbf{x}) = \sum_{\chi=1}^{25} \beta_{\chi} [Q_{\chi}(\mathbf{x}) - R_{\chi}(\mathbf{x})]^2 \quad (3.1)$$

where the 25 different Q_{χ} and R_{χ} are functions defined as each side of the equality of equations (2.8), (2.9), (2.12), (2.17) and (2.18). The argument of these functions is the vector $\mathbf{x} \in \mathbb{R}^{15}$ that represents the set of 15 unknowns specified in Chapter 2, \mathbf{x}_g being their respective estimated values. As an example, equation (2.8) can be used with spacecraft SC1 and SC4, yielding:

$$Q_{\chi}(\mathbf{x}) = v_S \quad R_{\chi}(\mathbf{x}) = \frac{c\Delta\omega_{1,4}}{\omega\mu_1(\mathbf{x})\cos(\psi_1) - \omega\mu_4\cos(\psi_4)} \quad (3.2)$$

where $\mu_1(\mathbf{x})$ and $\mu_4(\mathbf{x})$ must be replaced by (2.10), with $i = 1$ and 4 respectively. For this approach to work well, each term of the sum in (3.1) must be weighted with a factor β_{χ} , in order not to render any variable more significant than any other in the solution. The β_{χ} values are chosen by trial and error based on the behavior

of functions Q_χ and R_χ . They are chosen as the inverse of the estimated values of R_χ for each unknown vector (called \mathbf{x}_g) raised to the second power, i.e., as $\beta_\chi = [R_\chi(\mathbf{x}_g)]^{-2}$. This choice of the β_χ values using an exponent of 2 provides a means to normalize each error term in the sum (3.1) to avoid numerical errors due to the differences of magnitudes of the values of each $R_\chi(\mathbf{x}_g)$. The trial and error nature of this method comes from the proper selection of the \mathbf{x}_g , the most complicated task in the calculation, and one that is aided by the knowledge of the physics of the problem in hand. A proper selection of \mathbf{x}_g leads to convergence to a solution of the system of equations that lies within the error margins of the measurables. A wrong set of values for \mathbf{x}_g can lead to a set of solutions which provide a minimum in the solution space, but which does not satisfy the system of equations within the limits of the tolerance on the measurables, thus not constituting a real solution. The values of \mathbf{x}_g used for Cases 1 and 2 are shown in Tables 3.1 and 3.2, corresponding to each of the unknowns.

Once the \mathbf{x}_g values are determined, the system of equations can then be solved using different algorithms, the ones used for this case being the quasi-Newton, [Acton, 1990, ch. 14; Moré and Cosnard, 1979] and the Levenberg-Marquardt [Levenberg, 1944; Marquardt, 1963] methods, the latter being the more efficient method for the case in hand.

The present method of solution relies on the measurement of the frequency and time difference as well as the frequency-time slope of the individual chorus elements observed on the four spacecraft. The manner in which this measurement is used in our determination of the source properties is illustrated in Figures 3.3c and 3.4c. The chorus emission is assumed to be generated at the source with a frequency that increases with time. The source of the chorus subsequently moves toward, or away from, the spacecraft (depending on the sign of the Doppler frequency shift) resulting in the frequency-time slopes that are observed on SC1 to SC4. The solution of the system of equations reveals the original frequency range and frequency-time shape of the emission at the source, uniquely determined by the unknowns f (or ω) and the propagation times d_i/v_{gi} , with $i = 1, \dots, 4$. This process also has the desired outcome of identifying the specific location at which each frequency is emitted and

	\mathbf{x}_{g1}	\mathbf{x}_{g2}	\mathbf{x}_{g3}	\mathbf{x}_{g4}
$f[\text{Hz}]$	5500	5600	5700	5800
v_S/c	0.001	0.001	0.001	0.001
$d_1[\text{km}]$	4600	3800	3500	2500
$d_2[\text{km}]$	3600	2900	2200	1500
$d_3[\text{km}]$	4100	3500	2800	2000
$d_4[\text{km}]$	2900	2300	1700	1000
$\psi_1[^\circ]$	4.2	5	6	15
$\psi_2[^\circ]$	10	10	12	15
$\psi_3[^\circ]$	6.4	7.1	8	17
$\psi_4[^\circ]$	0	0	0	0
$\zeta[^\circ]$	90	90	90	90
$\sigma[^\circ]$	90	90	90	90
$\rho[^\circ]$	90	90	90	90
$\delta[^\circ]$	90	90	90	90
$S_Z[\text{km}]$	-4700	-4000	-3500	-2500

Table 3.1: Values \mathbf{x}_g used to solve the system of equations described by (2.8), (2.9), (2.12), (2.17) and (2.18), for Case 1

	\mathbf{x}_{g1}	\mathbf{x}_{g2}	\mathbf{x}_{g3}	\mathbf{x}_{g4}
$f[\text{Hz}]$	4300	4600	5000	5200
v_S/c	-0.02	-0.033	-0.02	-0.02
$d_1[\text{km}]$	6800	6300	5400	5200
$d_2[\text{km}]$	7800	7200	6400	6100
$d_3[\text{km}]$	7200	6700	5900	5600
$d_4[\text{km}]$	8200	7700	7000	6500
$\psi_1[^\circ]$	135	138	138	135
$\psi_2[^\circ]$	169	160	152	146
$\psi_3[^\circ]$	139	140	139	140
$\psi_4[^\circ]$	180	180	180	180
$\zeta[^\circ]$	90	90	90	90
$\sigma[^\circ]$	90	90	90	90
$\rho[^\circ]$	90	90	90	90
$\delta[^\circ]$	90	90	90	90
$S_Z[\text{km}]$	11000	10500	9500	8000

Table 3.2: Values \mathbf{x}_g used to solve the system of equations described by (2.8), (2.9), (2.12), (2.17) and (2.18), for Case 2

the direction and the magnitude of the velocity of the source.

3.2.1 Source Location Results for Case 1

For Case 1, displayed in Figure 3.3, the source location results are shown in Figure 3.5. The four panels presented herein correspond to four different values of frequency f , calculated from the system of equations presented in Chapter 2. These four points in frequency correspond to four different parts of the chorus element highlighted with white circles in Figure 3.3. The use of four frequency-time points in the chorus element allows accurate definition of frequency-time shape of the elements and allows to resolve the frequency dependence of source location and velocity. The selection of the points is done so as to have uniformly distributed frequency-time pairs as explained in Section 3.1.2. The resulting measurement error depends on the frequency (time) spread of the chorus element at each time (frequency). Each of the four measurements of this element, as observed by spacecraft SC1 to SC4, represent a corresponding value of time and frequency. All of the six combinations of pairs from these four values of f_i and t_i , for each spacecraft SC i , are fed into equations (2.9) and (2.12) to calculate the values of $\Delta\omega_{i,j} = \omega_i - \omega_j$ and $\Delta t_{i,j} = t_i - t_j$, the index i and j representing the corresponding number of spacecraft SC i and SC j . As explained at the end of Chapter 2, the values of the plasma frequency ω_p and the electron gyrofrequency ω_c are known within a range of $|\omega_c - \omega_{co}| / \omega_{co} < 0.01$ and $|\omega_c - \omega_{po}| / \omega_{po} < 0.1$, where $\omega_{po} = 54.5$ kHz and $\omega_{co} = 8$ kHz for Case 1, as highlighted in Figure 3.1. The quantities $\Delta_{i,j}$ and $\Delta t_{i,j}$ also have their respective uncertainties and should also be considered as unknowns with the restrictions $|\Delta t_{i,j} - \Delta t_{i,j,o}| < 0.01$ sec and $|\Delta\omega_{i,j} - \Delta\omega_{i,j,o}| / 2\pi < 10$ Hz (The subindex ‘o’ refers to the observed values of ω_c , ω_p , $\Delta t_{i,j}$ or $\Delta\omega_{i,j}$). These tolerance values are used for the four measurables, ω_c , ω_p , $\Delta\omega_{i,j}$ and $\Delta t_{i,j}$ in the four cases studied in this work. The results in Figure 3.5 show the values of the location of the source as given uniquely in the 3D space by S_Z , d_1 to d_4 , and the set of angles ζ , σ , ρ , δ (See Figure 2.6). The error bars in the z direction are obtained from equation (2.17), representing the range of values acquired by S_Z for different values of the observables in the solution space, within the restrictions mentioned earlier.

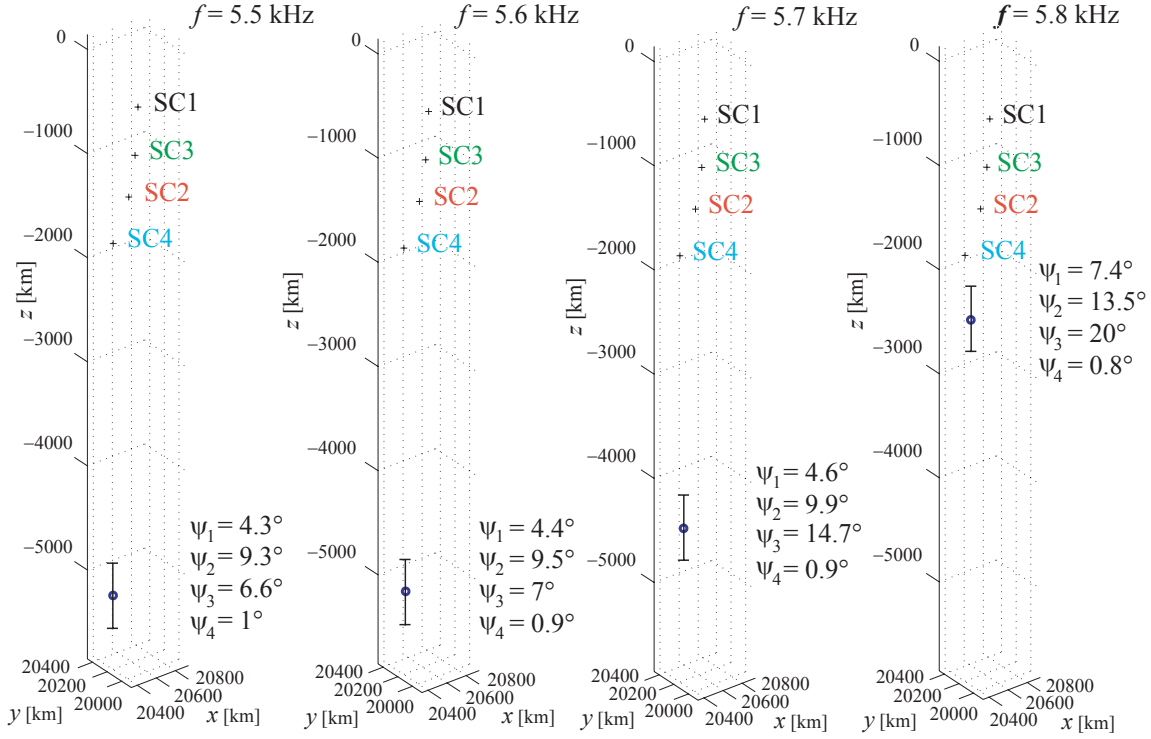


Figure 3.5: Source location results on July 24, 2003, 01:14:38 UT, for four different calculated frequencies, each one corresponding to one of those shown in each of the four panels. The position of the spacecraft is indicated as well as the source. The system of coordinates in this panel is defined in Chapter 2. For each result in source location the corresponding values of wave normal angle are specified (ψ_i , for $i = 1, \dots, 4$).

The system of equations is expected to have several solutions, and it is found that such is indeed the case, but the solutions found must also have physical significance, and among those that are found to be physically significant, the one with a minimum value of $g(\mathbf{x})$ is the one that is adopted as the solution. Nevertheless it should be mentioned that the difference of $g(\mathbf{x})$ for any set of solutions \mathbf{x} found to fulfill the restrictions on the measurables is not significant.

The results obtained for source location and velocity using equations (2.8), (2.9), (2.12), (2.17) and (2.18) by means of a simple test. Using the results for the 15 unknowns of the set of equations presented in Chapter 2, the values of frequency and time observed at each spacecraft SC i can be calculated and compared to the ones

originally observed, i.e., the measurables, represented by the white circles in Figures 3.3 and 3.4. The general procedure to check the results obtained via the solution of equations (2.8), (2.9), (2.12), (2.17) and (2.18), is described by the following two steps:

1. The values of observed frequency for each point along each element onboard SC*i* can be obtained from equation (2.9), for each of the four points picked for the chorus element shown in Figure 3.3. This calculation is performed using the obtained values of ω , ψ_i , v_S and the corresponding μ_i calculated using (2.10).
2. The procedure to obtain the values of observed time requires some additional elaboration. The values of observed time obtained from the UT scale in Figures 3.3 and 3.4 for each spacecraft SC*i* ($i = 1, \dots, 4$) $t'_{UT\,i}$ are given by $t'_{UT\,i} = t_0 + d_i/v_{gi}$, expression that is substituted in (2.12) to obtain the time of arrival differences between spacecraft $\Delta t_{i,j} = t'_{UT\,i} - t'_{UT\,j}$. A reference time value t_0 is introduced, which unfortunately represents an extra unknown that cannot be obtained from the system of equations given by (2.8), (2.9), (2.12), (2.17) and (2.18). Therefore one of the spacecraft is used as a reference in time (denoted here as SC*r*), assuming that the observed value of $t'_{UT\,r}$ coincides with the calculated one. After this procedure the rest of the values of $t'_{UT\,i}$, for $i \neq r$ can be obtained using the estimated value of d_r and v_{gr} from (2.13) or (2.14) to obtain a value of t_0 from $t_0 = t'_{UT\,r} - d_r/v_{gr}$. The rest of the values of $t'_{UT\,i}$ are then compared with t_0 , using $t'_{UT\,i} = t_0 + d_i/v_{gi}$ from the obtained values of d_i and the corresponding v_{gi} calculated using (2.13) or (2.14). In the verification of Cases 1 to 4 discussed in this dissertation, SC1 is taken as a reference, i.e., $r = 1$.

The verified values of observed time $t'_{UT\,i}$ and frequency ω'_i pairs for Case 1 are shown in Figure 3.6 as green circles. They are superimposed to the originally observed white circles already displayed in Figure 3.3. The difference between the observed and recalculated values of $t'_{UT\,i}$ and ω'_i lies within the error range that was adopted as a restriction on these measurables as was explained at the beginning of this subsection. The agreement lies within the expected error adopted in the calculations and shows

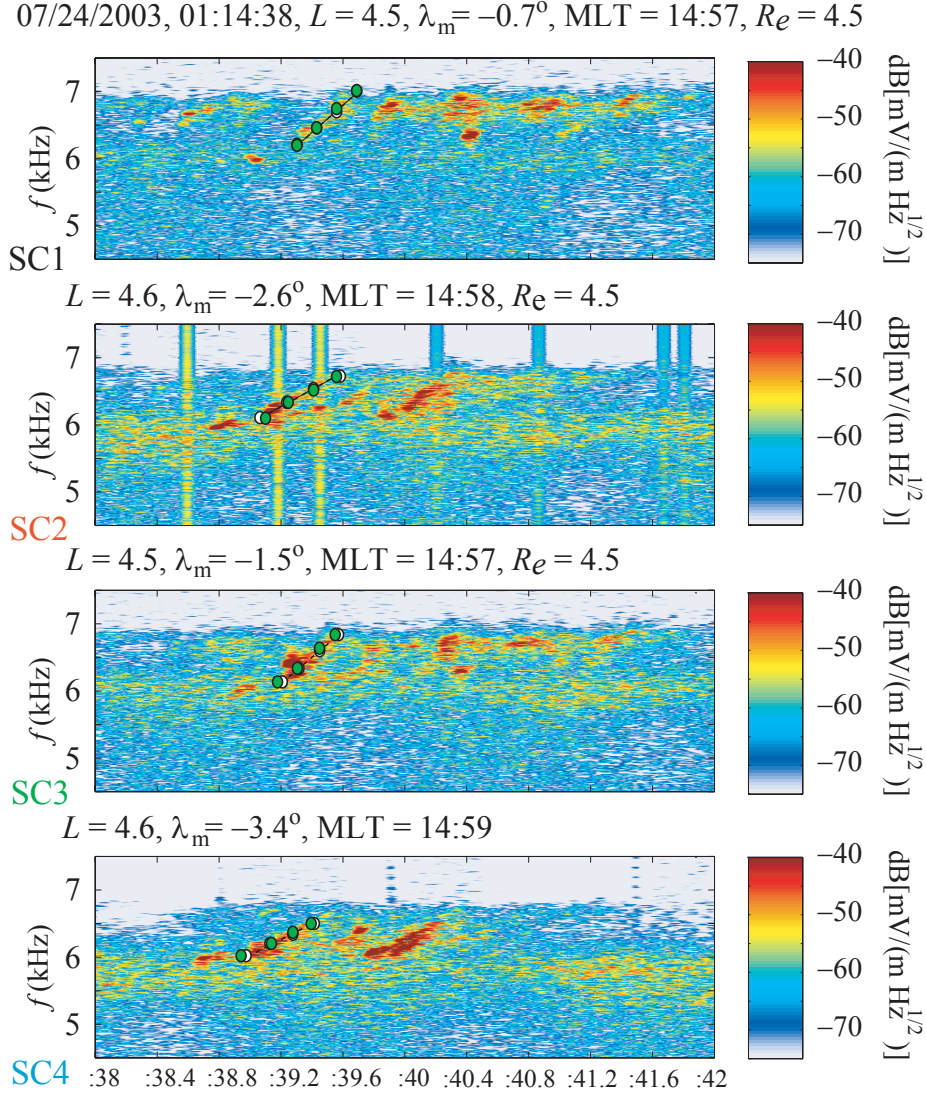


Figure 3.6: Four second spectrograms of electric field data observed by the four Cluster spacecraft, starting at 01:14:38 UT. The color scale is related to the magnitude of the electric field in dB with respect to $1 \text{ mV}/(\text{m}\sqrt{\text{Hz}})$. The vertical axis indicates frequency, while the horizontal axis indicates time in UT. Highlighted (with white circles across its frame) is the chorus element studied in Case 1. Overimposed (with green circles) are the four recalculated values of observed ω'_i and t'_i at each spacecraft $\text{SC}i$ ($i = 1, \dots, 4$)

that the method is self consistent. The same verification is performed for Cases 2, 3 and 4 shown in what follows of the dissertation, even though a similar figure as 3.6 is not included for those Cases.

3.2.2 Source Location Results for Case 2

The chorus element studied in Case 2 and displayed in Figure 3.4 is found to have a source as shown in Figure 3.7. As in Case 1, the four panels correspond to four different values of frequency f calculated from the system of equations presented in Chapter 2. This result also suggests a field aligned moving source, emitting coherent wave packets at different frequencies at different locations along the field line. These four values of f were calculated using the same method of dividing the chorus element into four $f - t$ pairs, selected as explained in section 3.1.2. The results of Figure 3.7 display the values of the location of the source as given uniquely in the 3D space by S_Z , d_1 to d_4 , and the set of angles ζ , σ , ρ , δ (See Figure 2.6). As in Case 1, the error bars in the z direction are obtained from equation (2.17), being the deviation of S_Z for different values of observables within the solution space, within the restrictions mentioned earlier. In this case, the system of equations is also expected to have several solutions as before. The solutions found must have physical significance and within the ones that do, the one with a minimum value of $g(\mathbf{x})$ is adopted. As is shown in Chapter 4, the risers observed in Figure 3.4 are generated away from the equator, while the sources of the emissions move rapidly toward it. The extent of the source motion along the field line is larger for Case 2, being ~ 3700 km, while the frequency range spanned by the risers in Figure 3.4 is more than that for the risers in Figure 3.3. The source in this case is also moving toward the spacecraft, i.e., in the direction of propagation of the observed chorus wave packets.

3.2.3 Raytracing Results

Results shown in Figures 3.5 and 3.7 have been obtained using the formulation and the method of calculation presented in Chapter 2. These calculations are performed based on the fact that rays propagate roughly along the field line, and that the

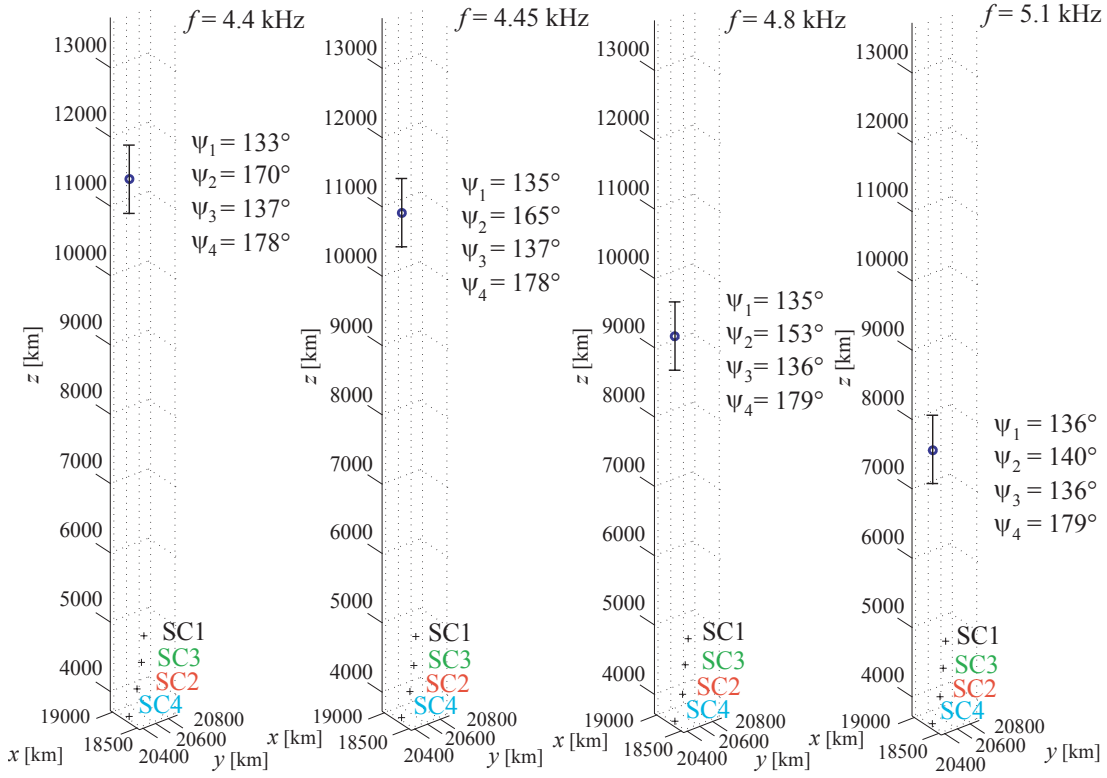


Figure 3.7: Source location results for July 24, 2003, 01:35:25 UT, for four different calculated frequencies, each one corresponding to each of the four panels. Indicated is the position of the spacecraft as well as the source with their corresponding error bars along the z -axis. The system of coordinates in this panel is defined in Chapter 2. For each result in source location is specified the corresponding values of wave normal angle (ψ_i , for $i=1, \dots, 4$).

wave normal angles do not change much along short trajectories. Nevertheless, the source-to-spacecraft distances obtained are found to be large enough to raise questions about the validity of this assumption. To assess the possible effects of wave normal angle variation (along the path) on our results, the calculation is repeated using 2D raytracing in an inhomogeneous magnetospheric model to estimate the values of the wave normal angles and to correct the values of the source location accordingly. The raytracing method consists of the use of the plasma density profile obtained from the Whisper instrument as an input to the Stanford 2D raytracing program described in *Inan and Bell* [1977]. Relaxing the assumptions that the ray paths are straight lines in the field aligned system of coordinates, raytracing is used based on the Haselgrove equations [*Haselgrove*, 1954]. The following expressions are used to calculate the ray path coordinates $\mathbf{r} = [r \ \varphi]$ in space. The coordinate r indicates the radial distance from the origin of the coordinate system, φ is the zenith angle, the angle between the vertical z -axis and the \mathbf{r} vector. A 3D version of the vector \mathbf{r} would also include the azimuth angle ϕ , the angle between the positive x -axis and the \mathbf{r} vector projected onto the $x-y$ plane that has a one-to-one relation with the magnetic local time MLT. Nevertheless for in our 2D calculations, ϕ is fixed (as required for 2D tracing), and therefore not used. As we already know, the orientation of \mathbf{n} is the same as \mathbf{k} , $\mathbf{n} = [n_r \ n_\varphi]$ and $|\mathbf{n}| = \mu$. The raytracing code is utilized for a cold, magnetized collisionless plasma and uses the Haselgrove differential equations for the 2D case to find \mathbf{r} and \mathbf{n} :

$$\begin{aligned}\frac{dr}{dt} &= \frac{1}{\mu^2} \left(n_r - \mu \frac{\partial \mu}{\partial n_r} \right) \\ \frac{d\varphi}{dt} &= \frac{1}{r\mu^2} \left(n_\varphi - \mu \frac{\partial \mu}{\partial n_\varphi} \right)\end{aligned}\tag{3.3}$$

$$\begin{aligned}\frac{dn_r}{dt} &= \frac{1}{\mu} \frac{\partial \mu}{\partial r} + \frac{d\varphi}{dt} \\ \frac{dn_\varphi}{dt} &= \frac{1}{r} \left(\frac{1}{\mu} \frac{\partial \mu}{\partial \varphi} - n_\varphi \frac{dr}{dt} \right)\end{aligned}\tag{3.4}$$

The value of μ is obtained from equation (1.7) (using the minus sign for whistler mode propagation), while its derivatives are given as:

$$\begin{aligned} \frac{\partial \mu}{\partial n_\iota} &= \frac{\partial \mu}{\partial \psi} \frac{\partial \psi}{\partial n_\iota} = \frac{\partial \mu}{\partial \psi} \left[\frac{n_\iota B_0 \cos(\psi) - \mu B_0}{\mu^2 B_0 \sin(\psi)} \right] \\ \frac{\partial \mu}{\partial \iota} &= \frac{\partial \mu}{\partial \psi} \frac{\partial \psi}{\partial \iota} + \sum_u \frac{\partial \mu}{\partial \omega_{cu}} \frac{\partial \omega_{cu}}{\partial \iota} + \sum_u \frac{\partial \mu}{\partial \omega_{pu}} \frac{\partial \omega_{pu}}{\partial \iota} \end{aligned} \quad (3.5)$$

for $\iota = r, \varphi$ and for each species u .

The magnitude of the derivatives $\partial \psi / \partial \iota$ and $\partial \omega_{cu} / \iota$ depend upon the adopted model of the Earth's magnetic field, which in our case is the centered dipole model. The quantity $\partial \omega_{pu} / \iota$ depends on the particle density model used; in our case, the r^{-4} model is used for densities outside the plasmasphere [Platino *et al.*, 2005], based on measurements with the Whisper instrument of the plasma frequency.

The waves are launched from the positions calculated for the model described above, using the value of frequency and wave normal angle obtained by the system of equations in Chapter 2. The resultant propagation times from the source to the spacecraft are compared to the measured values and an adjustment in the values of ψ_i for each spacecraft SC*i* is performed in order to fit the measured delays. Even though this process may result in slightly different values of f , ψ_i , d_i , S_Z and ζ , σ , ρ , δ than the ones calculated originally, the changes are not significant, as can be seen from Figure 3.8. Shown here is the evolution of ψ_i for chorus rays launched from the estimated source location toward the spacecraft SC*i*, in both Cases, 1 and 2 (Distances between spacecraft are exaggerated for clarity). The colored lines indicate the ray trajectories for different frequencies while the small black segments show the direction of the \mathbf{k} vector. Indicated in Figure 3.8 are the values of the wave normal angles at the source and at the spacecraft. In our two cases, we find that the ray paths calculated stay field aligned, requiring relatively small correction ($< 8\%$) to the results previously obtained without raytracing. The values of the source location and velocity, displayed in Figures 3.5, 3.7 and 3.9 are all verified by taking into account the effect of ray propagation as described in this paragraph and shown in Figure 3.8.

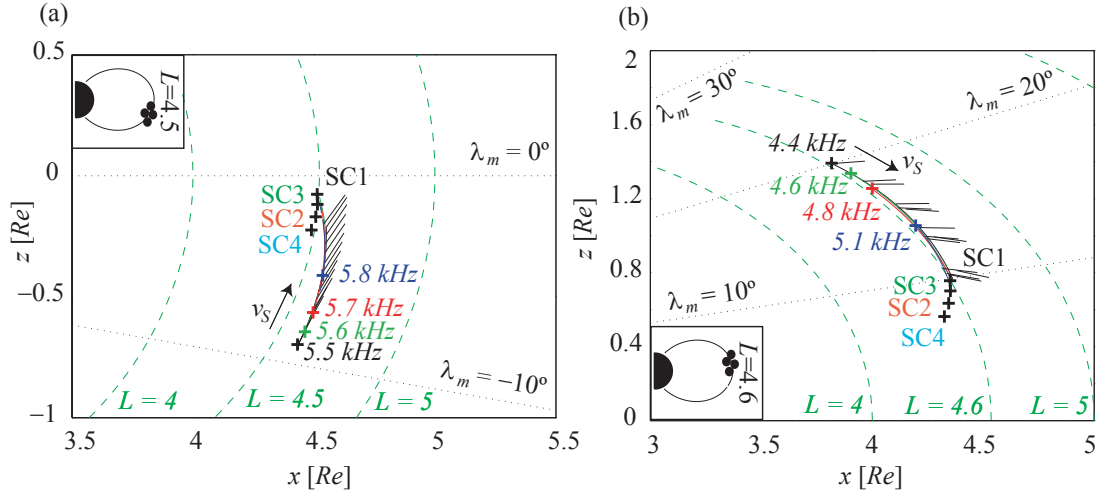


Figure 3.8: Raytracing results for July 24, 2003, when rays are launched from the source locations calculated for each of the four frequencies obtained in this case. The full lines correspond to the ray path for each frequency, while the small black segments placed periodically along the ray path represent the direction of the wave vector, \mathbf{k} . Displayed are the lines of constant L and geomagnetic latitude λ_m .

It should be noticed in Figure 3.8 that ψ can vary along the trajectory from the source to the spacecraft. This feature is not contemplated in the calculations performed in Chapter 2, and is one of the reasons why the correction using raytracing may be necessary.

3.2.4 Source Velocity Results

The results of calculated source velocities are shown in Figure 3.9a and 3.9b. Each panel shows the source velocity for the values of frequency obtained from the calculations described on Figures 3.5 and 3.7. The error bars on the two plots are calculated considering the sensitivity of the solution to changes of the values of the input parameters of ω_p and ω_c . Superimposed on the source velocity plot are the corresponding values of the parallel velocity of resonant energetic electrons for $\psi \simeq 0^\circ$, as calculated from the expression [Helliwell, 1967]:

$$-v_{\parallel} = \frac{\omega_c - \omega}{k} \simeq \frac{(\omega_c - \omega)^{3/2}}{\omega_p \sqrt{\omega}} c \quad (3.6)$$

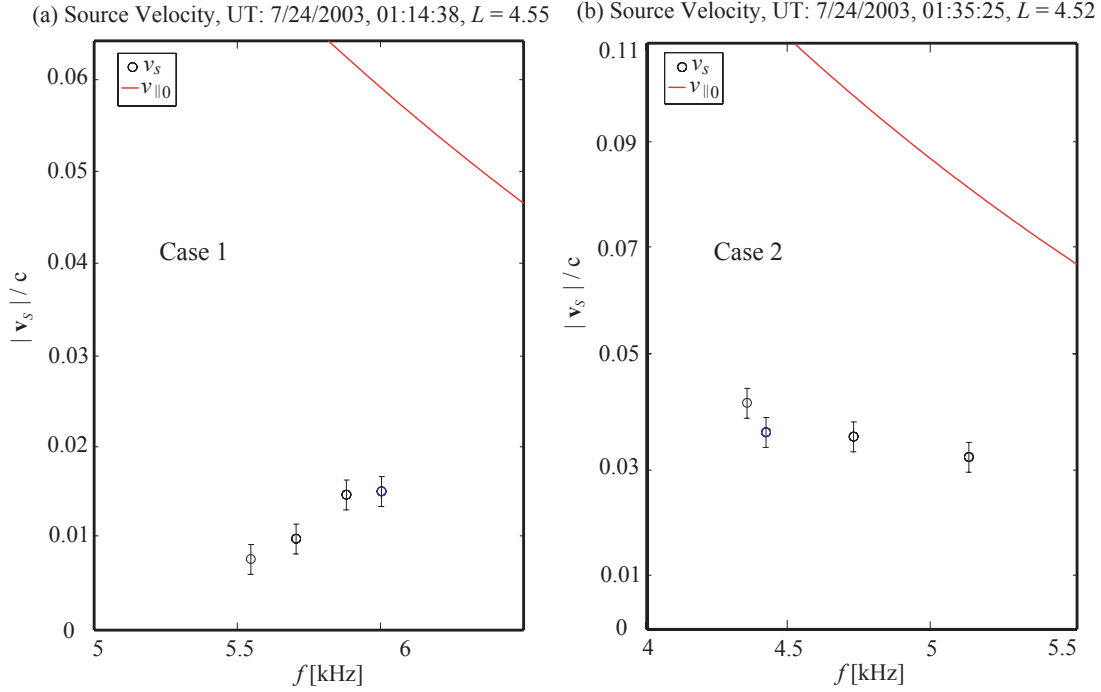


Figure 3.9: Results of the calculations of source velocity as a function of frequency on July 24, 2003. (a) Case 1 at 01:14:38 UT; (b) Case 2 at 01:35:25 UT. The obtained values of v_s display their corresponding error bars. The approximate parallel velocity of resonant energetic electrons, v_{\parallel} , is shown in red in both plots. In both cases the source is moving toward the spacecraft. The calculated values of group velocity v_g are not shown because their magnitudes are larger than the maximum scale in plots (a) and (b)

The source velocities calculated for the two cases differ by a factor of ~ 3 , being higher for the risers observed after the equatorial crossing. In Case 1 the source velocity increases with frequency, while in the second case it decreases.

The fact that the deduced velocities of chorus source are of the same order of magnitude as the parallel resonant velocity and the wave group velocity is consistent with the heuristic discussion of source motion in [Helliwell, 1967] based solely on energy considerations. In the next two Chapters we provide a quantitative interpretation of chorus source motion, showing that such motion is a necessary consequence of other known properties of chorus emissions, namely growth rate, bunching time and saturation.

Chapter 4

A Physical Interpretation of Moving Sources of Chorus

‘Beauty will be convulsive or will not be at all.’¹

In this Chapter, we discuss the cyclotron resonance process of whistler wave amplification and illustrate that the field-aligned motion of the sources of discrete chorus emissions is a natural result of the known properties of discrete chorus emissions, such as the rapid temporal growth, saturation of growth and the frequency-time variations. We also demonstrate by considering several example cases, that the direction and speed of the source motion is largely controlled by the temporal growth rate. The objective of this chapter is thus to present a simple phenomenological model which predicts source motion along \mathbf{B}_0 , in order to establish the plausibility of such moving sources. The phenomenological model presented in this thesis draws upon cyclotron resonance growth driven by anisotropy of the energetic particle distribution, as the general mechanism of generation of ELF/VLF emissions. In this context, we note that the physical mechanisms that lend to the discrete and coherent forms of chorus and the observed high growth rates is not yet understood, and that we do not attempt to explain these features. Rather, we simply set out to present a simple interpretation to show how motion of sources of chorus emissions can come about as a result of other

¹André Breton, *Nadja*, first published as a novel in 1928

known properties of chorus. In this context, the primary starting assumptions made are (i) that chorus emissions exhibit rapid temporal growth and saturation, and (ii) the frequency-time shape of chorus is inherent to the emission mechanism. In other words, the phenomenological model presented here does not in any way attempt to explain why chorus is emitted as a rising (or falling) emission. Rather, we take it as a matter of fact that chorus is emitted in this form, and show that this fact, and the known rapid temporal growth and saturation naturally lead to rapid motion of sources of chorus.

4.1 Interpretation of Chorus Source Motion

Some of the basic features of the phenomenological model used here are described in *Helliwell* [1967]. In this model, the perpendicular velocity vectors \mathbf{v}_\perp of energetic electrons drifting along \mathbf{B}_0 are bunched in gyrophase by interaction with a triggering (i.e., externally injected or locally generated stimulant) whistler mode wave. This bunching results in a total perpendicular (to \mathbf{B}_0) current \mathbf{J}_\perp that radiates at the local electron gyrofrequency in the field-aligned drift frame of the resonant electrons. The motion of the particles in the direction opposite to the wave propagation produces a Doppler shift in the frequency of the radiated wave energy, which is why chorus waves are observed in the whistler mode at frequencies below ω_c . In the *Helliwell* [1967] model, the location of the phase bunching interaction in regions of different \mathbf{B}_0 (and corresponding ω_c) and the drifting motion of the source lead to the frequency-time shapes (i.e., risers and fallers) characteristic of chorus emissions. According to this model, the wave energy that is convected away from the interaction region as shown in Figure 1.6a at the group velocity and must be supplied by the incoming electrons. If the input power from the streaming electrons is not exactly equal to the output wave power for a fixed position, then the interaction region drifts either downstream or upstream at a velocity such that input power equals output power. With these arguments, *Helliwell* [1967] heuristically predicted that the source velocity should lie in the range between the group velocity of the wave in one direction and the parallel resonant velocity of the bunching particles in the other direction.

While some of the phenomenological aspects of the *Helliwell* [1967] model are also applicable in our case, the underlying purpose in our work is the quantitative interpretation of the observed motions of chorus sources. For this purpose, we take the frequency-time shape to be an inherent feature of the emission process, and take the rapid temporal growth and saturation properties of chorus emissions as observationally established facts. We then show that these assumptions alone lead to the rapid motions of chorus sources. Even though the *Helliwell* [1967] study serves as a starting point for our interpretation because of its prediction of source motion based on heuristic arguments, none of the calculation in this Chapter is based on it. The work of *Helliwell* [1967] has been visionary and has identified the physics involved in the cyclotron resonance mechanism. However, this model is based on considerations of the individual resonant particles and does not account for the wave growth driven by the anisotropy of the distribution functions in velocity space. These and other shortcomings of *Helliwell* [1967] were improved upon later studies (e.g., *Bell* [1984]; *Matsumoto and Kimura* [1971]; *Nunn* [1986] and *Trakhtengerts et al.* [2003]).

In the present work, the source location is defined to be the average between the two points within the interaction region where the radiating current \mathbf{J}_\perp is 3dB below its first local maximum. For the purpose of our work, the interaction region is defined in the same way as *Helliwell* [1967], i.e., it is the region along the z -axis where significant phase bunching occurs. The parameter z_{int} , the coordinate designating the point along the field line at which the phase bunching process starts, is one of the limits of this region and is the one used in our calculations.

Our physical interpretation of moving sources of chorus is illustrated in Figure 4.1. On a given L shell there exists a local minimum of the Earth's magnetic field, such as that which exists near the geomagnetic equator. The minimum of \mathbf{B}_0 provides both the concentration of trapped energetic electrons as the source of free energy needed for amplification by cyclotron resonance, and also maximizes the interaction lengths for individual resonant electrons [e.g., *Inan et al.*, 1983]. As explained below, the source of new radiation is the current produced by gyroresonant electrons and we define its location in space to be S_Z , the coordinate along z where the maximum radiating current \mathbf{J}_\perp occurs at a given frequency ω . The energetic electrons move along the

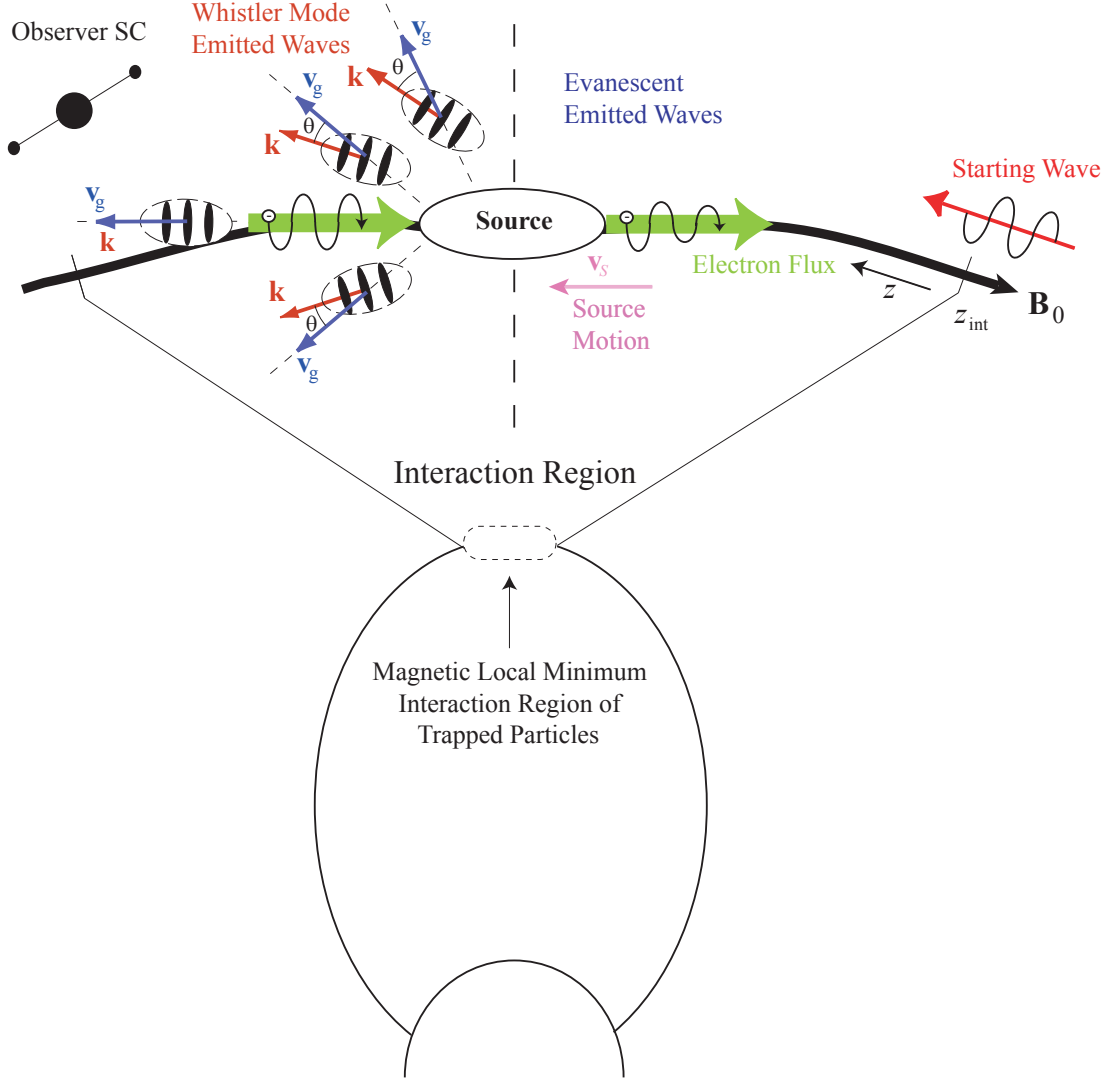


Figure 4.1: General picture of the physical interpretation of chorus based on the cyclotron resonance model. Interaction occurs around the geomagnetic equator, where B_0 has a minimum along the L shell. The green arrows represent the particle flux along the magnetic field lines. Whistler mode wave packets are emitted from the source in the counter streaming direction, each wave packet identified with its corresponding k and v_g . In the interaction region, a field aligned system of coordinates is defined with the z -axis defined along B_0 . The position z_{int} indicates the point along z where phase bunching starts when a triggering pulse enters the region.

field lines, and when a triggering pulse enters the region, it initiates the amplification process. Amplification may also be initiated by noise fluctuations already present in the region, rather than an external triggering signal. Amplified waves are emitted at a wide range of wave normal angles. The wave energy propagating in a direction which projection along the z -axis is counter streaming (i.e., direction along \mathbf{B}_0 that is opposite to the streaming motion of the particles) are electromagnetic whistler-mode waves, while in the streaming direction only evanescent waves exist. In the anisotropic magnetoplasma medium, wave energy at different wave normal angles propagates both along and at an angle to the ambient magnetic field. A spacecraft close enough to the source can observe the oblique propagating waves as well as the parallel propagating ones. The source location changes along the field line within this interaction region according to the mechanism we describe below. The field aligned system of coordinates used in Chapters 2 and 3 is also used in this Chapter.

4.2 Phase Bunching

An essential consequence of the cyclotron resonance interaction is the so-called phase bunching of the resonant electrons. This bunching is a process by which the velocities along the field line of gyro-resonant energetic electrons are modified in gyrophase [Bell, 1964b; Schmidt, 1966, pp. 244-245; Helliwell and Crystal, 1973] through interaction with a triggering wave of amplitude B_w , as illustrated in Figure 4.2 (Based on Figure 3 from Helliwell and Crystal [1973]). Figure 4.2a shows an initial state at $t = 0$ where a set of 12 test particles of identical energy and pitch angle gyrating around \mathbf{B}_0 with approximately the same gyroradius, move with the same velocity $v_{\parallel k}$ parallel to \mathbf{B}_0 . Perpendicular to \mathbf{B}_0 , the electron velocities are $\mathbf{v}_{\perp k}$ with the same magnitude but different azimuthal angles ($k = 1, \dots, 12$) (also called Larmor phase) with respect to the wave magnetic field B_w . Each vector $\mathbf{v}_{\perp k}$ is indicated with a different color and the tip of each vector, highlighted with a point of the same color, describes a helix as the particles move along z . The helical motion of each resonant electron constitutes a helical current (also called ‘elemental stream’ [Helliwell and Crystal, 1973]) that radiates a Doppler shifted wave in the z direction, but initially at a location $x \simeq 0$,

$y \simeq 0$, $z = z_1$, the vector sum of the $\mathbf{v}_{\perp k}$'s, labeled in Figure 4.2 $\mathbf{v}_{\perp}^{\text{res}}$, is zero. Therefore, at that location in space the total radiating current is zero. During the time interval $0 < t < t_1$ (Figure 4.2b), a whistler mode wave with magnetic field amplitude B_w perpendicular to z interacts with the 12 particles, which are affected by a bunching force parallel to z given by $\mathbf{F}_k = q_e(\mathbf{v}_{\perp k} \times \mathbf{B}_w)$, where q_e is the magnitude of the charge of the electron. By the time $t = t_1$ the particles have moved several wavelengths of the triggering wave along z , and at $x \simeq 0$, $y \simeq 0$, $z = z_2$, the perpendicular velocity vectors $\mathbf{v}_{\perp k}$'s have been modified in their azimuthal angles around \mathbf{B}_0 by the influence of the bunching force \mathbf{F}_k . The main function of the wave is to organize the relative gyrophases of each of the 12 streams so that their radiation becomes coherent, and so that after a given time has elapsed, the vector sum of all their velocities perpendicular to \mathbf{B}_0 is nonzero, producing a resulting finite perpendicular radiating current \mathbf{J}_{\perp} . Figure 4.2a corresponds to an initial uniform distribution of particles in gyrophase with a fixed number of particles that are exactly in gyroresonance at the start.

Once again considering only the resonant electron stream, the bunching period τ_B , which represents the time during which phase bunching occurs, can be estimated if the value of the triggering pulse amplitude B_w and the pitch angle of the resonant particles α are known [Bell, 1984]:

$$\tau_B = \frac{2\pi}{\sqrt{\frac{q_e}{m_e} B_w [\omega_c - \omega] \tan(\alpha)}} \quad (4.1)$$

where m_e is the mass of the electron. While Figure 4.2a illustrates the phase bunching only for the single group of resonant electrons, the resultant amplification (or damping) of the wave is determined by the total sum effects of the phase bunching of the larger group of energetic electrons, distributed in initial perpendicular and parallel velocities. In other words, electrons that have parallel velocities in the vicinity of the cyclotron resonant velocity as given by (1.8), and those having a wide range of pitch angles all contributed (at varying degrees) to the establishment of the perpendicular radiating current \mathbf{J}_{\perp} . The wave growth rate resulting from the phase bunching process as considered in this study, is thus determined by the velocity space gradients of the number density of energetic electrons moving with perpendicular velocities and

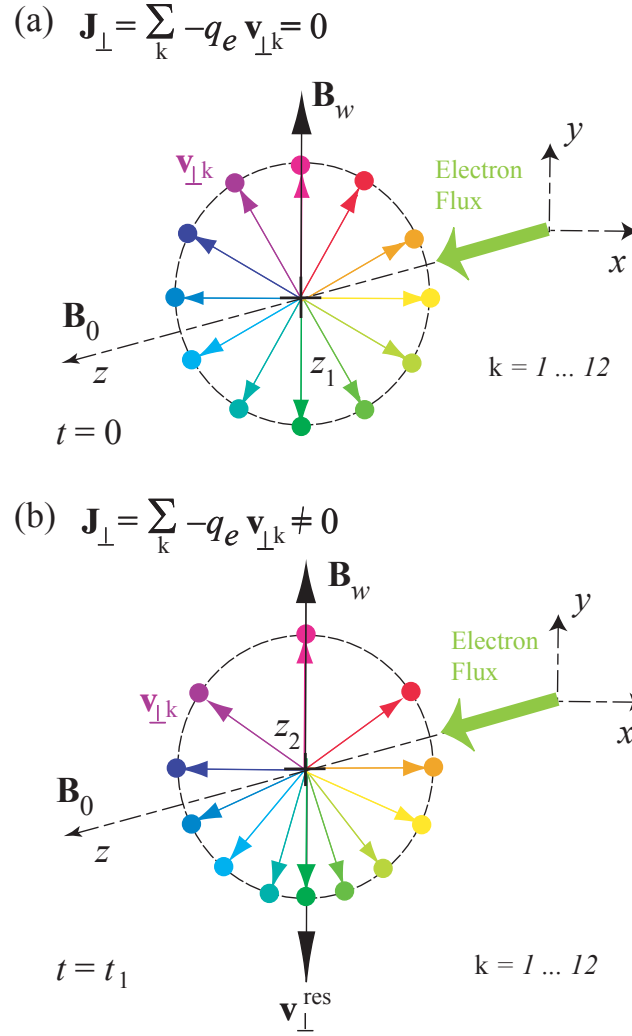


Figure 4.2: Phase bunching process, adapted from *Helliwell and Crystal* [1973] (a) A set of 12 particles are gyrating around \mathbf{B}_0 , moving along the z -axis before phase bunching starts. The vector sum of the perpendicular components of the velocities $\mathbf{v}_{\perp k}$ of each of the particles is 0. (b) After a time $t = t_1$, the vector sum of all the $\mathbf{v}_{\perp k}$ is finite, resulting in a radiating current \mathbf{J}_\perp

pitch angles as given by the velocity space distribution function $f(\mathbf{v}, \alpha, \lambda_m)$ [Matsumoto and Kimura, 1971]. In this context, the bunching time as given in (4.1) is to be viewed as an ‘average’ value representative of the time it takes for the overall current (produced by the totality of the electrons near resonance) to reach its peak value. In the following, we index our discussion on the initial bunching time $\tau_B/4$, with the understanding that this is an average value representative of all the energetic electrons which contribute to the radiating currents.

In this average sense, it is assumed τ_B is related to t_1 , i.e., the time at which \mathbf{J}_\perp is maximum to be $t_1 \simeq \tau_B/4$, similar to the value adopted in *Helliwell and Crystal* [1973]. Figure 4.3 shows a sketch of the magnitude of \mathbf{J}_\perp highlighted in solid colored lines at three different frequencies ω_1, ω_2 and ω_3 . An example of the general form of the curve of \mathbf{J}_\perp as a function of time can be found in Figure 4 of *Trakhtengerts et al.* [2003]. As is apparent from Figure 4.3, the radiating current $\mathbf{J}_{\perp\xi}$ at a given frequency ω_ξ ($\xi = 1, \dots, 3$) reaches a peak value at $\tau_B/4$ and then decreases in magnitude with time. The location along z at which phase bunching generates a maximum radiating current at a given frequency is defined here as the source location $S_{Z\xi}$. This process can be repeated for each frequency, along the chorus element so that every time $\mathbf{J}_{\perp\xi}$ reaches its peak, a new wave packet is triggered starting the bunching process again for current $\mathbf{J}_{\perp\xi+1}$. The source location $S_{Z\xi}$ is different at each frequency ω_ξ . The process is continuous and can be broken up in as many parts as desired, effectively taking the limit $\xi \rightarrow \infty$. For the purpose of the present study, the process is analyzed in Section 5.2 by breaking it up into 3 or 4 parts, depending on the case in hand.

4.3 Wave amplification by Cyclotron Resonance

During the initial average bunching time $\tau_B/4$, phase bunched particles radiate coherently, and the amplitude of the emitted wave can be estimated if the velocity space distribution of particles $f(\mathbf{v}, \alpha, \lambda_m)$ is determined as a function of the electron velocity v , pitch angle α and geomagnetic latitude λ_m . The emitted wave adds to the amplitude of the triggering wave, and this process is called amplification by cyclotron resonance. The linear spatial amplitude growth rate γ can be determined from the

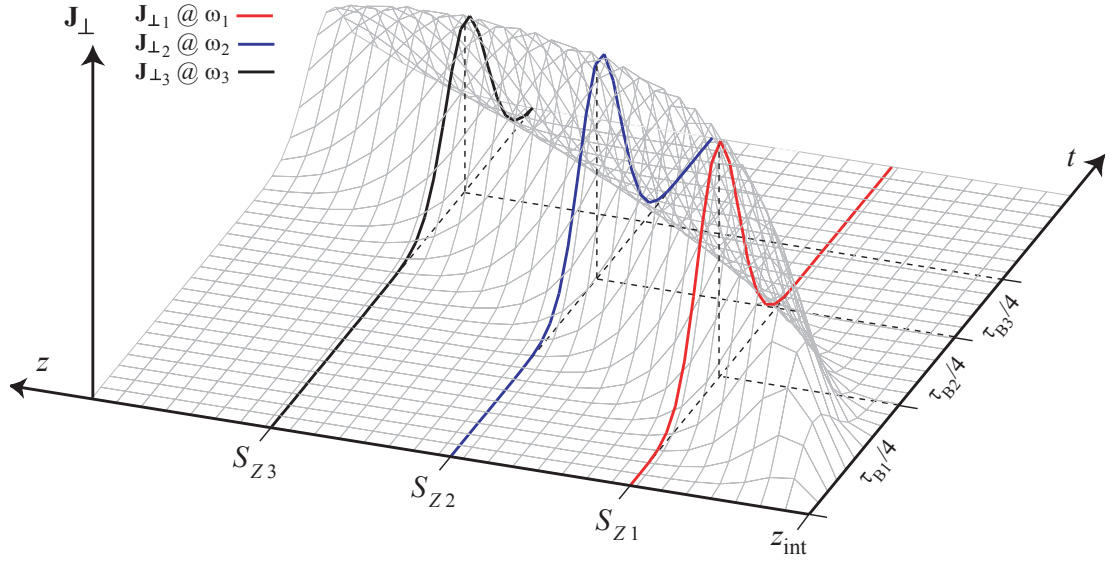


Figure 4.3: General description of the distribution in space and time of the perpendicular current produced by the resonant energetic electrons. The vertical axis indicates the amplitude of the perpendicular radiating current, the z -axis represents distance along \mathbf{B}_0 and the third axis represents time t starting from the moment the triggering pulse enters the interaction region at z_{int} . Even though the general shape of \mathbf{J}_{\perp} in this figure is based on previous calculations by *Trakhtengerts et al.* [2003], it is not produced from actual calculations. It represents only a conceptual diagram for informational purposes.

linear temporal growth rate ω_t given by the relation [Matsumoto and Kimura, 1971]:

$$\gamma = \frac{\omega_t}{v_g}$$

$$\gamma = \frac{-\pi}{2 N_h v_g} \frac{\omega_c \omega_{ph}^2}{\partial D / \partial \omega} \int_{-\infty}^{\infty} dv_z \int_0^{\infty} dv_{\perp} v_{\perp}^2 \delta(\omega - k v_z + \omega_c) \left(\frac{\partial}{\partial v_{\perp}} - \frac{k v_{\perp}}{\omega_c} \frac{\partial}{\partial v_z} \right) f(\mathbf{v}, \alpha, \lambda_m) \quad (4.2)$$

where

$$D = c^2 k^2 - \omega^2 + \frac{\omega \omega_p^2}{\omega - \omega_c}$$

and N_h is the number density of the energetic electrons, while ω_{ph} is their corresponding plasma frequency. In order to use this expression, a form for $f(\mathbf{v}, \alpha, \lambda_m)$ must be assumed. According to Liouville's theorem, $f(\mathbf{v}, \alpha, \lambda_m)$ is constant along the trajectory of the energetic electrons in velocity space. From *Bell et al.* [2000] the energetic electron distribution in velocity space $f(\mathbf{v}, \alpha, \lambda_m)$ is related to the perpendicular energetic particle flux j_{\perp} at any given point as follows:

$$j_{\perp} = \frac{C}{2} f(\mathbf{v}, \pi/2, \lambda_m) v^4 \quad (4.3)$$

where C is a proportionality constant introduced for units consistency. Therefore, the complete form of $f(\mathbf{v}, \alpha, \lambda_m)$ can be found if j_{\perp} is known as a function of geomagnetic latitude λ_m . This information can be obtained from the data acquired by the PEACE instrument during many of the perigee passes of Cluster, when the spacecraft crosses the geomagnetic equator following approximately the same magnetic field line over a given range of geomagnetic latitudes near the geomagnetic equator. In order to use (4.3) to provide a first order estimate of $f(\mathbf{v}, \alpha, \lambda_m)$, a loss cone distribution is assumed [Bell et al., 2000]:

$$f(\mathbf{v}, \alpha, \lambda_m) = \kappa \left[\sqrt{\frac{B_0(0)}{B_0(\lambda_m)}} \sin(\alpha) \right]^{\eta} v^{-4} \quad (4.4)$$

where κ and η are estimated from particle flux data from the PEACE instrument and $B_0(\lambda_m)$ is the magnitude of the Earth's magnetic field \mathbf{B}_0 at a given geomagnetic

latitude. The values of B_0 are obtained from the onboard magnetometer, while the Tsyanenko model [Tsyanenko, 2002a and 2002b] is used for locations in space that are not along the Cluster orbit, fitting the modeled version to the observed values where Cluster observations are available, as described in Tsyanenko [2002b].

The energy-time spectrogram in Figure 4.4 shows the magnitude of the perpendicular electron flux as a function of time and particle energy from observations by the PEACE instrument onboard Cluster 1 on July 24, 2003 (Figure 4.4a) and August 23, 2003 (Figure 4.4b). The black line shows the integral perpendicular flux for energies above 100 keV. The observations shown in Figure 4.4a are used for our model calculations of source motion, comparing the calculations of source location described in this Chapter with those obtained in Chapter 3. The 10–25 keV energy band is identified as the possible reservoir of particles that possess the necessary free energy to amplify the chorus waves from the background noise [Bell *et al.*, 2000]. The electron fluxes shown in Figure 4.4 are averaged over a pitch angle range of $87.27^\circ < \alpha < 92.75^\circ$. Since the magnitude of j_\perp in Figure 4.4 is in units of ergs/(cm² str sec eV), a simple change of units to el/(m² str sec) is necessary in order to use these values in calculations with (4.4). The pitch angle α distribution as a function of geomagnetic latitude λ_m is obtained from PEACE using the method described in Bell *et al.* [2000].

Figure 4.4b shows another Cluster 1 pass, during August 23, 2003. For this particular day the PEACE instrument was shut off before the geomagnetic equatorial crossing. Nevertheless, there is clear evidence of energetic electrons between 8 keV and 25 keV during the period 22:20 UT to 22:30 UT which can be used to interpolate, following the same gradient the black line follows for particles above 100 KeV.

The space-time development of the cyclotron resonance amplification mechanism is illustrated in Figure 4.5. In our system of coordinates, the z -axis is aligned along \mathbf{B}_0 and the positive direction points toward magnetic north. Phase bunching of electrons occurs as the wave packet that initiates the phase-bunching travels from z_{int} to z_B . During this process, wave amplification occurs as the particles move through the wave. Saturation is reached at a given value of B denoted as B_g , followed by a decrease in amplitude of the radiated wave. Phase bunched electrons leaving the wave packet radiate at a slightly different frequency due to reasons inherent to the generation

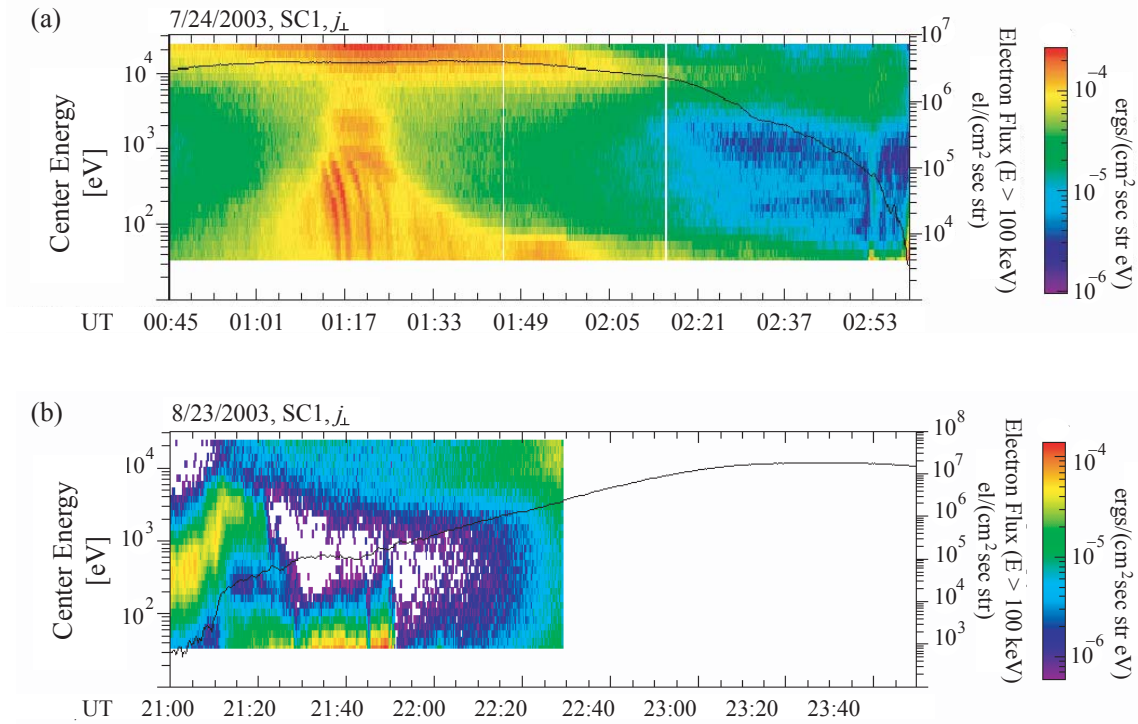


Figure 4.4: PEACE spectrogram of particle fluxes observed onboard SC1 on 7/24/2003 (a) and 8/23/2003 (b). The horizontal scale shows UT. The vertical axis on the left shows the energy in eV for perpendicular (averaged over a pitch angle range of $87.27^\circ < \alpha < 92.75^\circ$) differential electron fluxes j_{\perp} indicated in the color scale in $\text{ergs}/(\text{cm}^2 \text{ str sec eV})$, and is applied only to the vertical scale of the spectrogram. The vertical scale on the right shows the integral flux in $\text{el}/(\text{cm}^2 \text{ str sec})$ for particles with energies larger than 100 keV and applies only to the black line superimposed in the spectrogram.

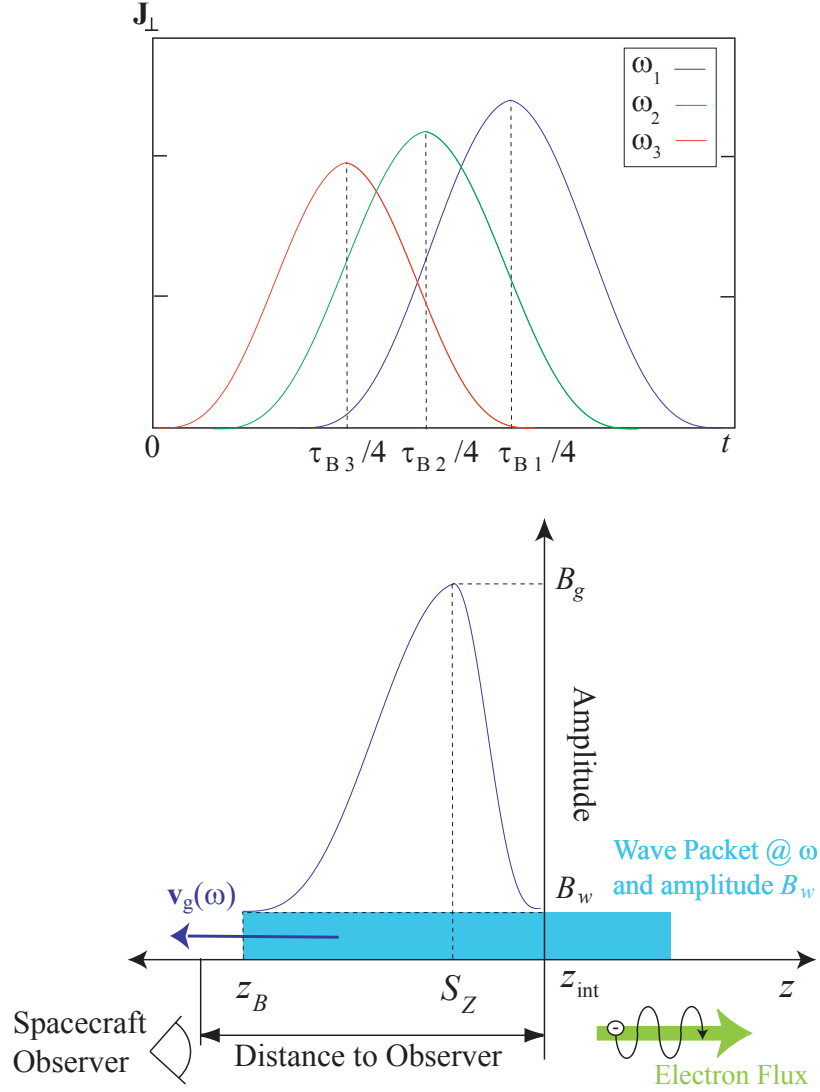


Figure 4.5: Wave amplification by cyclotron resonance. The left panel shows the behavior of the radiating current \mathbf{J}_\perp as a function of time. At time $t = \tau_B/4$, \mathbf{J}_\perp is maximum, for different frequencies ω_1 , ω_2 , ω_3 . The right panel shows the amplification at a given frequency ω . The vertical scale represents the wave magnetic field amplitude, and the horizontal scale represents distance along the magnetic field line, z . The dark blue curve is the wave amplitude as a function of z , and the light blue box represents the triggering wave packet propagating along z at a velocity $v_g(\omega)$. Even though the general shape of the radiating currents in this figure is based on previous calculations by *Trakhtengerts et al.* [2003], it is not produced from actual calculations. It represents only a conceptual diagram for informational purposes.

process (i.e., frequency-time shape of chorus is one of our starting observationally based assumptions), possibly related to the gradient in the Earth's magnetic field \mathbf{B}_0 . It is important to mention here that wave amplitude is an increasing function of distance in the direction of the electron flow, until it reaches a maximum due to saturation. The location along z at which the amplitude reaches a maximum value of B_g coincides with the location at which the radiating current is maximum, i.e., S_Z . Phase bunching still occurs for $t > \tau_B/4$, but the radiated wave eventually becomes out of phase with the triggering wave and cumulative wave growth thus ceases. The general behavior of \mathbf{J}_\perp is repeated in the upper panel of Figure 4.5 at three different frequencies, ω_1 , ω_2 and ω_3 . This figure is a simplified version of Figure 4 in *Trakhtengerts et al.* [2003], in which it is shown that the magnitude of \mathbf{J}_\perp can have secondary maxima later in time.

Newly emitted wave energy can only propagate in the electromagnetic whistler mode, i.e., in the counter streaming direction. These waves are Doppler shifted in frequency from their generation at the electron gyrofrequency, to lower frequencies (in the whistler mode band) due to the motion of the particles along the field line. The drifting motion of the source produces an additional Doppler shift in frequency, the sum total of which results in the frequencies observed onboard the spacecraft.

4.4 The Process of Source Motion

The complete process of source motion for one chorus element is described in Figure 4.6. Here the third axis of time is extended to show the process at different stages. A whistler mode wave enters the interaction region at z_{int} producing phase bunching of the energetic electrons and corresponding amplification through cyclotron resonance. At a given frequency ω_ξ , $z_{B\xi}$ is the location of the bunching wave packet at $\tau_{B\xi}/4$. At the location where saturation is reached, the source location for a given frequency ω_ξ , is defined by $S_{Z\xi}$. In other words, a wave radiated at frequency ω_ξ is generated by phase bunching due to a wave generated previously at $S_{Z\xi-1}$, and propagates a distance $\Delta z = z_{B\xi} - S_{Z\xi-1} = v_g(\omega_\xi) \tau_{B\xi}$ during this process. The radiated wave propagates in the counterstreaming direction and the bunching process restarts, but

due to the frequency-time change assumed to be inherent in the emission mechanism, possibly related to displacement along the field line and the corresponding change in \mathbf{B}_0 (i.e., the radiating frequency at ω_c), the new radiated pulse is at a slightly different frequency $\omega_{\xi+1}$. This process is continuously repeated and the resulting trace of source locations ($S_{Z\xi}$'s) constitute a motion of the source as defined previously. We calculate the values of $z_{B\xi}$'s and $S_{Z\xi}$'s for the different frequencies at each point $\xi = 1, \dots, 4$ ($\xi = 1, \dots, 3$ in Case 4), dividing the chorus element in four parts (three in Case 4) as described before in Chapter 3, using the previously introduced expressions for growth rate and bunching time:

$$|z_{B\xi} - S_{Z\xi-1}| = v_g(\omega)\tau_{B\xi} \quad (4.5)$$

$$\exp \left| \int_{z_{B\xi}}^{S_{Z\xi}} \gamma \, dz \right| = \frac{B_g}{B_w} \quad (4.6)$$

where $S_{Z0} = z_{\text{int}}$ and $\xi = 1, \dots, 4$ in Cases 1, 2 and 3 and $\xi = 1, \dots, 3$ in Case 4. Following the form of \mathbf{J}_\perp and the corresponding amplified wave, cyclotron resonance amplification evolves in the streaming direction, in terms of Figure 4.5; the lower panel shows that $z_B > S_Z$. In other words, if the electrons move along the negative z -axis direction, the absolute value bars in (4.6) are needed in order to have a positive valued integral. If the electrons move in the positive z -axis direction, then the absolute value bars are needed in equation (4.5) in order to have a positive value of distance. One cannot observe the direction of motion of the particular stream of electrons that generates a given chorus element, but the direction of wave propagation in the whistler mode is always counter streaming, and therefore the sense of the parallel direction of motion of the electrons can be simply deduced from the calculations of direction of wave propagation shown in Chapter 3.

Another important point to mention is that even though we consider that the subsequent bunching process starts again from location $S_{Z\xi-1}$ for the next frequency ω_ξ , the entire process is continuous, and that therefore the chorus element is continuously emitted at intermediate frequencies (and at intermediate locations) between ω_ξ and $\omega_{\xi+1}$. In our calculations the same value of natural background noise value B_w

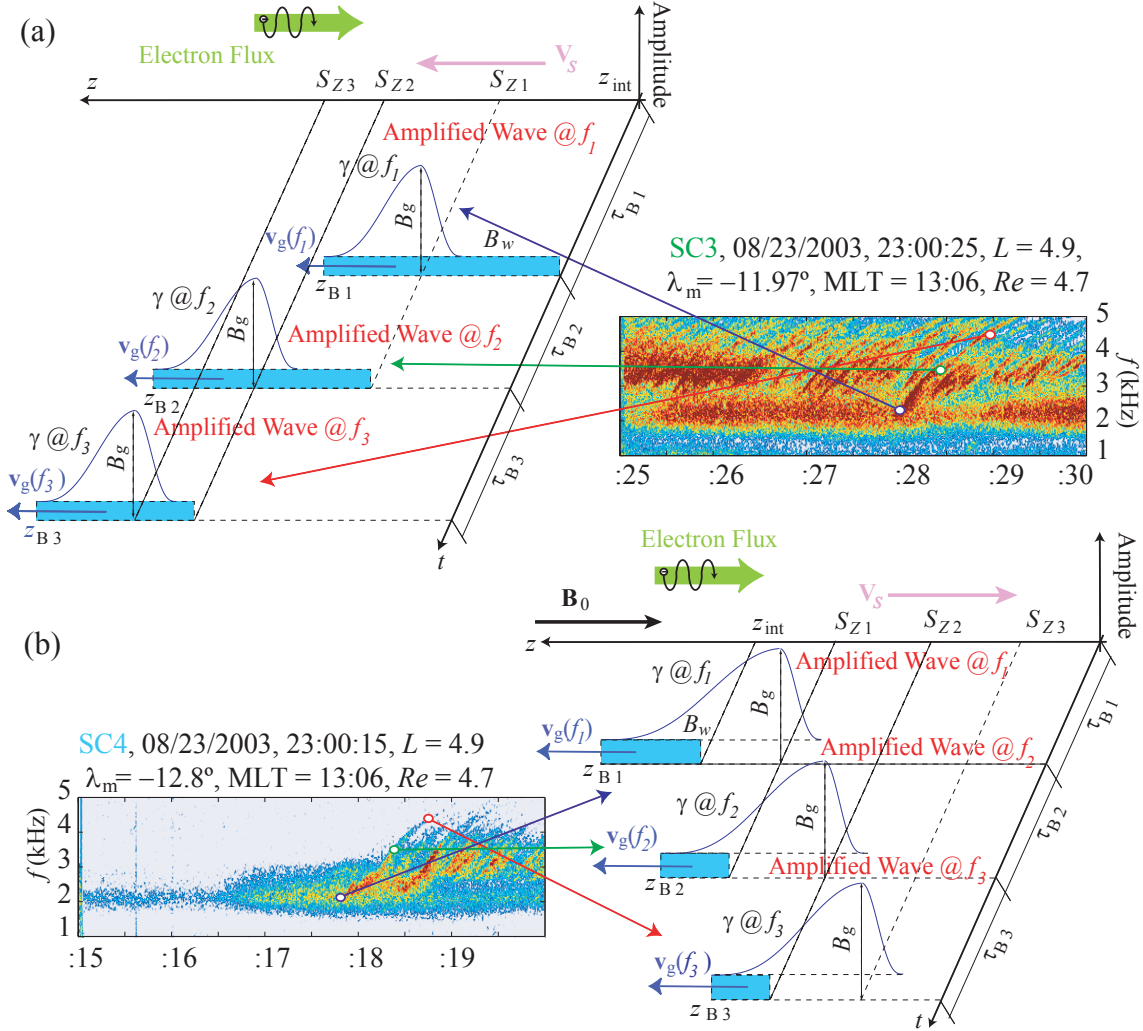


Figure 4.6: General description of the model, in two three-axis plots for a relatively large τ_B (a) and relatively small τ_B (b). The vertical axis indicates the amplitude of the wave magnetic field, the horizontal z -axis represents distance along \mathbf{B}_0 and the oblique axis represents time starting from the moment the triggering pulse enters the interaction region at z_{int} . The two WBD spectrograms showing observed chorus onboard SC3 (a) and SC4 (b) during 8/23/2003 are shown as examples. The arrows indicate the moment in time and frequency along the selected elements that correspond to the schematics in the three axis plots. The magnetic coordinates of each spacecraft and time are indicated on each spectrogram. The horizontal scale in the spectrograms represents time in seconds.

is used in (4.1) and (4.6) for each case studied. In other words, the wave is always amplified initially starting from the background natural existing noise. Values for B_w and α are assumed in the described cases, and the group velocity v_g is as given in (2.13) and (2.14).

The value of the wave normal angle ψ observed on a given spacecraft can be determined using the technique described in Chapter 2, and in general there is a different value for each observation point. For determination of the value of the wave group velocity, the average value from the results obtained in those calculations for each of the four spacecraft is used. Figure 4.6a shows the case where τ_B is relatively large, as a result of low values for the product $B_w \tan(\alpha)$ and the high anisotropy, leading to a relatively large γ . We calculate the values of $z_{B\xi}$ and $S_{B\xi}$, assuming a given value of B_w , using the equations of phase bunching time τ_B , group velocity v_g and growth rate γ .

The same process can be repeated if the conditions of the plasma are such that the bunching time τ_B is small, as a result of large values for $B_w \tan(\alpha)$ (with respect to the previous case), as well as relatively smaller growth rate γ due to a lower anisotropy. One such low growth rate case is illustrated in Figure 4.6b. Repeating the bunching and amplification process for lower values of τ_B and γ , it is found that source motion can also occur in the streaming direction.

4.5 Summary of the Model

The overall process of chorus source motion is a continuous one, even though we break it down here into $\xi = 1 \dots 4$, ($\xi = 1 \dots 3$ in Case 4) discrete steps for clarity. The process can be summarized in the following sequence of most important events for time and frequency points $\xi = 1, 2$ and onwards:

1. At $t = 0$, a triggering wave packet with amplitude B_w enters the interaction region (or is already present therein) at z_{int} and starts to phase bunch near-resonant electrons.
2. Phase bunched electrons begin to amplify the wave at frequency ω_1 , generated

by a radiating current $\mathbf{J}_{\perp 1}$. This wave propagates with velocity $v_g(\omega_1)$ and with a \mathbf{k} -vector $\mathbf{k}(\omega_1)$.

3. At the average bunching time of $t \simeq \tau_{B1}/4$ the radiating current reaches a maximum and the location at which the $\mathbf{J}_{\perp 1}$ reaches a maximum S_{Z1} is considered to be the source location of the chorus wave at frequency ω_1 .
4. The amplified wave with amplitude B_g , and frequency ω_1 propagates in the counter streaming direction.
5. At $t \simeq \tau_{B1}/4$, the bunching process starts again but now at a different frequency ω_2 , as is inherent in the generation mechanism, possibly determined by the gradient of \mathbf{B}_0 .
6. Phase bunched electrons begin to amplify the wave now at frequency ω_2 , generated by a radiating current $\mathbf{J}_{\perp 2}$. This wave propagates with velocity $v_g(\omega_2)$ a \mathbf{k} -vector $\mathbf{k}(\omega_2)$.
7. At $t \simeq \tau_{B1}/4 + \tau_{B2}/4$ the radiating current reaches a maximum and the location at which the $\mathbf{J}_{\perp 2}$ reaches a maximum S_{Z2} is considered to be the source location of the chorus wave at frequency ω_2 .
8. The amplified wave with amplitude B_g , and frequency ω_2 propagates in the counter streaming direction.
9. At $t \simeq \tau_{B1}/4 + \tau_{B2}/4$, the bunching process starts again, now at a different frequency ω_3 , as is inherent in the generation mechanism, possibly determined by the gradient of \mathbf{B}_0 .
10. The process continues until any of the conditions necessary for wave growth are no longer satisfied.

Chapter 5

Cases 3 and 4: Comparison of Source Location Results with Interpretation

‘No human investigation can be called true science without passing through mathematical tests.’¹

5.1 Observations on August 23, 2003

In this Chapter observations of chorus on the four Cluster spacecraft on August 23, 2003 are presented specifically from two regions before the spacecraft crossed the geomagnetic equator. This particular perigee pass was selected because the four spacecraft crossed the equator near $L = 4$, with a spacecraft separation of no more than 300 km. These two additional cases are interpreted using the method described in Chapter 2 to estimate the source location in 3D space.

¹Leonardo da Vinci. *Trattato della Pittura*, compiled and first published in 1651

5.1.1 Geomagnetic Conditions

The maximum K_p index observed in the 24 hours prior to the events studied here was about 6⁻ (The notation of a minus sign after the number means that the actual value is more than 5.5, but less than 6. This notation is used in K_p displays since the actual value does not have more than 1 significant digit). The record of the geomagnetic activity is presented in Figure 5.1a, showing the variation of the K_p index during the day before and several days after the observed events studied herein show.

To derive values of local plasma density, data from the Whisper resonance sounder [Décréau *et al.*, 1997] is used in the same process described in Chapter 3. Frequency-time spectrograms generated from electric field measurements using the Whisper instrument in the passive mode [Décréau *et al.*, 1997] are shown in Figure 5.1b. The four panels show spectrograms of one of the components of the electric field on spacecraft SC1, SC2, SC3 and SC4, for the pass on August, 23, 2003. In the basic nominal operational mode, as is the case presented in this study, the density is measured every 52 seconds on SC1. In SC2, SC3 and SC4 it is measured in the same manner during the first 15 minutes of the pass and every 104 seconds during the rest of the data acquisition on that day. The frequency and time resolution for the wave measurements are about 300 Hz and 2.2 s. As in Cases 1 and 2, these active and passive measurements are used to obtain the electron density through the method specified by Canu *et al.* [2001] and Trotignon *et al.* [2001 and 2003].

5.1.2 WBD Observations

Figure 5.2 shows an overview of the plasma wave electric field amplitude observed on the four Cluster spacecraft by the WBD instrument during August 23, 2003. Highlighted in black are the regions of the cases studied, Case 3 being at 23:00:25 UT and Case 4 at 23:02:30 UT. The four spectrograms presented in Figure 5.2 correspond to each of the four Cluster spacecraft, each measuring the same component of the electric field. The x -axis shows the universal time, as well as the geomagnetic coordinates (the L parameter, MLT, the geomagnetic latitude λ_m , as well as the radial distance Re) of spacecraft SC4, along the path. The vertical white lines observed in

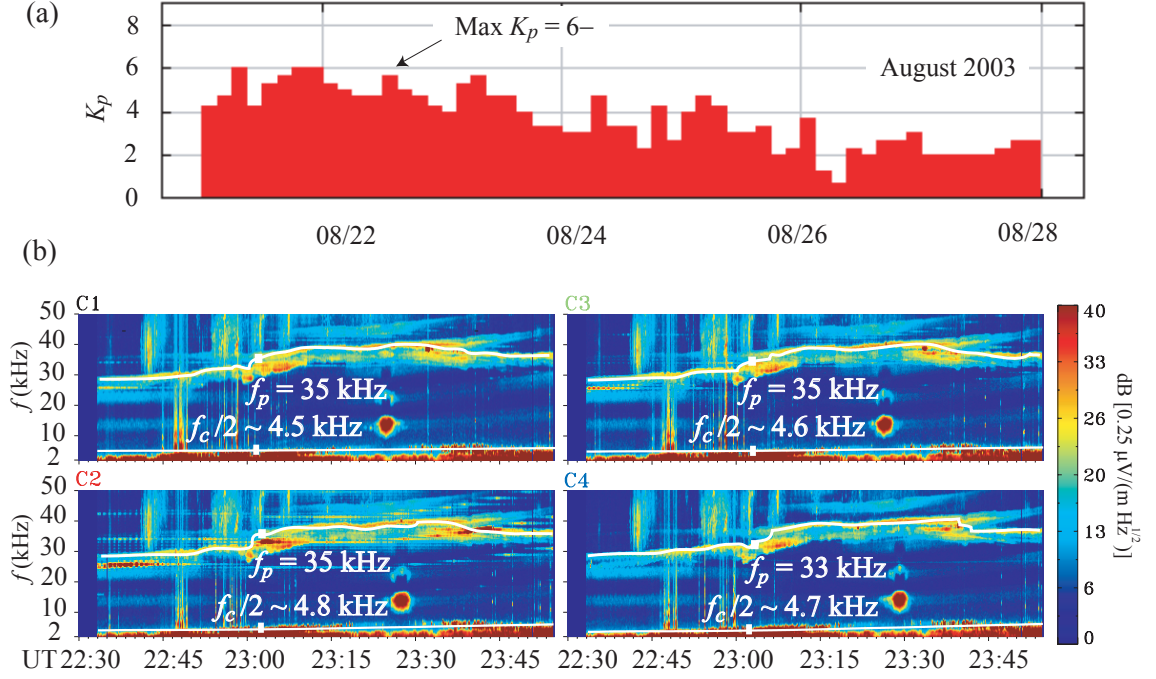


Figure 5.1: (a) Geomagnetic activity index (K_p) plot, for the last week of August, 2003. Highlighted is the local maximum in the K_p index value, as observed in the 24 hours previous to the observations shown in Figure 5.2. (b) Whisper overview spectrogram of the Cluster satellite pass during August 23, 2003, starting at 22:30:00 UT. The color scale is related to the magnitude of the electric field in dB, measured with respect to $0.25 \mu\text{V}/(\text{m}\sqrt{\text{Hz}})$. The y -axis indicates frequency, and the x -axis indicates universal time (UT). Highlighted in white are the plasma frequency f_p and a frequency ($f_c/2$) equal to one half of the electron gyrofrequency observed in each spacecraft, and the corresponding values of f_p and $f_c/2$ used for the calculations in Cases 3 and 4 respectively.

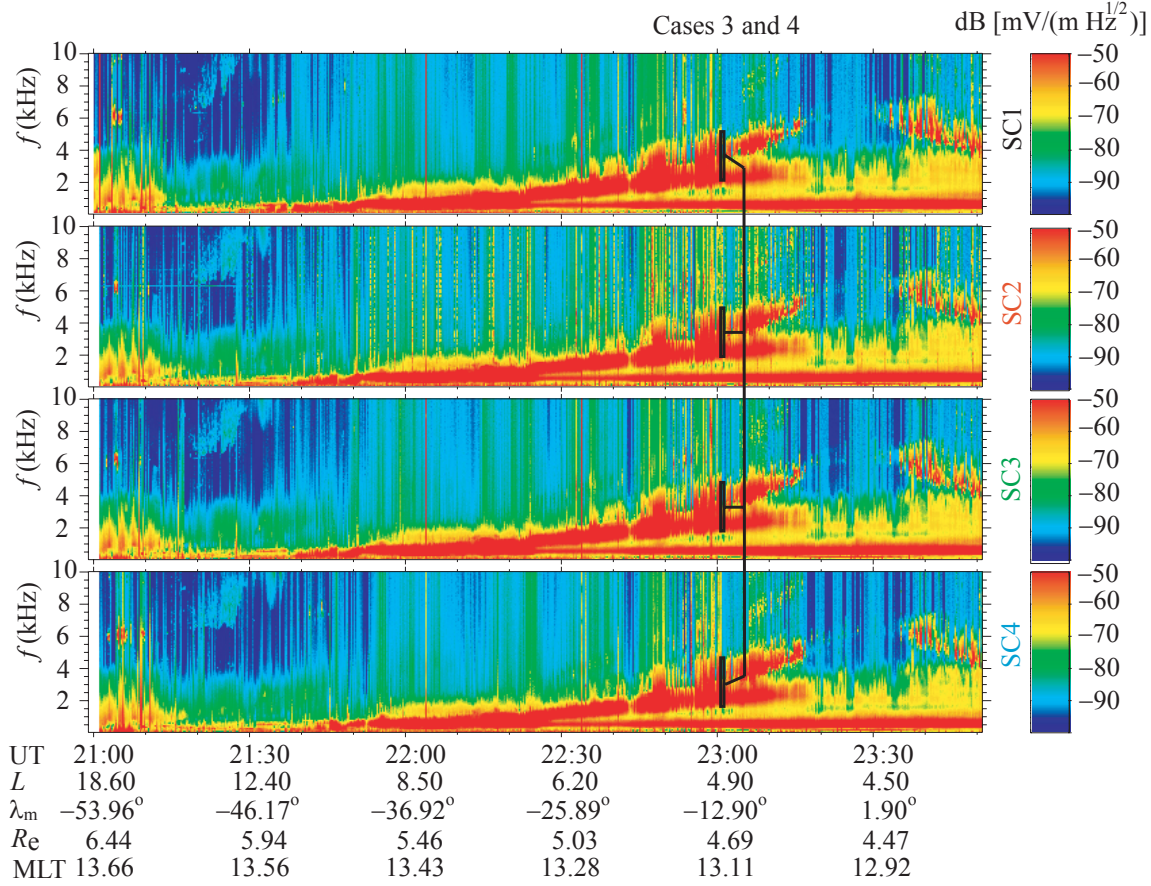


Figure 5.2: WBD overview spectrogram of the Cluster satellite pass during August 23, 2003, starting at 21:00:00 UT. The color scale indicates the magnitude of the electric field in dB with respect to $1 \text{ mV}/(\text{m}\sqrt{\text{Hz}})$. The y -axis indicates frequency, and the header above each spectrogram indicates universal time (UT) as well as position information of each spacecraft, in terms of the L parameter, geomagnetic latitude λ_m , geomagnetic local time MLT, and radial distance to the center of the Earth, Re . Highlighted are the two elements studied in Cases 3 and 4 respectively (they are too proximate to each other in time to be distinguishable in the time scale of this figure).

the spectrogram are interruptions in the measurements produced by the periodical switching of the wideband receiver between the electric and magnetic antennas, which is observed in the spectral data as a sudden change in the amplitude of the signal.

Simple visual inspection indicates that chorus emissions often have a very unique frequency-time structure, and that this structure, even when shifted in frequency and dispersed (e.g., slight changes in slope), still maintains its distinct frequency-time shape from one spacecraft to another. The method described in Chapter 3 of dividing similar elements observed in 4-second long sections into frequency-time points (such as the ones shown in Figures 3.3 and 3.4, or 5-second long sections as the ones shown in Figures 5.3 and 5.4) is used to measure the frequency-time characteristic of the single elements.

The four spectrograms in Figure 5.3c show single chorus elements, in a 5 second snapshot taken during a Cluster pass on August 23, 2003, at 23:00:25 UT. These elements are observed before the geomagnetic equatorial crossing. The chorus activity is observed on the four spacecraft SC1, SC2, SC3 and SC4. The spacecraft position with respect to one another is displayed in Figure 5.3b, in the same coordinate system used to show the results described below in this chapter. Figure 5.3a shows the location of the spacecraft in the frame of reference of the geomagnetic field, using the L parameter and the geomagnetic latitude λ_m as a coordinate system. The frequency time spectrogram displays lower-band chorus waves as observed by the three spacecraft at different times and frequencies. Most of these elements show a distinctive frequency-time characteristic with similar identifiable sections along the element. As before, it is assumed that individual chorus elements observed with distinctly similar frequency and time sequencing on different spacecraft emanate from the same source. For analysis purposes, a single element is divided into four points. The locations along the element of the points for this case were selected trying to match distinctive features in the $f - t$ characteristics (i.e., sudden changes in the slope, etc.) of the selected chorus element. For each point the time and frequency differences between the four spacecraft are measured, following the method described in Chapter 3. In this case it is much easier than in Cases 1 and 2 to identify the very unique frequency-time structure, and this structure, even when shifted in frequency

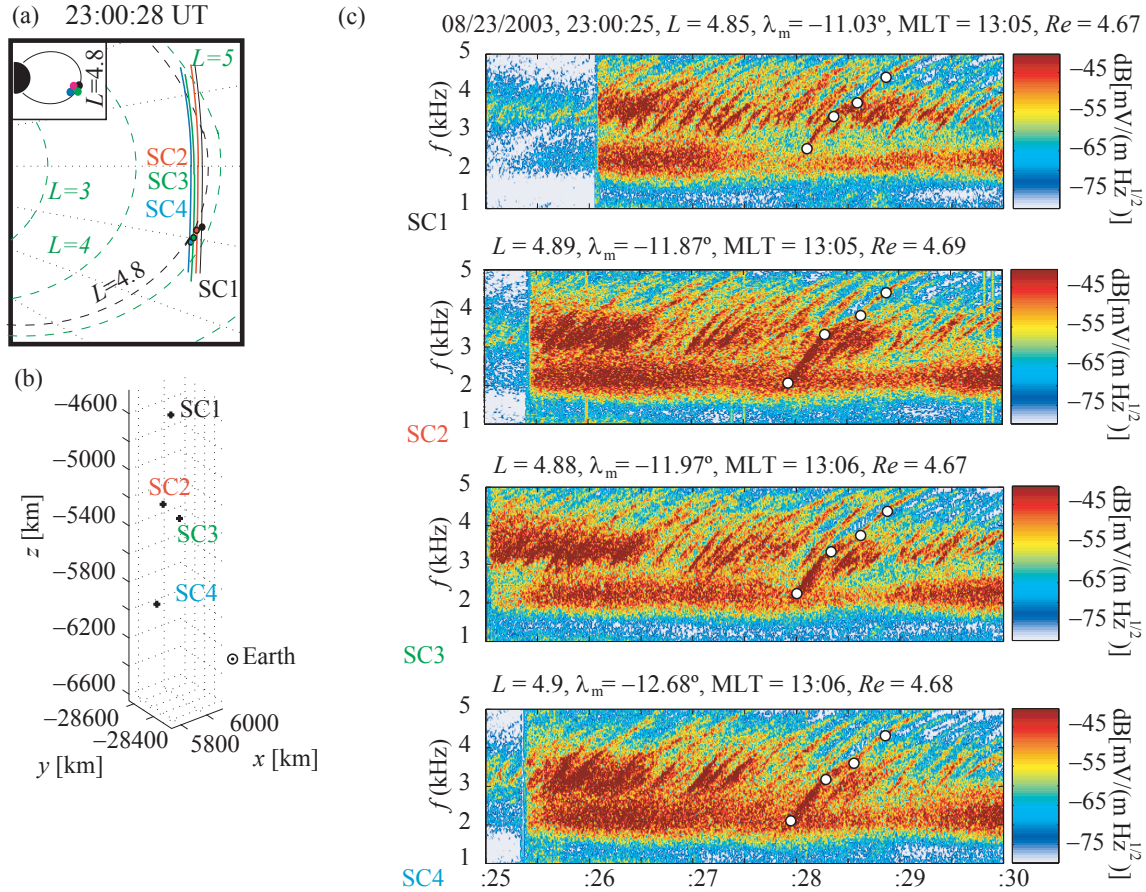


Figure 5.3: (a) Spacecraft location along the orbit for August 23, 2003. Indicated are the lines of constant L , and geomagnetic latitude λ_m . Highlighted are the 4 spacecraft, located at the place in orbit where the observations were performed. (b) Relative position of the spacecraft with respect to each other in space. (c) 5 s spectrograms as observed by 4 Cluster spacecraft, starting at 23:00:25 UT. The color scale indicates the magnitude of the electric field in dB with respect to $1 \text{ mV}/(\text{m}\sqrt{\text{Hz}})$. The y -axis indicates frequency, and the x -axis time in UT.

and dispersed (e.g., slight changes in slope), still maintains its distinct frequency-time shape from one spacecraft to another. The sudden increase in amplitude observed in SC1 and SC4 between seconds 25 and 26 is due to switch from the magnetic antenna to the electric antenna. The observations performed using the magnetic antenna are not calibrated, thus the values of amplitude are only valid for electric field measurements, even though the same amplitude scale is used in our displays for the magnetic measurements.

The four spectrograms in Figure 5.4c show single chorus elements, in a 5-second snapshot taken during a Cluster pass on August 23, 2003, at 23:02:30 UT, observed before the geomagnetic equatorial crossing. The chorus activity is observed on all four spacecraft SC1, SC2, SC3 and SC4. The spacecraft position with respect to one another is displayed in Figure 5.4b, in a coordinate system also used to show the results shown in Section 5.2. Figure 5.4a shows the location of the spacecraft in the frame of reference of the geomagnetic field, using the L parameter and the geomagnetic latitude λ_m as a coordinate system. The frequency-time spectrogram displays lower-band chorus waves as observed by the four spacecraft at different times and frequencies. Many of these elements show a distinctive dispersion characteristic in frequency, which have similar identifiable sections along the element. As in Case 3, it is assumed that individual chorus elements emanate from the same source. This time, a single element is identified with three points spaced in time and frequency along the element. For each point the time and frequency differences between the four spacecraft are measured. The same source location procedure followed in Chapter 2 is applied for Cases 3 and 4 and the results are shown in the next section. The solutions are compared to the results obtained for source location $S_{Z\xi}$ at each point ξ along the element, using equations (4.5) and (4.6).

5.2 Source Location Derived from PEACE Data

The source location in 1D and the direction of its motion can be directly determined from the calculation described in Chapter 4, by solving the system of equations (4.5) and (4.6). In this section, we apply this methodology to Cases 1 to 4, and compare

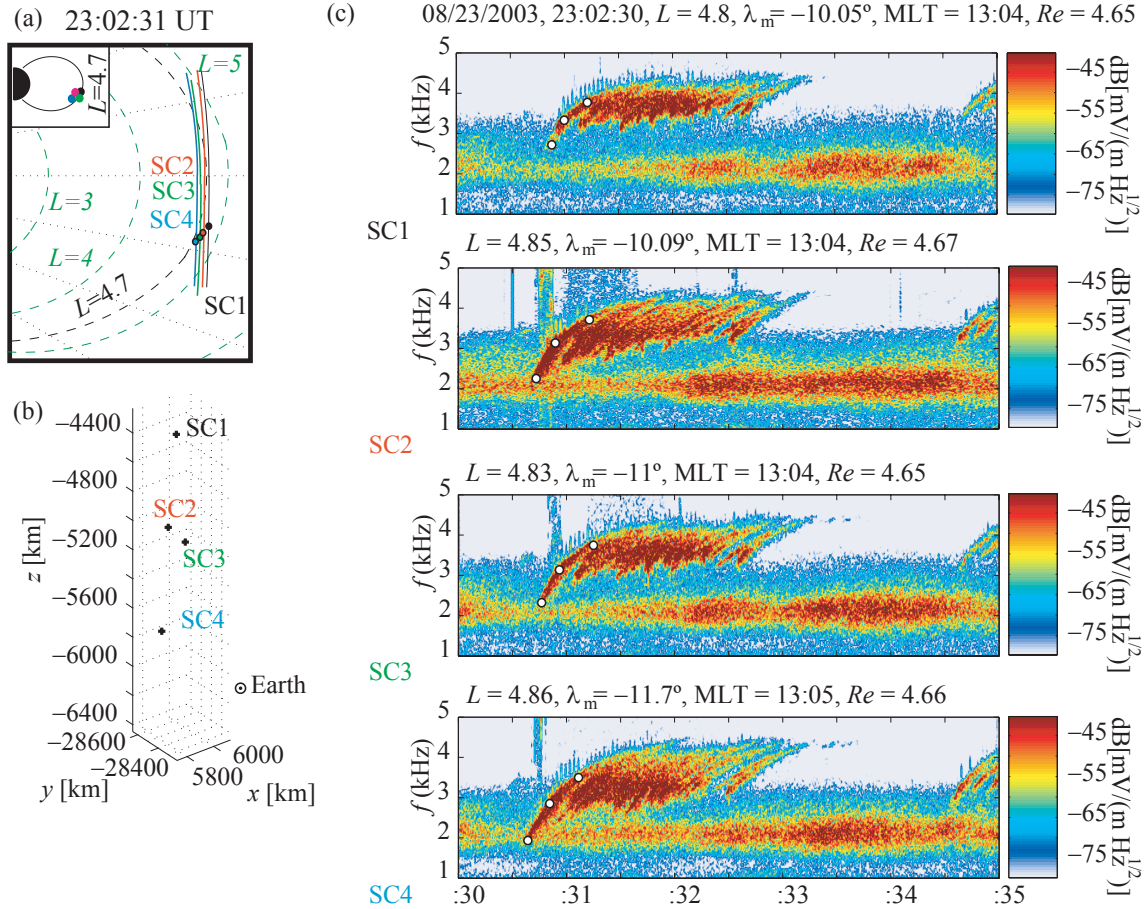


Figure 5.4: (a) Spacecraft location along the orbit for August 23, 2003. Indicated are the lines of constant L , and geomagnetic latitude λ_m . Highlighted are the spacecraft, located at the place in orbit where the observations were performed. (b) Relative position of the spacecraft with respect to each other in space. (c) 5 s spectrograms as observed by 4 Cluster spacecraft, starting at 23:02:30 UT. The color scale indicates the magnitude of the electric field in dB with respect to $1 \text{ mV}/(\text{m}\sqrt{\text{Hz}})$. The y -axis indicates frequency, and the x -axis time in UT.

results with 3D source location results obtained by application to Cases 3 and 4 of the differential Doppler shifts method described in Chapter 2 and previously applied to Cases 1 and 2 in Chapter 3.

The distribution function given in (4.4) is used with $\eta = 16$ and $\kappa = 1.875 \cdot 10^8$ el/(cm² sec str) for Cases 1 and 2 while $\eta = 27$ and $\kappa = 9.375 \cdot 10^7$ el/(cm² sec str) for Cases 3 and 4, using the measured values of electron flux obtained from Figure 4.4. For Case 1, $\omega_p/2\pi = 55$ kHz, $\omega_c/2\pi = 12$ kHz, for Case 2, $\omega_p/2\pi = 42$ kHz, $\omega_c/2\pi = 11$ kHz, and for Cases 3 and 4, $\omega_p/2\pi = 35$ kHz, $\omega_c/2\pi = 9.6$ kHz. For Cases 1 and 2, amplitude measurements from Figures 3.3 and 3.4 show that $20 \log(B_g/B_w) \simeq 30$ dB, while for Cases 3 and 4 we have from Figures 5.3 and 5.4 that $20 \log(B_g/B_w) \simeq 35$ dB. This parameter is obtained by considering the difference in amplitude between the chorus element average amplitude denoted B_g and the amplitude B_w of the background noise which initiates the amplification process as described in Chapter 4. In this context, we assume that the electric field amplitudes ratios between maximum and starting amplitudes of chorus are the same as the ones for magnetic field amplitudes.

The system of equations (4.5) and (4.6) can be easily solved numerically using any mathematical software such as MathCad or Mathematica, performing the integrals in (4.2). In the present study, a two step approach was used. First, equations (4.6) were decomposed into a Taylor series of order 5 and a first order solution was found for the unknowns $z_{B\xi}$ and $S_{Z\xi}$. The values thus obtained were then used in the actual equations to determine the final solution. The only iterative aspect of this calculation lies in the proper selection of the values of $B_w \tan(\alpha)$ and z_{int} . Different values of these three parameters can be assumed for each case, as is done in our calculations. The calculations of the $S_{Z\xi}$'s were performed by trying different values of the product $B_w \tan(\alpha)$ and z_{int} in order to find a combination of these values that provides a close fit (in a minimum square sense) for all four frequencies (three for Case 4), between the calculated S_Z values and those deduced from measurements of differential Doppler shift in Chapter 2.

For Case 1, displayed in Figure 3.3, the results are shown in Figure 5.5. The four panels presented herein correspond to four different values of frequency ω , calculated from the method described in Chapter 2. Similar results for Cases 2 and 3 are shown

in Figures 5.6 and 5.7. Case 4 was calculated using three points, which also fully allow us to represent the change in slope of the frequency-time characteristic for the waves, and the results for that case are shown in Figure 5.8. All of the six (four in Case 4) combinations of pairs from these four (three for Case 4) values of ω_i and t_i , for each spacecraft SC_i , are used to estimate the source location, which is represented as a green dot with its corresponding value in Figures 5.5 to 5.8. The values of source location in Figures 5.5 and 5.6 represented as green dots are reproduced from from Figures 3.5 and 3.7, while the values of source location shown as green dots in Figures 5.7 and 5.8 are calculated following the same procedure described in Chapter 2. The values of source location obtained from calculations of $S_{Z\xi}$ described in Chapter 4 are displayed in Figures 5.5 to 5.8 as red dots.

Since the calculation using the method of Chapter 4 is a 1-D determination, in order to display the results in the 3-D format of Figures 5.5 to 5.8, the $S_{Z\xi}$'s are placed along the z -axis and aligned in x and y with the result for the first green point, that is, along the same field line. The error bars for the red dots are obtained in a similar way as those for the green dots. The tolerances for the plasma frequency and the electron gyrofrequency are given as $|\omega_c - \omega_{co}|/\omega_{co} < 0.1$ and $|\omega_p - \omega_{po}|/\omega_{po} < 0.1$.

The results for Case 1 shown in Figure 5.5 were calculated using $B_w \tan(\alpha) \simeq 2.6 \times 10^{-13}$ T and a z_{int} that corresponds to a geomagnetic latitude of $\lambda_m = -15^\circ$. The results obtained for Case 2 shown in Figure 5.6 were calculated using $B_w \tan(\alpha) \simeq 6.5 \times 10^{-13}$ T and a z_{int} that corresponds to a geomagnetic latitude of $\lambda_m = 24^\circ$. The results for Case 3 shown in Figure 5.7 were calculated using $B_w \tan(\alpha) \simeq 15 \times 10^{-13}$ T and a z_{int} that corresponds to a geomagnetic latitude of $\lambda_m = 0.32^\circ$. The results for Case 4 shown in Figure 5.8 were calculated using $B_w \tan(\alpha) \simeq 3.3 \times 10^{-13}$ T and a z_{int} that correspond to a geomagnetic latitude of $\lambda_m = -4^\circ$. The value of α in these expressions was chosen as $\alpha \simeq 78.86^\circ$ for Cases 1 and 2 and $\alpha \simeq 81.336^\circ$ for Cases 3 and 4, obtained as the average of the pitch angle, weighted using the distribution function introduced in (4.4).

For these average values of α , we can determine the absolute magnitude of the noise amplitudes B_w and compare with data. The values of B_w are assumed not to change significantly as they propagate from the source to the spacecraft. Even though values

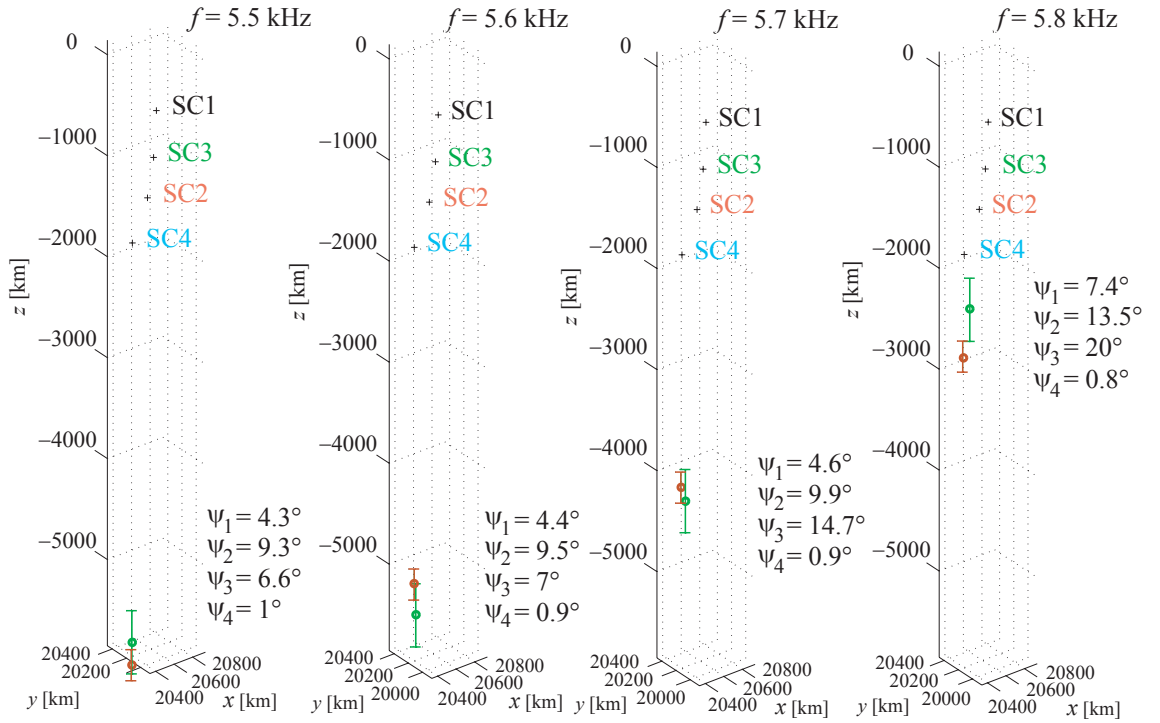


Figure 5.5: Source location results on July 24, 2003, 01:14:38 UT, for four different calculated frequencies, each frequency corresponding to each of the four panels. The position of the spacecraft is indicated as well as the source. The source location is obtained from Figure 3.5 (with the corresponding values of wave normal angle for each spacecraft ψ_i , for $i = 1, \dots, 4$) and shown in green. The source location determined from the calculations described in Chapter 4 is shown in red.

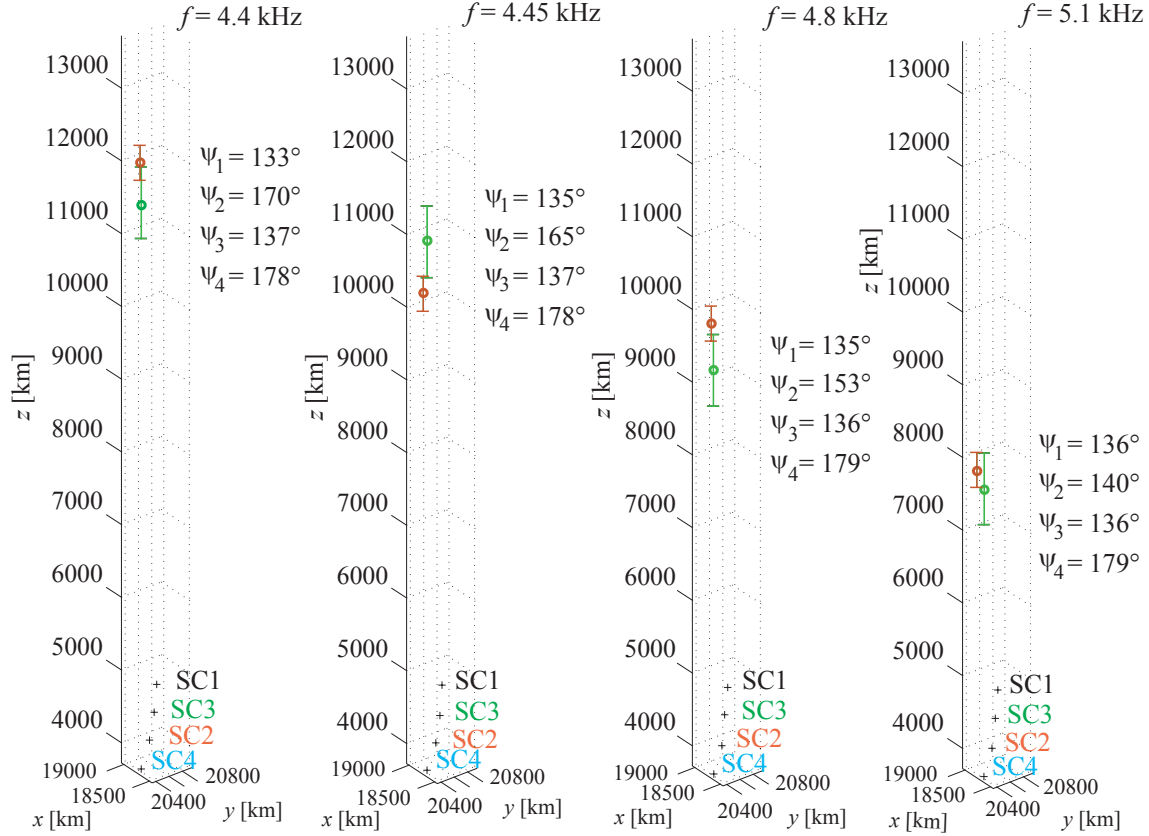


Figure 5.6: Source location results on July 24, 2003, 01:35:25 UT, for four different calculated frequencies, each frequency corresponding to each of the four panels. The position of the spacecraft is indicated as well as the source. The source location is obtained from Figure 3.7 (with the corresponding values of wave normal angle for each spacecraft ψ_i , for $i = 1, \dots, 4$) and shown in green. The source location determined from the calculations described in Chapter 4 is shown in red.

of amplitude in Figures 3.3, 3.4, 5.3 and 5.4 correspond to electric field magnitudes, the corresponding values of magnetic field can be obtained using the relationship $B \simeq \mu_0 \mu E / \eta_0$ where (only for this expression) $\mu_0 = 4\pi \times 10^{-7}$ H/m, $\eta_0 \simeq 377 \Omega$ and μ is given by (1.7). If we compare B_w to the magnitude of the plasma wave magnetic field for each chorus element studied in Case 1 we find: $B_w \simeq 4.5 \times 10^{-14}$ T which is 34.8 dB below the observed average magnitude of the magnetic field observed for the chorus element, obtained from the spectrograms in Figure 3.3. In Case 2, $B_w \simeq 5.7 \times 10^{-14}$ T which is 33.3 dB below the observed average magnitude of the magnetic field observed for the chorus element, obtained from the spectrograms in Figure 3.4. In Case 3, $B_w \simeq 2.34 \times 10^{-13}$ which is 30.16 dB below the observed average magnitude of the magnetic field observed for the chorus element, obtained from the spectrograms in Figure 5.3. In Case 4, $B_w \simeq 5 \times 10^{-14}$ T which is 41.8 dB below the observed average magnitude of the magnetic field observed for the chorus element, obtained from the spectrograms in Figure 5.4. These dB values are in reasonable agreement with the values of $20 \log(B_g/B_w)$ measured from data, indicating that our method of calculation is consistent.

Our simple model of source motion provides reasonably good agreement for all the Cases with the values of source location along the z -axis obtained from the data-driven calculations described in Chapter 2 and 5. The concept of a moving source is inherently linked to the result of having different values of source location for different values of frequency. Also it must be noted that the source seems to be moving toward the observing spacecraft in Cases 1 and 2, but away from the observer in Cases 3 and 4, traveling a distance of ~ 2500 km between the locations at which the lowest and the highest frequencies are generated. Even though the form of the distribution function $f(\mathbf{v}, \alpha, \lambda_m)$ as given in (5.4) was selected simply as a reasonable assumption our results seem to agree well in all the cases, suggesting that the source motion mechanism described in Chapter 4 is quite robust.

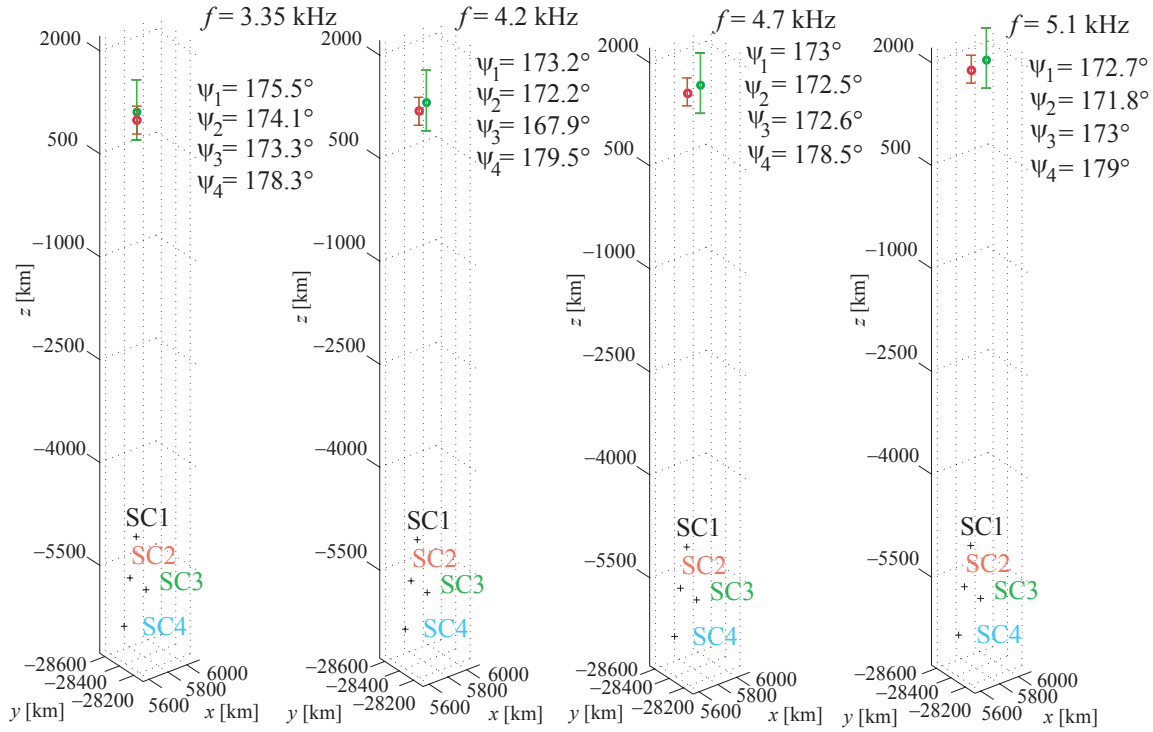


Figure 5.7: Source location results on August 23, 2003, 23:00:25 UT, for four different calculated frequencies, each frequency corresponding to each of the four panels. The position of the spacecraft is indicated as well as the source. The source location is estimated from the calculations described in Chapter 2 and shown in green. The source location determined from the calculations described in Chapter 4 is shown in red.

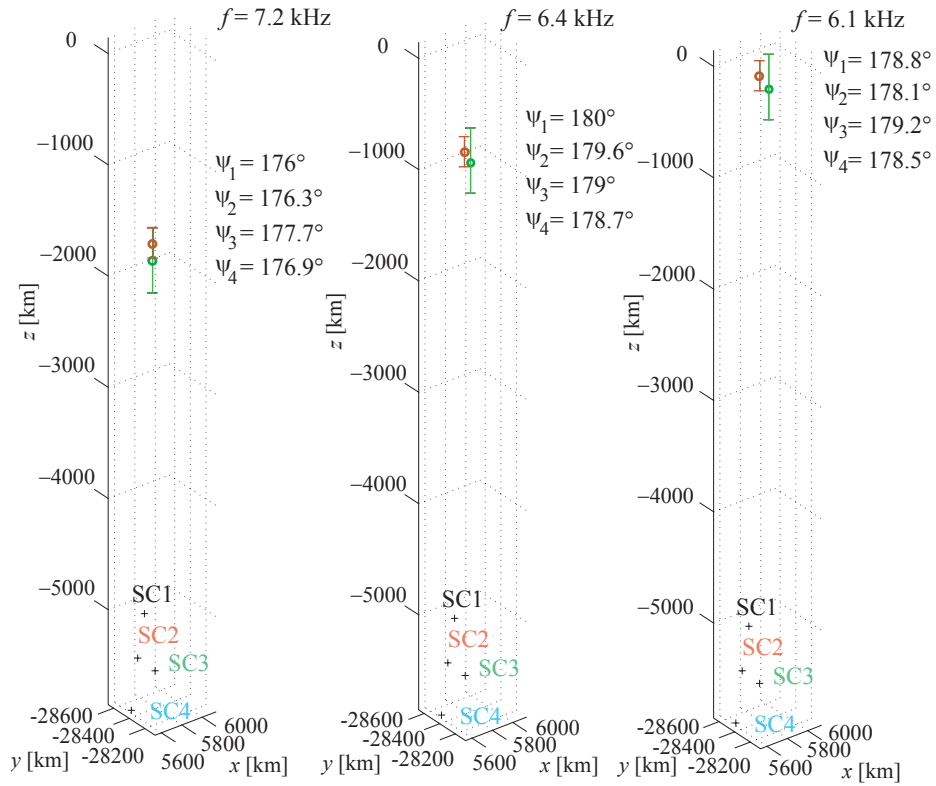


Figure 5.8: Source location results on August 23, 2003, 23:02:30 UT, for three different calculated frequencies, each frequency corresponding to each of the four panels. The position of the spacecraft is indicated as well as the source. The source location is estimated from the calculations described in Chapter 2 and shown in green. The source location determined from the calculations described in Chapter 4 is shown in red.

Chapter 6

Summary

‘In one case out of a hundred a point is excessively discussed because it is obscure; in the ninety-nine remaining it is obscure because it is excessively discussed.’¹

6.1 Summary

This study of chorus emissions and their sources was motivated initially by the observations reported in *Gurnett et al.* [2001], where individual, otherwise identical chorus elements were observed in two different spacecraft at different frequencies. This effect was originally interpreted by *Inan et al.* [2004] to be caused by the differential Doppler frequency shift of the signal propagating toward the spacecraft. In that article, the authors were able to estimate a source size and an approximate location with respect to the spacecraft.

In Chapter 2 of the present work, the method of source location from measured Doppler shift is generalized and expanded using WBD instrument observations from all four Cluster spacecraft to uniquely locate the chorus source in space without the assumptions of *Inan et al.* [2004]. In this process, wave group velocity, source velocity, and other parameters are calculated based on differential Doppler frequency shifts, and differential time delays observed in the spacecraft. We presented observations of

¹Edgar Allan Poe

two cases during July 24, 2003 and other two cases during August 23, 2003, where the upper and lower band chorus respectively showed an increase of intensity with increasing latitude and a decrease in its intensity and frequency of occurrence suddenly around the geomagnetic equator (Figures 3.2 and 4.2). This high variability near the geomagnetic equator is seen in the WBD instrument on almost every perigee pass of Cluster.

The frequency characteristics of chorus are displayed in more detail in Figures 3.3, 3.4, 5.3 and 5.4. In these cases chorus with rising frequency occurs, where the same element is seen with similar frequency-time characteristic on different spacecraft. A detailed method for estimating the source location and motion in space based on Doppler shift analysis is presented in Chapter 2 and applied to data in Chapters 3 and 5.

The results of our source location calculations are consistent with a compact transverse size of the source, while the emission of different frequencies comprising a single chorus element occurs over an extended region along the field line. This idea reinforces the interpretation of source motion given by *Inan et al.* [2004]. We have thus shown that discrete chorus emissions are produced in sources that are highly compact (of the order of one wavelength, or tens of kilometers) in the direction transverse to the magnetic field, but which are extended by as much as a few thousand kilometers along the magnetic field, so that different frequencies are emitted at different points along the field line.

For the cases studied here, the sources were found to be located within $-20^\circ < \lambda_m < 20^\circ$ of the geomagnetic equator, where the static magnetic field exhibits a minimum inhomogeneity in a dipole model. During disturbed periods, the magnetic field can exhibit multiple minima along the same L shell [*Santolík et al.*, 2003]. The presence of local minima in \mathbf{B}_0 can maximize the interaction lengths, and in the presence of high anisotropy in velocity space could lead to generation of chorus at locations not necessarily at the geomagnetic equator. Therefore chorus waves may be generated in regions of space other than the geomagnetic equator, as long as there is a local minimum of \mathbf{B}_0 .

Previous chorus observations such as those documented by *Lauben et al.* [2002],

also suggest that the location of the source of chorus waves is in the vicinity of the geomagnetic equator. It was concluded in *LeDocq et al.* [1998] that sources located at large distances from the spacecraft must emit chorus waves at low wave normal angles. *Lauben et al.* [2002] explained that waves at higher wave normal angles (except the special case at the Gendrin angle) tend to diverge away from the field lines, while waves emitted at wave normal angles close to 0° or at the Gendrin angle tend to remain more tightly focused and provide a coherent illumination over larger distances than do waves at other angles, in the absence of field aligned plasma irregularities. This conclusion agrees with the wave normal angles found in our Cases 3 and 4 (Chapter 5), as well as in Case 1 (Chapter 2).

The sources of chorus are found to be moving toward the spacecraft in Cases 1 and 2, which also happens to be toward the geomagnetic equator. The direction of propagation of the emitted chorus waves thus coincides with the direction of motion of the source in these two cases, therefore leading to a positive Doppler shift in the measurements. In Cases 3 and 4, the sources are found to be moving away from the spacecraft, away from the equator in Case 3 and toward the equator in Case 4. For these cases, the direction of propagation of the emitted chorus waves leads to a negative Doppler shift in Cases 3 and 4.

Source motion results obtained in Chapter 3 are shown to be a natural consequence of known properties of chorus emissions (i.e., rapid temporal growth, saturation, and inherent frequency-time change) using a physical interpretation based on wave-particle gyroresonance as a mechanism of generation of chorus waves as presented in Chapter 4. Sources of chorus exhibit motion along the field line, in the streaming or the counter streaming directions, depending primarily on the growth rate. Based on these results, source motion is presented herein as an intrinsic characteristic of chorus waves, which means that local spacecraft observations of the frequency of chorus waves near their source would register chorus at a frequency that is Doppler shifted not only due to the motion of the gyrating particles that radiate the wave packets, but also due to the motion of the source currents from which chorus is emitted. In other words, the moving sources in this context are certainly not the electrons themselves, but rather are the electrical currents constituted by the collectively organized electrons

which ultimately radiate chorus waves.

6.2 Discussion

The present calculations of source location and velocity as a function of frequency based on the Doppler shift and time delay between any two spacecraft reveal sources moving toward or away from the equator within geomagnetic latitudes $-25^\circ < \lambda_m < 25^\circ$. This result agrees with previous estimations of source location (*Burtis and Helliwell* [1969 and 1976], *LeDocq et al.* [1998], *Santolík et al.* [2003] and *Parrot et al.* [2003]) where sources location of chorus were found to be located within those geomagnetic latitude limits. In all four cases presented in this dissertation, rising tone elements are observed, i.e., waves with frequency increasing in time. These are the most commonly observed chorus elements, even though other shapes in frequency-time are also observed.

Figure 6 from *Helliwell* [1967] shows the most common frequency-time shapes of whistler mode triggered emissions that can be observed, according to the cyclotron resonance model, for waves propagating parallel to \mathbf{B}_0 . From the point of view of this interpretation, the frequency characteristic of the wave is completely determined by the motion of the source along the field through regions of different static magnetic field \mathbf{B}_0 with respect to the motion of the streaming particles. According to our interpretation in Figure 4.6, the direction of motion of the source does not necessarily coincide with the direction of motion of the streaming particles. To illustrate this point and compare with the cases presented in Figure 6 of *Helliwell* [1967], we summarize each presented case in particular:

- For the case described in Figure 4.6a, which corresponds to Cases 1 and 2, the source moves in the counterstreaming direction, i.e., in the direction of propagation of the chorus waves. According to Figure 6 of *Helliwell* [1967], in this situation a riser (faller) is expected for a source moving toward (away from) regions of *lower* B_0 , that is, toward (away from) the geomagnetic equator.
- For the case described in Figure 4.6b, which corresponds to Cases 3 and 4,

the source moves in the streaming direction, i.e., in the opposite direction of propagation of the chorus waves. According to Figure 6 of *Helliwell* [1967], in this situation a riser (faller) is expected for a source moving toward (away from) regions of *higher* B_0 , that is, away from (toward) the geomagnetic equator.

All of our Cases 1 through 4 involve risers. The results for Cases 1 and 2 show that the source moves toward the geomagnetic equator in the same direction as the propagating waves, which correspond to the case described in Figure 4.6a. These two cases agree with the prediction [*Helliwell*, 1967] of risers being generated by a source moving in the counterstreaming direction toward the geomagnetic equator. In Case 3 the source is moving in the streaming, i.e., in the opposite direction of the wave propagation, which corresponds to the case described in Figure 4.6b. This case also agrees with the prediction of risers being generated by a source moving in the streaming direction away from the geomagnetic equator [*Helliwell*, 1967]. Case 4 also corresponds to the situation described in Figure 4.6b, but does not agree with the prediction of *Helliwell* [1967], as the source is moving in the streaming direction toward the equator.

The fact that Case 4 results appear different from the predictions can be explained in at least two possible ways: First of all we must consider that chorus emissions are likely produced by a collective interaction of the wave with electrons distributed in both parallel velocity and pitch angle. In fact, our model of source motion involves the chorus waves growth rate due to gyroresonance, and the growth rate depends upon the entire energetic electron distribution. Therefore the fact that a rising emission is observed may not be uniquely related to the location of the source with respect to the equator, without detailed information about the energetic particle distribution function. This information is not taken into account in *Helliwell* [1967], which considered only the behavior of the resonant electron stream. Secondly the inconsistency can be explained if magnetic field compression produces a local minimum in B_0 located away from the equator [*Santolik et al.*, 2003]. This situation would allow for risers to be produced by a source moving toward the geomagnetic equator in the counterstreaming direction. Based on other different cases of Cluster observations of chorus, studied separately but not shown here, the production of risers by sources moving

	ω_1	ω_2	ω_3	ω_4
$\gamma[\text{dB/km}]$	0.34	0.37	0.32	0.4
$\tau_B[\text{s}]$	0.032	0.034	0.036	0.039

Table 6.1: Estimated values of average growth rate γ and bunching time τ_B for each estimated frequency ω_ξ , obtained for the calculations performed in Case 1.

toward the equator in the direction of wave motion is generally observed, with some exceptions as mentioned in *Inan et al.* [2004].

Tables 6.1 to 6.4 show the values of the two important parameters in the source motion process, the average growth rate expressed in dB/km and the bunching time expressed in seconds, for the four cases we have considered. As can be seen from Table 6.1, the values of growth rate change an order of magnitude from Cases 1 and 2 to Cases 3 and 4, with the two latter cases having highest growth. No such large differences exist in values of the bunching times, which range in magnitude between 0.02 sec to 0.09 sec in all the four cases. This result is not surprising since the bunching time depends largely on the cold plasma parameters, which are very similar on different days for the Cluster perigee passes of the geomagnetic equator near $L \simeq 4 - 5$.

These results lead us to believe that the determining parameter for the source motion process and the direction of motion of the source is the growth rate. For cases with lower growth rates (Cases 1 and 2) we have motion of the source in the counterstreaming direction, while for higher growth rates (Cases 3 and 4) the source moves in the streaming direction.

	ω_1	ω_2	ω_3	ω_4
$\gamma[\text{dB/km}]$	0.01	0.11	0.02	2.1
$\tau_B[\text{s}]$	0.029	0.028	0.03	0.031

Table 6.2: Estimated values of average growth rate γ and bunching time τ_B for each estimated frequency ω_ξ , obtained for the calculations performed in Case 2.

	ω_1	ω_2	ω_3	ω_4
$\gamma[\text{dB/km}]$	3.7	1.2	3.2	2.2
$\tau_B[\text{s}]$	0.018	0.02	0.021	0.022

Table 6.3: Estimated values of average growth rate γ and bunching time τ_B for each estimated frequency ω_ξ , obtained for the calculations performed in Case 3.

	ω_1	ω_2	ω_3	ω_4
$\gamma[\text{dB/km}]$	27	54	40	n/a
$\tau_B[\text{s}]$	0.082	0.064	0.058	n/a

Table 6.4: Estimated values of average growth rate γ and bunching time τ_B for each estimated frequency ω_ξ , obtained for the calculations performed in Case 4.

6.3 Suggestions for Future Work

6.3.1 Improvements on the Source Location Method

The source location method described in Chapter 2 is presented in a simplified way that allows for future improvements in several aspects. First of all, the assumption of straight line propagation in the defined system of coordinates can be relaxed. Even though it is a convenient one for the case in hand, all equations involving distances such as (2.12), (2.17) and (2.18) could be reformulated for a geomagnetic system of coordinates with the aid of the Haselgrove equations (3.3), (3.4) and (3.5). In this way, the additional step of verification using raytracing could be avoided by integrating this technique directly to the system of equation. However it should be mentioned that this step could introduce an extra degree of complexity to the already large system of equations obtained in Chapter 2 that would turn the calculation into a highly complex convex optimization problem. Nevertheless this important improvement could substitute the calculations expressed in our defined system of coordinates for those expressed in the more familiar geomagnetic field-aligned system of coordinates.

6.3.2 Improvements in the measurement of the frequency-time differences between spacecraft

The graphic method presented in Chapters 3 and 5 to obtain the frequency time differences represent a major source of error in the calculations presented in Chapter 2. This problem can be resolved by using more precise methods to determine the frequency-time differences between spacecraft, possibly based on a mathematical correlation method like the one presented in *Santolík et al.* [2006]. This process can take into account the possible errors in frequency and time introduced by the overlay method of Chapter 3. It could also allow for a more detailed representation of the frequency-time shape of the discrete element.

6.3.3 Improvements in the Physical Interpretation Model

The physical interpretation model presented in Chapter 4 also offers several chances of improvement. The linear growth model presented in equation (4.2) does not exhibit saturation, a feature that plays a key role in the calculations of that chapter but which nevertheless is introduced in a rather forced manner as an assumption. This assumption can be relaxed if a more sophisticated representation of wave growth can be used. For example, *Matsumoto and Kimura* [1971] introduces a non linear version of the growth rate that can take into account saturation. *Trakhtengerts et al.* [2003] also shows a behavior of the radiating current \mathbf{J}_\perp that inherently includes saturation and more sophisticated features, which can be used in our physical interpretation.

Bibliography

- Acton, F. S., *Numerical methods that work*, Mathematical Association of America, 1990.
- Baker, D. N., The occurrence of operational anomalies in spacecraft and their relationship to space weather, *IEEE Transactions on Plasma Science*, 28, 2007–2016, 2000.
- Balogh, A., et al., The Cluster magnetic field investigation, *Space Science Reviews*, 79, 65–91, 1997.
- Bartels, J., N. H. Heck, and H. F. Johnston, Three-hour-range index measuring geomagnetic activity, *Terrestrial Magnetism and Atmospheric Electricity*, 44, 411–454, 1939.
- Bell, T. F., Time reversal of geocyclotron mechanism, *Journal of Geophysical Research*, 69, 177–179, 1964a.
- Bell, T. F., Wave Particle Gyroresonance Interactions in the Earth’s Outer Ionosphere, Ph.D. thesis, Stanford University, 1964b.
- Bell, T. F., The nonlinear gyroresonance interaction between energetic electrons and coherent VLF waves propagating at an arbitrary angle with respect to the Earth’s magnetic field, *Journal of Geophysical Research*, 89, 905–918, 1984.
- Bell, T. F., U. S. Inan, R. A. Helliwell, and J. D. Scudder, Simultaneous triggered VLF emissions and energetic electrons distributions observed on POLAR with PWI and HYDRA, *Geophysical Research Letters*, 27, 165–168, 2000.

- Brice, N., Qualitative explanation of diurnal variation of chorus, *Journal of Geophysical Research*, *69*, 4701–4703, 1964.
- Burtis, W. J., Magnetospheric Chorus, Ph.D. thesis, Stanford University, 1974.
- Burtis, W. J., and R. A. Helliwell, Banded chorus-a new type of VLF radiation observed in the magnetosphere by OGO 1 and OGO 3, *Journal of Geophysical Research*, *74*, 3002–3010, 1969.
- Burtis, W. J., and R. A. Helliwell, Magnetospheric chorus: Occurrence patterns and normalized frequency, *Planetary and Space Science*, *24*, 1007–1024, 1976.
- Burton, R. K., Critical electron pitch angle anisotropy necessary for chorus generation, *Journal of Geophysical Research*, *81*, 4779–4781, 1976.
- Burton, R. K., and R. E. Holzer, The origin and propagation of chorus in the outer magnetosphere, *Journal of Geophysical Research*, *79*, 1014–1023, 1974.
- Canu, P., et al., Identification of natural plasma emissions observed close to the plasmopause by the Cluster-Whisper relaxation sounder, *Annales Geophysicae*, *19*, 1697–1709, 2001.
- Décréau, P. M. E., et al., WHISPER, a resonance sounder and wave analyser: performances and perspectives for the Cluster mission, *Space Science Reviews*, *79*, 157–193, 1997.
- Décréau, P. M. E., et al., Early results from the Whisper instrument on Cluster: an overview, *Annales Geophysicae*, *19*, 1241–1258, 2001.
- Dunckel, N., and R. A. Helliwell, Whistler-mode emissions on the OGO 1 satellite, *Journal of Geophysical Research*, *74*, 6371–6385, 1969.
- Escoubet, C. P., R. Schmidt, and M. L. Goldstein, Cluster-science and mission overview, *Space Science Reviews*, *79*, 11–32, 1997.
- Ferri, P., and M. Warhaut, Cluster mission operations, *Space Science Reviews*, *79*, 475–485, 1997.

- Gendrin, R., Guiding of whistlers by the magnetic field, *Planetary and Space Science*, *5*, 274–282, 1961.
- Goldstein, B. E., and B. T. Tsurutani, Wave normal directions of chorus near the equatorial source region, *Journal of Geophysical Research*, *89*, 2789–2810, 1984.
- Gurnett, D. A., and U. S. Inan, Plasma wave observations with the Dynamics Explorer 1 spacecraft, *Reviews of Geophysics*, *26*, 285–316, 1988.
- Gurnett, D. A., and B. J. O'Brien, High-latitude geophysical studies with satellite in June 3-5. Very-low-frequency electromagnetic radiation, *Journal of Geophysical Research*, *69*, 65–89, 1964.
- Gurnett, D. A., R. R. Anderson, F. L. Scarf, R. W. Fredricks, and E. J. Smith, Initial results from the ISEE-1 and -2 plasma wave investigation, *Space Science Reviews*, *23*, 103–122, 1979a.
- Gurnett, D. A., W. S. Kurth, and F. L. Scarf, Plasma wave observations near Jupiter: initial results from Voyager 2, *Science*, *206*, 987–991, 1979b.
- Gurnett, D. A., R. L. Huff, and D. L. Kirchner, The Wide-Band Plasma Wave investigation, *Space Science Reviews*, *79*, 195–208, 1997.
- Gurnett, D. A., et al., First results from the Cluster wideband plasma wave investigation, *Annales Geophysicae*, *19*, 1259–1272, 2001.
- Haselgrove, J., Ray theory and a new method for ray tracing, *Report of physical society conference on physics of the ionosphere*, Cambridge University, 1954.
- Hayakawa, M., Y. Yamanaka, M. Parrot, and F. Lefeuvre, The wave normals of magnetospheric chorus emissions observed on board GEOS 2, *Journal of Geophysical Research*, *89*, 2811–2821, 1984.
- Helliwell, R. A., *Whistlers and related ionospheric phenomena*, Stanford University Press, Stanford, California, 1965.

- Helliwell, R. A., A theory of discrete VLF emissions from the magnetosphere, *Journal of Geophysical Research*, *72*, 773–790, 1967.
- Helliwell, R. A., and T. L. Crystal, A feedback model of cyclotron interaction between whistler-mode waves and energetic electrons in the magnetosphere, *Journal of Geophysical Research*, *78*, 7357–7371, 1973.
- Hill, T. W., and A. J. Dessler, Plasma motions in planetary magnetospheres, *Science*, *252*, 410–415, 1991.
- Holzer, R. E., T. A. Farley, R. K. Burton, and M. C. Chapman, A correlated study of ELF waves and electron precipitation on OGO 6, *Journal of Geophysical Research*, *79*, 1007–1013, 1974.
- Horne, R. B., and R. M. Thorne, Relativistic electron acceleration and precipitation during resonant interactions with whistler-mode chorus, *Geophysical Research Letters*, *30*, 1527, 2003.
- Horne, R. B., et al., Wave acceleration of electrons in the Van Allen radiation belts, *Nature*, *432*, doi:10.1038/nature03939, 2005.
- Inan, U. S., and T. F. Bell, The plasmopause as a VLF wave guide, *Journal of Geophysical Research*, *82*, 2819–2827, 1977.
- Inan, U. S., R. A. Helliwell, and W. S. Kurth, Terrestrial versus Jovian VLF chorus: a comparative study, *Journal of Geophysical Research*, *88*, 6171–6180, 1983.
- Inan, U. S., Y. T. Chiu, and G. T. Davidson, Whistler-mode chorus and morningside aurorae, *Geophysical Research Letters*, *19*, 653–656, 1992.
- Inan, U. S., M. Platino, T. F. Bell, D. A. Gurnett, and J. S. Pickett, Cluster measurements of rapidly moving sources of ELF/VLF chorus, *Journal of Geophysical Research*, *109*, A05214, 2004.
- Isenberg, P. A., H. C. Koons, and J. Fennell, Simultaneous observations of energetic electrons and dawnside chorus in geosynchronous orbit, *Journal of Geophysical Research*, *87*, 1495–1503, 1982.

- Johnstone, A. D., et al., PEACE: a Plasma Electron And Current Experiment, *Space Science Reviews*, *79*, 351–398, 1997.
- Kennel, C. F., and H. E. Petschek, Limit on stably trapped particle fluxes, *Journal of Geophysical Research*, *71*, 1–28, 1966.
- Lauben, D. S., U. S. Inan, T. F. Bell, D. L. Kirchner, G. B. Hospodarsky, and J. S. Pickett, VLF chorus emissions observed by POLAR during the January 10, 1997, magnetic cloud, *Geophysical Research Letters*, *25*, 2995–2998, 1998.
- Lauben, D. S., U. S. Inan, T. F. Bell, and D. A. Gurnett, Source characteristics of ELF/VLF chorus, *Journal of Geophysical Research*, *107*, 1429, 2002.
- LeDocq, M. J., D. A. Gurnett, and G. B. Hospodarsky, Chorus source locations from VLF Poynting flux measurements with the polar spacecraft, *Geophysical Research Letters*, *25*, 4063–4066, 1998.
- Levenberg, K., A method for the solution of certain problems in least squares, *Quarterly Applied Math*, *2*, 164–168, 1944.
- Marquardt, D., An algorithm for least-squares estimation of nonlinear parameters, *Society for Industrial and Applied Mathematics*, *11*, 431–441, 1963.
- Matsumoto, H., and I. Kimura, Linear and nonlinear cyclotron instability and VLF emissions in the magnetosphere, *Planetary and Space Science*, *19*, 567–608, 1971.
- Meredith, N. P., R. B. Horne, and R. R. Anderson, Substorm dependence of chorus amplitudes: Implications for the acceleration of electrons to relativistic energies, *Journal of Geophysical Research*, *106*, 13,165–13,178, 2001.
- Meredith, N. P., M. Cain, R. B. Horne, R. M. Thorne, D. Summers, and R. R. Anderson, Evidence for chorus-driven electron acceleration to relativistic energies from a survey of geomagnetically disturbed periods, *Journal of Geophysical Research*, *108*, 1248, 2003.

- Moré, J. J., and M. Y. Cosnard, Numerical solution of nonlinear equations, *ACM Transactions on Mathematical Software*, *5*, 64–85, 1979.
- Nunn, D., A theoretical investigation of banded chorus, *Journal of Plasma Physics*, *11*, 189–212, 1974a.
- Nunn, D., A self-consistent theory of triggered VLF emissions, *Planetary and Space Science*, *22*, 349–378, 1974b.
- Nunn, D., A nonlinear theory of sideband stability in ducted whistler mode waves, *Planetary and Space Science*, *34*, 429–451, 1986.
- Nunn, D., Numerical simulation of VLF nonlinear wave-particle interactions in collision-free plasmas using the Vlasov hybrid simulation technique, *Computer Physics Communications*, *60*, 1–25, 1990.
- Nunn, D., Y. Omura, H. Matsumoto, I. Nagano, and S. Yagitani, The numerical simulation of VLF chorus and discrete emissions observed on the Geotail satellite using a Vlasov code, *Journal of Geophysical Research*, *102*, 27,083–27,097, 1997.
- Ondoh, T., Y. Nakamura, S. Watanabe, and T. Murakami, Latitudinal variation of chorus frequency observed in the topside ionosphere, *Journal of the Radio Research Laboratories*, *29*, 1–13, 1982.
- Parrot, M., O. Santolík, N. Cornilleau-Wehrlin, M. Maksimovic, and C. C. Harvey, Source location of chorus emissions observed by Cluster, *Annales Geophysicae*, *21*, 2003.
- Platino, M., U. S. Inan, T. F. Bell, D. A. Gurnett, J. S. Pickett, P. Canu, and P. M. E. Décréau, Whistlers observed by the Cluster spacecraft outside the plasmasphere, *Journal of Geophysical Research*, *110*, A03,212, 2005.
- Russell, C. T., R. E. Holzer, and E. J. Smith, OGO 3 observations of ELF noise in the magnetosphere: I. Spatial extent and frequency of occurrence, *Journal of Geophysical Research*, *74*, 755–777, 1969.

- Santolík, O., and D. A. Gurnett, Transverse dimensions of chorus in the source region, *Geophysical Research Letters*, *30*, 1031, 2003.
- Santolík, O., D. A. Gurnett, J. S. Pickett, M. Parrot, and N. Cornilleau-Wehrin, Spatio-temporal structure of storm-time chorus, *Journal of Geophysical Research*, *108*, 1278, 2003.
- Santolík, O., D. A. Gurnett, J. S. Pickett, M. Parrot, and N. Cornilleau-Wehrin, A microscopic and nanoscopic view of storm-time chorus on 31 March 2001, *Geophysical Research Letters*, *31*, L02,801, 2004.
- Santolík, O., D. A. Gurnett, J. S. Pickett, M. Parrot, and N. Cornilleau-Wehrin, Five years of investigation of whistler-mode chorus using the measurements of the Cluster spacefleet, *European Space Agency, (Special Publication)*, pp. 75–82, 2006.
- Sazhin, S. S., and M. Hayakawa, Magnetospheric chorus emissions: a review, *Planetary and Space Science*, *40*, 681–697, 1992.
- Scarf, F. L., D. A. Gurnett, and W. S. Kurth, Jupiter Plasma Wave Observations: An Initial Voyager 1 Overview, *Science*, *204*, 991–995, 1979.
- Schmidt, G., *Physics of High Temperature Plasmas*, Academic Press, New York, 1966.
- Smith, A. J., and D. Nunn, Numerical simulation of VLF risers, fallers, and hooks observed in Antarctica, *Journal of Geophysical Research*, *103*, 6771–6784, 1998.
- Smith, A. J., M. P. Freeman, and G. D. Reeves, Postmidnight VLF chorus events, a substorm signature observed at the ground near $L = 4$, *Journal of Geophysical Research*, *101*, 24,641–24,653, 1996.
- Smith, A. J., R. B. Home, and N. P. Meredith, Ground observations of chorus following geomagnetic storms, *Journal of Geophysical Research*, *109*, A02,205, 2004.
- Spasojević, M., and U. S. Inan, Ground based VLF observations near $L = 2.5$ during the Halloween 2003 storm, *Geophysical Research Letters*, *32*, L21,103, 2005.

- Stix, T. H., *The Theory of Plasma Waves*, Advanced Physics Monograph Series, McGraw-Hill, 1962.
- Storey, L. R. O., An Investigation of whistling atmospherics, *Philosophical Transactions of the Royal Society of London*, *246*, 113–141, 1953.
- Trakhtengerts, V. Y., Magnetosphere cyclotron maser: backward wave oscillator generation regime, *Journal of Geophysical Research*, *100*, 17,205–17,210, 1995.
- Trakhtengerts, V. Y., A generation mechanism for chorus emission, *Annales Geophysicae*, *17*, 95–100, 1999.
- Trakhtengerts, V. Y., A. G. Demekhov, Y. Hobara, and M. Hayakawa, Phase-bunching effects in triggered VLF emissions: Antenna effect, *Journal of Geophysical Research*, *108*, 1160, 2003.
- Trakhtengerts, V. Y., A. G. Demekhov, E. E. Titova, B. V. Kozelov, O. Santolík, D. Gurnett, and M. Parrot, Interpretation of cluster data on chorus emissions using the backward wave oscillator model, *Physics of Plasmas*, *11*, 1345–1351, 2004.
- Trotignon, J. G., J. Etcheto, and J. P. Thouvenin, Automatic determination of the electron density measured by the relaxation sounder on-board ISEE 1, *Journal of Geophysical Research*, *91*, 4302–4320, 1986.
- Trotignon, J. G., J. L. Rauch, P. M. E. Décréau, P. Canu, and J. Lemaire, Active and passive plasma wave investigations in the earth's environment: The cluster/whisper experiment, *Advances in Space Research*, *31*, 1449–1454, 2003.
- Trotignon, J. G., et al., How to determine the thermal electron density and the magnetic field strength from the Cluster/Whisper observations around the Earth, *Annales Geophysicae*, *19*, 1711–1720, 2001.
- Tsurutani, B. T., S. R. Church, and R. M. Thorne, A search for geographic control on the occurrence of magnetospheric ELF emissions, *Journal of Geophysical Research*, *84*, 4116–4124, 1979.

- Tsyganenko, N. A., A model of the near magnetosphere with a dawn-dusk asymmetry
- 1. Mathematical structure, *Journal of Geophysical Research*, *107*, 1179, 2002a.
- Tsyganenko, N. A., A model of the near magnetosphere with a dawn-dusk asymmetry
- 2. Parameterization and fitting to observations, *Journal of Geophysical Research*,
107, 1176, 2002b.
- Van Allen, J. A., The geomagnetically-trapped corpuscular radiation, *Journal of Geophysical Research*, *64*, 1683–1689, 1959.
- Warwick, J. W., et al., Voyager 1 planetary radio astronomy observations near Jupiter,
Science, *204*, 995–998, 1979.